FINITE ELEMENT ANALYSIS AND EXPERIMENTAL EVALUATION OF MAGNETIC STIMULATION OF NEURONS USING MICRO-SCALE COILS TOWARD AN IMPROVED COCHLEAR IMPLANT

A Dissertation
Presented to
The Academic Faculty

By

Sagarika Mukesh

In Partial Fulfillment of the
Requirements for the Degree

Doctor of Philosophy

School of Electrical and Computer Engineering

Georgia Institute of Technology

December 2018

FINITE ELEMENT ANALYSIS AND EXPERIMENTAL EVALUATION OF MAGNETIC STIMULATION OF NEURONS USING MICRO-SCALE COILS TOWARD AN IMPROVED COCHLEAR IMPLANT

Approved by:

Dr. Pamela T. Bhatti, Advisor
School of Electrical and Computer Engineering
Georgia Institute of Technology

Dr. Robert J. Butera
School of Electrical and Computer Engineering
Georgia Institute of Technology

Dr. Andrew F. Peterson
School of Electrical and Computer Engineering
Georgia Institute of Technology

Dr. Emmanouil M. Tentzeris
School of Electrical and Computer Engineering
Georgia Institute of Technology

Dr. Suresh K. Sitaraman
School of Mechanical Engineering
Georgia Institute of Technology

Date Approved: September 27, 2018

The time spent learning is time well spent

Sagarika Mukesh

To those who smile in the face of adversity.

ACKNOWLEDGEMENTS

Dr. Bhatti, for your patience, support, and continued guidance during the course of this thesis, many thanks. Thank you for giving me the opportunity to experience the diverse and challenging field of cochlear implant research. Thank you for encouraging my endeavors, both naive and savvy, and thank you for challenging me to do my best.

Many thanks to Dr. Butera for providing the necessary support to carry out the experiments for the completion of this thesis, and many thanks to Dr. Peterson for serving on my reading committee, and for his thoughtful feedback on my work. I would also like to thank Dr. Tentzeris and Dr. Sitaraman for kindly agreeing to serve on my defense committee.

The field of studying neuronal behavior is challenging and filled with uncertainties. I want to thank Riley Zeller-Townson for making this field more accessible to me through his constant support and guidance, and for his hands-on help with understanding the data acquired during experiments. I also want to thank him for many technical discussions, and for sharing his knowledge of the field with me. I want to thank Patrick Howard for plating and feeding my cultures, and want to thank all the Butera lab members for accommodating me in their schedule, and providing me with the space to perform experiments.

I want to thank Bijan Tehrani, Saswat Mishra, Christine Taylor, and Isaac Bower from the A.T.H.E.N.A, Yeo, and CASPaR labs at Georgia Tech, for helping me fabricate coils using different additive manufacturing techniques. It is challenging for PhD students to find time outside of their own projects, so, I really appreciate them finding the time to help me out.

I am also grateful for the constant support from the Electrical and Computer Engineering senior design lab. I would like to convey special thanks to James Steinberg and Kevin Pham for their help, whenever needed; and for making their equipment and services available to me. This project would have taken much longer to complete, if it were not for their support.

I want to thank Waqas Waheed, Ahmad Usman, Victor Alfonso Rodriguez Toro, Mohit

Agarwal, Abdullah Nauroze, and Aishwarya Natarajan for important technical discussions and support throughout my PhD. I also want to thank Jingting Yao and Karthik Rao for providing technical suggestions, editorial comments, and for their constant encouragement and support during this program.

I also acknowledge the help and support of the School of Electrical and Computer Engineering for structuring this PhD program and all the staff members for their constant support. In general, the Georgia Tech community has been very loving and supportive of its graduate students, especially its international students. I would like to acknowledge their efforts in ensuring our well-being and making our stay in the United States hassle-free.

I thank and appreciate the support of Microelectronics Research Center staff members in providing logistic help whenever required including but not limited to quick repairs of broken down systems, to avoid any significant delay in completion of work.

I also take this opportunity to thank my sponsor, National Science Foundation for their funding which was instrumental in supporting this research.

Last but not the least, I am grateful for the many friendships and would like to thank my friends for helping me cope through the pressures of graduate school. Ayush, Chirag, Aditi, Aishwarya, Achyut, Mohit, Becky, Alfredo, Victor, Felipe, and Divya, thanks for being there. I want to thank Kate and Bill, and Courtney and Josiah, for providing me a home for holidays. A special thanks to my husband for being supportive and patient throughout this journey, it couldn't have been as easy as he makes it seem. Thanks to my sister, for making me believe in myself. Thanks to my mothers, for being patient with me and showering me with their love. Finally, a heartfelt gratitude to the rest of my family for believing in me, encouraging me, and for their love and support.

TABLE OF CONTENTS

LIST OF TABLES

LIST OF FIGURES

CHAPTER 1
INTRODUCTION

Electrical stimulation of neurons has been the foundation of neural prosthetic devices for the last six decades. This technique is so prevalent today, that the term *neural stimulation* is synonymous to the term *electrical stimulation*. Some of the most successful electrical stimulation based devices today include pace-makers, deep-brain stimulators, and cochlear implants. However, electrical stimulation is also infamous for providing non-specific stimulation unless it is placed in direct contact with the target neurons. This non-specific stimulation results in several unwanted results, which show up as side-effects of using the particular technology, or lead to poor performance of the device, such as in the case of a cochlear implant [1] [2]. In applications like deep brain stimulation there is an option of placing the stimulation electrode in immediate vicinity of the target neurons. However, in the case of cochlear implants, this is not an option. This restriction on electrode placement results in poor sound quality as perceived by the cochlear implant patient because electrical stimulation has poor selectivity of neuron activation from a distance. In this thesis, we explore micro-scale magnetic stimulation as an alternative to this conventional electrical stimulation, and analyze the potential advantages and limitations of this technology.

1.1 Human ear and sensorineural hearing loss

The human ear, an organ responsible for hearing and providing a sense of balance, is divided into three main components: the outer ear, responsible for gathering sounds and funneling them into the ear canal; the middle ear, responsible for converting these sound vibrations into mechanical vibrations of the middle ear bones for the inner ear; and the inner ear, responsible for delivering sound, proprioception, and a sense of balance to the brain. The inner ear consists of the cochlea, a bony, fluid-filled structure with two-and-a-half turns

that is responsible for converting acoustic signals into electrical signals; and the vestibular system, consisting of semicircular canals and the otolith organs that collectively facilitate the sense of balance in humans (figure 1.1). Inside the cochlea, the organ responsible for producing electrical signals in response to the acoustic signals is the organ of corti, which consists of thousands of hairs cells that act as mini transducers. In response to an acoustic signal, these hair cells generate an electrical signal whose strength codes sound intensity and whose physical location of origin, inside the two-and-a-half turns of the cochlea, codes frequency. This frequency-to-space-mapping is called tonotopicity, a characteristic of the auditory system that is preserved all the way up to the primary cortex. For some people, the hair cells may become unresponsive due to disease, drug toxicity, or congenital defect resulting in a situation where the link between the ear and the brain fails. This failed link results in a medical condition called sensorineural hearing loss where a person eventually becomes profoundly deaf and is unable to benefit from a standard hearing aid. The only hope for people suffering from this condition is a cochlear implant- a neural prosthetic device that bypasses the hair calls and directly stimulates the auditory nerve, providing a sense of hearing to its user.

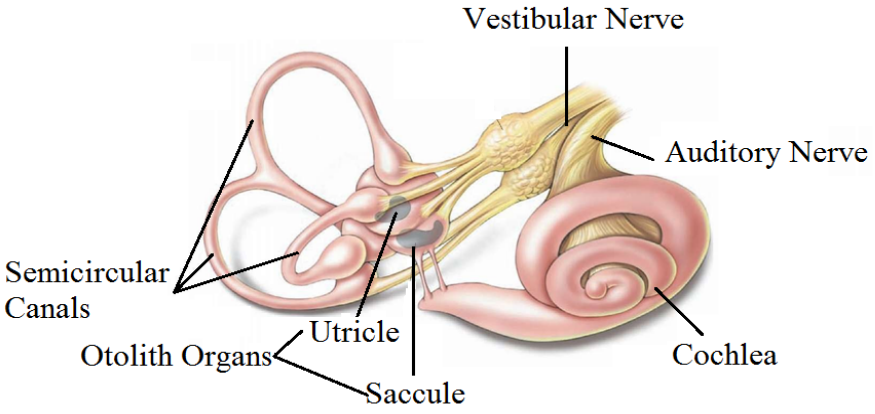

Figure 1.1: The structure of the inner ear consisting of the the cochlea and the vestibular system (Courtesy: Google Images)

1.1.1 Cochlear Implants and their shortcomings

As of December 2012, the National Institute on Deafness and other Communication Disorders (NIDCD) reported more than 324,000 people worldwide -including about 58,000 adults and 38,000 children in the U.S. -have received a cochlear implant [3]. These implants have three main components, an external microphone and signal processor that capture sound and break it into digital signals based on the sound's frequency content and energy; an implanted stimulator and electrode array that receive the digital signal through the third component- a telemetry unit (figure 1.2). The implanted stimulator drives a small electric current through one of the several electrodes to induce auditory nerve response. A patient who qualifies for an implant generally has one of these devices surgically inserted into the Scala Tympani, one of the three fluid-filled chambers of the cochlea. Once inside the cochlea, these implants stimulate auditory neurons by injecting an electric current into the surrounding tissue, thereby creating an electric field high enough to elicit a neuronal response. However, this technique leads to inflammation of tissue, negative electrochemical reactions, and non-focussed stimulation due to current spread; resulting in sub-optimal performance of the device. Additionally, patients complain about abnormal pitch perception and inability to enjoy music.

1.2 Research Statement

The efforts made to get rid of the problems faced by users of cochlear implants have tried to localize the stimulation pulse through current steering or current focusing, or increase access to the neurons through higher density arrays. However, these efforts have resulted only in incremental improvements, not in any drastic performance enhancements. This limited success prompted the exploration of a paradigm shift in the electrode-neuron interaction for cochlear implants, leading to the central theme of this dissertation: *Better sound quality can be achieved by stimulating a highly specific sensory neuron population via pulsed*

micro-scale magnetic stimulation of the cochlear neurons. To verify this hypothesis, this dissertation analyses the following:

- The spatial distribution of electric fields induced by a micro-scale inductor, studied using finite-element modeling
- Power consumed and heat produced by these inductors as compared to their electrical counterparts, both in simulation and in-vitro
- in-vitro stimulation of dissociated cortical neurons using a sub-millimeter coil, observed using planar multielectrode arrays
- Exploratory design and fabrication of planar sub-millimeter coils for potential application in cochlear implants

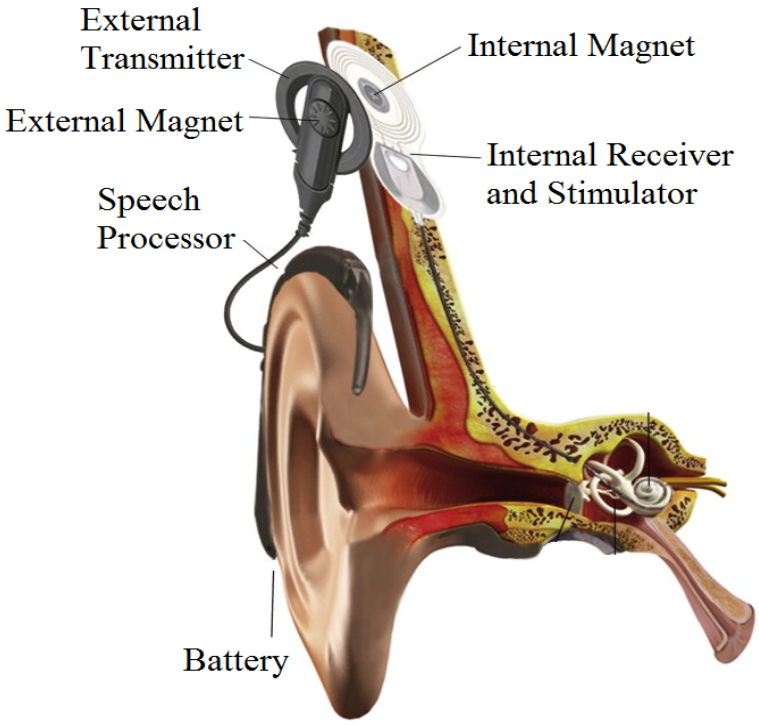

Figure 1.2: A contemporary cochlear implant system including an external microphone and signal processor, a telemetry unit and an implanted stimulator and electrode array (Courtesy: Med El Corporation, Durham, NC, USA)

We consider magnetic stimulation as an alternative to electrical stimulation because it has several advantages, such as, (a) no direct contact with target neurons to induce stimulation, (b) no deterioration in performance of the stimulator over time, as it will be insulated to prevent such degradation, (c) no concerns regarding surface electrochemistry at the site of implantation, and (d) minimal foreign body reaction.

1.3 Contributions of this thesis

The first contribution of this dissertation is a quantitative analysis of the electric fields induced by micro-scale inductors, for a better understanding of its spatial distribution inside the cochlea. The derivative of the induced fields, also known as activating function, is also calculated to quantify the effect of these fields on neurons. This spatial distribution is demonstrated to have better resolution, suggesting better frequency resolution, for an implanted magnetic array, by comparing the second derivative of electric potential with the first derivative of induced electric field using tools of finite-element analysis.

The second contribution of this dissertation focuses on feasibility and safety of the proposed magnetic stimulation through the analysis of power requirements and heating, through simulations and through experiments. These figures of merit are then compared to those of electrical stimulation.

The third contribution of this dissertation is an in-vitro experiment, where the effect of a self-assembled magnetic stimulator is evaluated on dissociated cortical neurons. The cells are plated on a multielectrode array (MEA), which is used to record the neuronal activity. The evoked responses and the stimulation parameters are recorded and analyzed to report responses to magnetic stimulation and power consumption. Spontaneous neuronal activity and responses to electrical stimulation are also recorded and compared to the responses to magnetic stimulation. Additionally, the voltages induced on the MEA electrodes are compared to the values predicted using theoretical analyses. This set of experiments characterize magnetic stimulation for a cochlear implant by analyzing its effect on a neuronal

level in a media similar to that present inside the cochlea.

The final contribution of this dissertation is an analysis of alternate planar coil designs and exploration of ways to fabricate them. Parameters such as requirement of a flexible substrate, bio-compatibility, and dimensions allowed by the physical structure of the cochlea are kept in mind while designing these coils and fabricating them. Techniques explored, problems faced, and future directions are reported.

1.4 Thesis organization

This thesis contains six other chapters, in addition to this chapter. An overview of these chapters are presented below.

Chapter 2 presents background for the different fields of study that motivated this work, and also surveys the state-of-the-art technology and most recent advances in the fields of micro-scale magnetic stimulation and neuronal recording.

Chapter 3 describes the theoretical and modeling work on magnetic stimulation of the cochlea using COMSOL, a finite-element-analysis tool. The induced electric fields, their respective activating function values, power consumption, and heating are evaluated for a set of parameters representative of neural stimulation. Then a planar coil is modeled to analyze the induced-field-neuron behavior due to the fields produced by it. Finally, magnetic stimulation of the vestibular system is reported as a second-use case.

Chapter 4 details the methods used during in-vitro experimentation and provides all the pertinent details for replicating the experiments described in it. It also describes the methods used for data analysis of the acquired data.

Chapter 5 focuses on a detailed analysis of the results obtained from experiments and discusses the implications of these results and the future directions.

Chapter 6 presents the design of planar coils and the exploration of different additive manufacturing techniques to fabricate it. The electrical properties of these fabricated coils are analyzed and the results are summarized.

Chapter 7 concludes this body of work and is followed by six appendices and bibliography. The first appendix briefly describes the mathematical formulation of the problem solved using finite-element modelling in chapter 3. Appendix B explains the concept of the activating function from a mathematical modeling perspective. Appendix C details the procedure for plating of the neurons on an MEA. Appendix D describes the procedure to Parylene coat a self-assembled stimulator. Appendix E presents some MATLAB codes used for data analysis, and Appendix F presents a map of the MEAs.

CHAPTER 2
BACKGROUND AND MOTIVATION

2.1 Cochlear implants

A cochlear implant (CI) is a neural prosthetic device that provides a sense of hearing to patients suffering from sensorineural hearing loss and consists of three main components-an external microphone and signal processor, a telemetry system, and an implanted stimulator and electrode array [4]. The external microphone and signal processor provide the signals that need to be interpreted by the patient, the telemetry system consists of two inductors that are mutually coupled through the skin of the scalp -one inductor resides outside and is connected to the external unit while the other sits on the inside and is connected to the implanted part of the device. The implanted component's output is in the form of small electrical pulses that induce activity in the proximal auditory neurons (see section 2.2.1 for details). These three main components of a cochlear implant lead to three distinct areas of research that are: (a) improving the external microphone and implementing enhanced signal processing algorithms, (b) improving the efficiency, aesthetics and performance of the telemetry system, and (c) improving the implanted stimulator along with providing a better neural interface for the implanted array (figure 1.2) [5] [6] [7] [8] [9].

From the perspective of signal processing, implants today come with options to enable the user to decide which part of the surrounding sound they want to focus on [10]. The algorithms that have lead to the implementation of these techniques rely heavily on machine learning and artificial neural networks [11]. The telemetry system has also been optimized and less patients have problems related to this component of the implant [8]. The implanted array, on the other hand, has not seen any drastic improvements in the last four decades and still relies on the techniques introduced in 1970s to stimulate the cochlear neurons.

The contemporary electrode arrays use electric currents to stimulate patients' surviving neural population. This technique dates back to the 1970s when the House 3M single-electrode implant was introduced in 1972, and was the first device to be commercially marketed [12]. During the same period, Clark and colleagues were developing a multi-channel cochlear implant in Australia that became the single-most implanted device in the world in the eighties, under the name 'Nucleus Multi-Channel Cochlear Implant'. These multiple channel devices enhanced the spectral perception and speech recognition capabilities compared to the single-channel device [13]. The implanted part of the devices used today is very similar in principal to these first successful implants. However, the patients who undergo the implant surgery require rigorous post-surgical rehabilitation to reap the benefits of this technology [14]. Some of the limitations of the contemporary implants are discussed in the following subsections followed by some of the efforts to overcome these drawbacks.

2.1.1 Current spread and spread of excitation

The frequency-to-space mapping inside the cochlea is called tonotopy (figure 2.1)- a characteristic of the auditory system that is preserved all the way up to the primary cortex. Cochlear implants with multi-channel electrode arrays make use of this property to achieve as many as four to eight functional channels at a time [1]; implying that if the input sound is broken into its frequency components, the implanted arrays are capable of stimulating areas most sensitive to four to eight different frequencies at once. While better than a single-electrode device, this technology is still limited to exciting areas that are far apart from each other inside the cochlea. This is because the presence of highly conductive perilymph inside the Scala tympani results in current spread resulting in non-focused stimulation. This problem is aggravated by significant cross talk between channels, thereby limiting the number of independent channels- given most implants have at least 22 channels but are able to achieve only four to eight independent channels at once. This means we end up stimulating a larger

region of the cochlea than we intend to, for example, in (figure 2.1) instead of stimulating the red region as intended, we end up stimulating the entire green region. This leads to abnormal pitch perception and poor quality of sound as heard by the brain [2]. Some patients also suffer from the problem of cross-turn stimulation where use of higher amplitudes of current to achieve a neuronal response results in stimulation of neurons from the higher turns of the cochlea. This can highly distort the signals received by the brain, exacerbating the already poor sound quality.

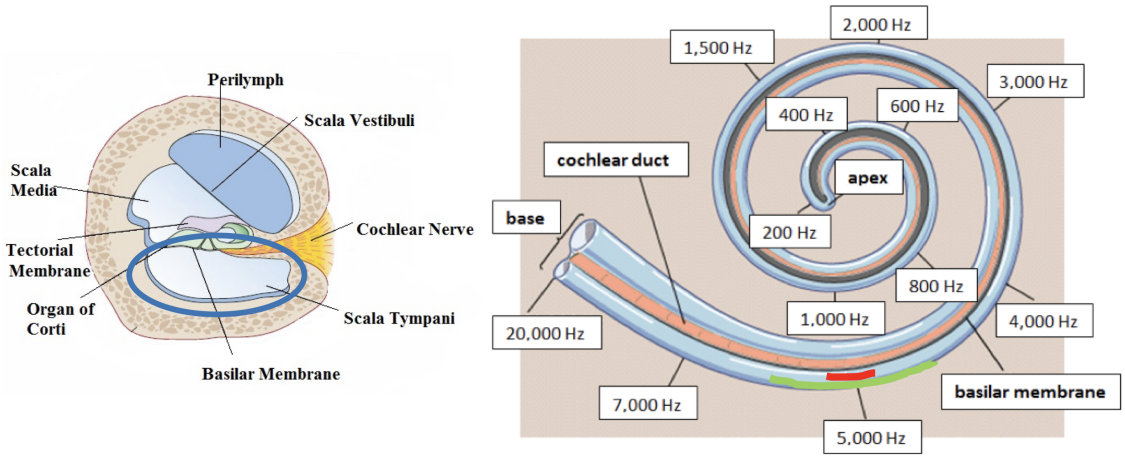

Figure 2.1: A cross section of the cochlea (left) and the tonotopic representation of the cochlea (right) (courtesy:Encyclopedia Britannica, Inc.)

2.1.2 Tissue scarring and foreign body reaction

In electrical stimulation of neurons, which is the state-of-the-art technique for CIs, the electrodes are a high-impedance circuit element capable of injecting sub-milliamperes of currents into the cochlea. Depending on the extent of sensorineural hearing loss, the amplitude of current injected into the cochlea needs to be adjusted by an audiologist after the implant surgery. In some cases, constant use of higher amplitude of current results in tissue scarring and permanent damage to the surrounding tissue [15]. A more prevalent problem is that of glia build up on top of the electrode surfaces. All implanted electrodes suffer from this problem, which leads to increase in impedance of the electrodes over time [16]. This usually results in the patients requiring higher amplitudes of current over time to achieve the

same level of hearing [17]. While this deterioration is mitigated by brain plasticity, studies have shown that improved speech recognition through standard post-implantation tests do not necessarily correlate with improved quality of life [18] [19]. These metrics suggest an urgent need to drastically improve the quality of sound heard by the cochlear implant patients, to enable them to lead a truly whole, multifaceted life.

2.1.3 Current steering, current focusing, and high density arrays for better sound quality

Some of the efforts made to improve the quality of sound by providing a more focused stimulation include current steering- creating additional virtual channels, and current focusing- restricting the spread of the neural activation. These concepts rely on the idea of deviating from the antiquated mono-polar stimulation- where the electrodes complete the circuit for stimulation with a distant ground electrode- and switching to bipolar and tripolar stimulation [20] [21]. In current focusing, one positive electrode is sandwiched between two negative electrodes, thereby eliminating the spread of current to undesired regions, in theory. Current focusing on the other hand relies on currents from two separate electrodes interacting with each other and stimulating regions of the cochlea not in direct reach of either one of the electrodes. While these concepts show great improvements in theory, they show marginal improvements in practice and have not led to drastic improvements in the sound quality [22].

High density arrays aspire to achieve similar goals as current steering by accessing more number of neurons through higher number of channels [23]. However, these arrays are also plagued by the drawbacks of the standard arrays where they are not able to recruit higher number of independent channels because of current spread and cross-channels interaction. Parallel efforts have pursued improving temporal content through signal processing schemes that retain rapid variations in the acoustic signal. However, the impact of these approaches on speech perception is mixed, and all rely upon electrodes, metal contacts, to exchange charge with tissue to modulate auditory nerve activity.

Some of the other novel ideas to improve electrical stimulation have included using micro-electrodes that are in touch with the neurons, thereby, eliminating the scope of current spread and the use of modiolus-hugging electrodes, to reduce the distance between the electrodes and the spiral ganglion neurons -the neurons present in the auditory system [24]. Modiolus is the central structure along the axis of the cochlea where all the neurons bodies are present (figure 2.2). It is the most reliable site for activation of neurons as it does not rely on the peripheral processes, which may be damaged to different extents depending on the extent of deafness in a patient.

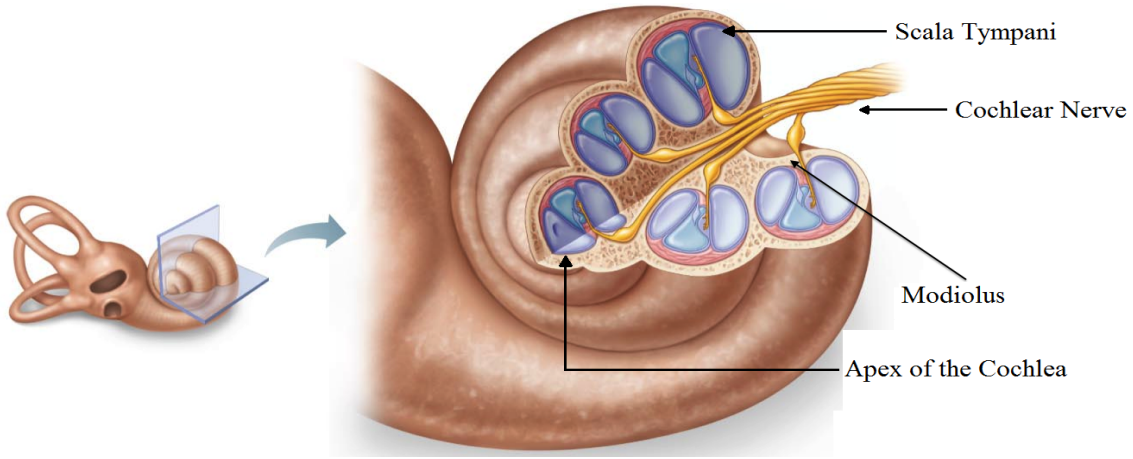

Figure 2.2: A vertical cross-section of cochlea highlighting the modiolus (Courtesy: Pinterest, Cold Brew Labs, Inc.)

2.1.4 Electric and acoustic stimulation, and optical stimulation

Some studies have highlighted the improvement in speech perception and ability to understand speech better in noisy environments through combination of electric and acoustic stimulation (EAS). This technique is useful for patients with residual hearing where one ear is implanted with a cochlear implant and the other is fitted with a hearing aid. However, it is only effective in patients with intact low frequency hearing. Moreover, some bilateral cochlear implant patients perform as well as patients with EAS, rendering EAS as effective as bilateral cochlear implants but not better [25] [26].

As cochlear implants are a grade-III medical device (as designated by the Food and Drug Administration), not a lot of effort has gone into changing the fundamental mechanism of exciting cochlear neurons. However, the limitations of existing technology encouraged researchers to explore alternative means for cochlear stimulation- the most significant of these being optical stimulation [27] [28] [29] [30]. The optical stimulation of cochlear neurons may be accomplished by using pulsed lasers at different wavelengths, nano-particle enhanced stimulation, or optogenetics [31] [32]. This technology claims to provide better frequency resolution and a more dynamic amplitude perception range [33]. Nevertheless, it suffers from several drawbacks and some of the major concerns include (a) safe expression of channel rhodopsins, which are the light sensitive proteins, (b) the channel kinetics of these opsins, (c) lack of an efficient neural interface, and (d) heating due to pulsed optical radiations [34] [35].

This thesis introduces an alternative paradigm shift in the stimulation of cochlear neurons by using magnetic stimulation instead of electrical or optical stimulation. The advantages of magnetic stimulation include, but are not limited to, enhanced frequency resolution, no physical contact with the neurons, and no genetic modification. Moreover, by avoiding direct contact with neurons, this technique also eliminates the problem of surface charge balance and tissue scarring.

2.2 Neural modeling and experimentation

Magnetic stimulation of neurons and neural elements is an alternative to their direct electrical stimulation. However, the basic mechanism through which neurons respond to extra-cellular potential is essentially the same. Hodgkin and Huxley characterized the neuronal response to extra-cellular potential through a series of voltage-clamp experiments that form the basis of most of the experimental paradigms and mathematical models related to extra-cellular excitation of neurons today [36]. How cells respond to external stimulus and some of the ways in which extra-cellular potentials are induced and measured are discussed below.

2.2.1 Cell membrane and active response to stimulus

All biological cells are surrounded by a cell membrane that is a thin layer of plasma consisting of 70 percent lipids. This membrane separates the contents outside the cells from those inside the cell, which primarily consists of ions. While the types of ions present inside a cell are the same as the types of ions present outside a cell-sodium, potassium, and chlorine, their concentrations vary greatly from inside the cell to that of the outside. Potassium concentration is much larger inside the cell than outside the cell, whereas sodium and chlorine are present in much higher concentration outside the cell than on the inside. This large variation in concentration leads to diffusion of ions from inside to outside or vice versa. However, the cell membrane is only semi-permeable, which means it only allows movement of ions in a particular direction. This behavior of the membrane is due to the presence of 'ion-channels' that are ion specific, the most common ones being the sodium-, potassium-, and calcium-channels. So, the rate of diffusion of ions is limited and this results in accumulation of charges on the either side of the membrane -resulting in a potential difference across the membrane. This potential difference creates an electric field that also exerts force on the charged ions, meaning, while at rest, the cell membranes balance the forces of diffusion and an electric field -this relationship is given by the Nernst-Planck equation [36]. When this equilibrium is disrupted by a signal from the brain or an extra-cellular potential, an action potential is generated that is propagated along the axon of a neuron (figure 2.3). The action potential consists of two main phases- the influx of sodium ions, leading to a positive peak, when measured intracellular, followed by the outflow of potassium ions - which brings the membrane potential back to the resting potential (figure 2.4). Since the media inside the cell and that outside the cell is passive, the active response to stimulus is obtained from the cell membrane. Scientists have used extra-cellular potential to modulate cell activities for years and some of the most successful applications are pacemakers and cochlear implants.

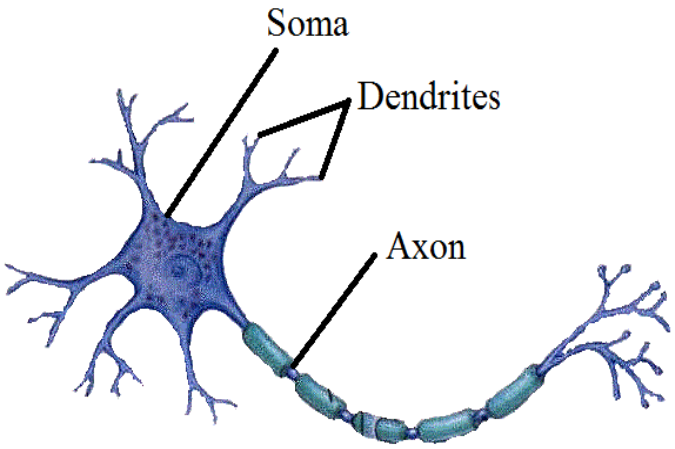

Figure 2.3: An image of a neuron with the long axon (courtesy: Encyclopedia Britannica, Inc.)

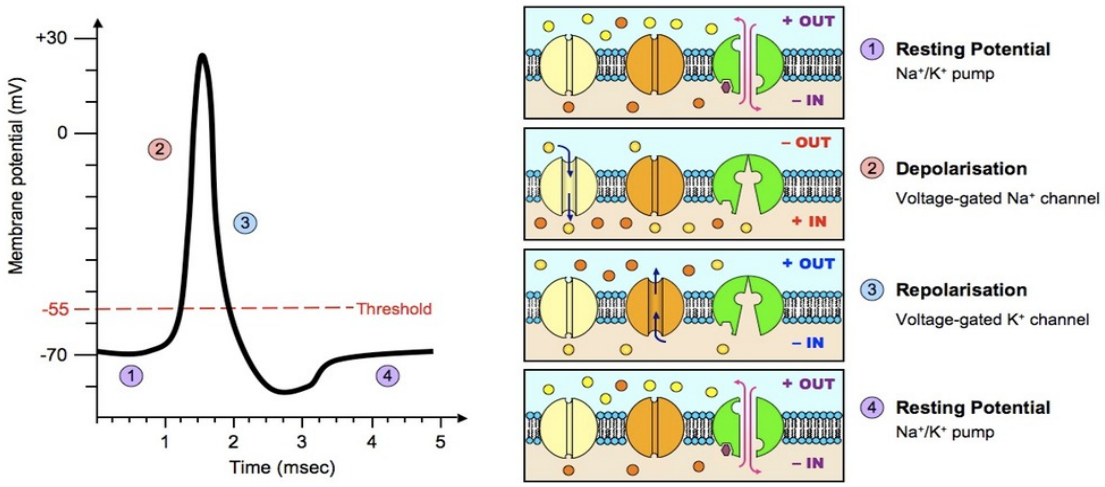

Figure 2.4: Graphic explaining the generation of an action potential;1. the cell membrane is at rest; 2. In response to stimulus, the sodium channels open and there's a movement of ions from outside the cell to the inside; 3. Now the cell is more positive on the inside than on the outside, so potassium ions exit the cell through the potassium channels, which are now open; 4. The membrane reaches the resting potential again. (Courtesy: [37])

2.2.2 Response to repeated stimulation

The action potential is similar to a digital signal, where either an extra-cellular potential induces an action potential, or it doesn't. There's no intermediate stage between these two states. However, when a repetitive stimulation is applied to neurons, such as in the case of a cochlear implant, several other responses to stimulus present themselves. The most prominent of these stimulus-evoked responses are: (a) refractoriness, (b) facilitation, (c) accommodation, and (d) spike rate adaptation [38]. Refractoriness is a measure of the post-spike recovery time, which corresponds to the time taken by the cell membrane to reach the resting potential, after the generation of an action potential. Facilitation is the generation of an action potential in response to two closely spaced sub-threshold pulses, whereas, accommodation is failure to generate an action potential in response of two sub-threshold pulses. Spike rate adaptation is a behavior observed over a longer time scale, where a neuron lowers its excitability in response to ongoing action potentials. These varied responses make the prediction of response to stimulus tricky, hence there's a need to experimentally study this responses. Chapters 4 and 5 discuss our assessment of response to micro-scale magnetic stimulation on dissociated cortical neurons.

2.2.3 In-vitro versus in-vivo experiments

Two different ways of understanding response to stimulus in a biological medium is through performing experiments inside a living subject, also known as in-vivo experiments, and through extracting live tissue in a dish, keeping it alive and performing experiments on this tissue, also known as in-vitro experimentation. The choice of methodology depends greatly on the question being answered. In-vivo experiments are a great way to understand neural circuits or changes in behavior in response to a stimulus, whereas in-vitro experiments are great for analyzing the effect of a stimulus on individual neurons. The work presented in this thesis is based on the results of an in-vivo experiment on a feline model that showed that magnetic stimulation works for a cochlear application and is being concluded through a set

of in-vitro experiments to better understand the effects of this stimulation. The advantages of in-vitro experiments include the following:

- They are cost-effective, compared to in-vivo.
- They allow for faster screening (negative in-vitro = negative in-vivo).
- As the neuronal circuit is isolated from rest of the system, there are fewer variables.

2.2.4 Maxwell and Rattay -magnetic stimulation modeling

Equations proposed by Maxwell tell us that a time-varying magnetic field induces a potential difference (Appendix A). Magnetic stimulation exploits this time-varying field to alter neuron functionality by either exciting or inhibiting the firing of neurons. The effect of magnetic fields on neurons has been studied for almost four decades now [39]. Three major factors are important to consider when modelling this effect: (1) spatial distribution of the induced electric fields, (2) temporal resolution of the induced electric fields, and (3) a compartmentalized model of the target neuron [40] [41]. However, most studies also use a simplified technique of calculating the Activating Function introduced by Rattay instead of solving for the entire compartmentalized model of a neuron [42] [43].

Rattay defines Activating Function (Appendix B) as the spatial derivative of induced electric fields, which helps predict the regions likely to be hyperpolarized or depolarized without solving the cable equation [44]. This function models the interaction of extracellular potentials with neurons, and provides an easy way for researchers to evaluate the performance of novel electrode designs and unconventional stimulation techniques. In this dissertation, the activating function is used to compare the spatial resolution of electrical stimulation with the spatial resolution of magnetic stimulation in the cochlea.

2.3 Multielectrode arrays for extracellular stimulation and recording

Multielectrode arrays (MEAs) provide a reliable interface for extracellular stimulation and recording of neuronal activity. With experiments dating back to the 1970s, where cardiac neurons were explanted onto an array of 30 micro-electrodes to understand the feasibility of a pacemaker, the high density arrays today consist of tens of thousands of electrodes and provide a sub-cellular resolution of neuronal activity [45] [46]. These arrays have been used to study a vast variety of neuronal responses such as high frequency oscillations caused by glia and controlling of culture-wide bursts through modulation of rate of stimulation [47] [48]. The behavior of dissociated cortical neurons, in particular, was studied over a period of five weeks, and their development was also reported [49]. Such studies would have been difficult to conduct in-vivo, because it is difficult to isolate sources of neuronal signals when the neural circuits are intact. Another study examined the response of spiral ganglion neurons (SGNs) to stimulation provided through MEA-electrodes and compared it to electrical stimulation provided from a distance of 40 μm, thereby showing that cochlear implants would perform better if the gap between the neurons and electrodes were eliminated or reduced [50]. Inspired from these studies and for the purpose of validating simulation results (discussed in chapter 3), this thesis uses a standard 64-channel MEA to record responses to magnetic stimulation from dissociated neuronal cultures as presented in chapters 4 and 5.

2.4 Micro-scale magnetic stimulation

Over the years, magnetic stimulation of neurons has advanced significantly and has found many clinical applications [51] [52]. It is an interesting technique for neural modulation because it can induce stimulation from a distance and is painless. Transcranial Magnetic Stimulation (TMS) is a non-invasive method employed for diagnostic and therapeutic purposes to treat depression, migraine, as well as to improve motor signals in those suffering from Parkinsons disease [53] [54] [55] [56]. This technique relies upon electromagnetic

induction and the ability of the body, a charge-carrying medium, to respond to changing magnetic fields applied externally. In such applications a generator is placed external to the region of interest and time-varying currents are pulsed through a coil thereby creating magnetic fields in the body. In turn, electrical currents are induced in the nearby region of interest and serve to modulate the activity of excitable tissue. There have been many studies exploring optimal stimulation times, pulse shapes, coil geometries and the relationship between induced electric fields and distances [57] [58] [59].

While non-invasive, TMS can only induce currents locally, a few millimeters in depth, and therefore is limited. Furthermore, there have been concerns regarding patient discomfort, loss of focus, high power consumption, as well as a host of undesirable secondary effects [60]. Additionally, the effect of magnetic stimulation on individual neurons is still unclear as the applications depend on indirect physiological measurements or imaging technologies. Subsequently, the last decade has seen an increasing interest in individual cell behavior in case of magnetic stimulation and efforts to improve patient experience leading to smaller and smaller coil designs and their characterization [61]. This recent field of assessing the capabilities of sub-millimeter coils to modulate neuronal behavior is called micro-scale magnetic stimulation.

To further this field of study, Bonmassar et al. conducted an in-vitro study using commercially available inductor, with the inductor measurement in sub-millimeters [62]. They accompanied the in-vitro experiment with Finite-Element Analysis to study the accompanying electric fields. Their efforts were soon followed by successful proof of neuron excitation using micro-scale coils in- vivo [63] [64]. An important issue raised by these studies was high power consumption by the sub-millimeter coils. This led to further research on different coil designs where different geometries were examined for cortical excitation, reporting significantly lower power consumption for applications where these coils can be as close as 300 nm to the target neurons [65].

In addition, Lee et al. showed that printed metal traces measuring 50 μm x 100 μm

in dimension were able to induce neuronal activity in cortical pyramidal neurons from a distance of $\sim$300 nm (thickness of the insulation layer), and their simulations suggested that this stimulation may not be effective beyond a distance of $\sim$75 μm from the edge of the coil [66]. While these results are promising, they raise the question of whether remote stimulation of neurons from a distance of $\sim$300 μm can be achieved through printed coils or not, where 300 μm is the approximate distance between the coils implanted inside the Scala tympani and neurons present inside the modiolus of the cochlea. Hence, we also explore the fabrication of a planar coil, inspired from this body of work. Table 2.1 compare the stimulation parameters used in other micro-magnetic stimulation studies to the parameters used in this thesis. While this comparison is not exhaustive, it provides a fair representation of the studies performed in this field.

Table 2.1: Comparison of micro-magnetic stimulation parameters [66] [63] [67] [65] [62].

	Lee (2016)	Lee (2017)	Park (2013)	Lee (2015)	Bonmassar (2012)	This thesis
Amplifier gain (V/V)	5.6	2.87	5	2.87	4.6	4.3
Stimulation Pulse type	Single full-period 3 kHz sinusoid	Monophasic rectangular pulses/ sine waves	Monophasic rectangular pulses	500 Hz sinusoid, 10 cycles	Monophasic rectangular pulses	1 complete cycle of sine wave @ 2.5 kHz or 2 complete cycles of sine wave @ 5 kHz
Amplitude in	0–200 mV	1 V	100 mV	1.5 V	4–6 V	3.5 V
Amplitude out	0–1.12V	2.87 V	500 mV	4.3 V	up to 23 V	15 V
Stimulation type	Repetitive at 1 Hz	Repetitive at 10 Hz	Repetitive at 2 Hz	Repetitive at 1 Hz, 10 Hz and 50 Hz	Repetitive at 1 Hz	Repetitive at 2 Hz
Distance from target neurons	300 nm	100 μm	100 μm	100 μm	300 μm	50 μm
Type of neurons	L5 Pyramidal neurons	L5 Pyramidal neurons	Inferior colliculus neurons	Subthalamic nucleus	Retinal ganglion cells	Dissociated, undifferentiated cortical neurons

CHAPTER 3

MODELING INTRACOCHLEAR MAGNETIC STIMULATION: A FINITE-ELEMENT ANALYSIS

The last six years have seen an increasing interest in evaluating the feasibility of micro-scale magnetic stimulation for implantable, chronic applications. A number of studies have examined the effect of sub-millimeter inductors on different sets of cortical neurons in-vivo and in-vitro, and have used computational tools to support or further analyze their results [62] [66]. In a similar effort, our group pursued an in-vivo pilot study to examine if sub-millimeter inductors would activate the cochlear neurons in a deafened feline model [68]. In brief, silicone-coated surface mount inductors (1.0 mm x 0.5 mm x 0.5 mm) were surgically inserted into the cochlea of anesthetized felines to a depth of 8 mm - 10 mm. After verifying the deafened subjects unresponsiveness to acoustic stimulation due to the lack of auditory brain response (ABR), electrical and magnetic stimuli were applied and ABRs were recorded. ABR threshold revealed successful activation of the auditory system for inductors varying from 1 μH - 2.5 μH. The results were positive and the successful activation of the feline auditory system demonstrated that cochlear stimulation through sub-millimeter inductors is effective, raising the possibility of using these inductors, instead of the electrodes, in cochlear implants. Implementing this approach would address some of the drawbacks of conventional cochlear implants, such as (a) deterioration of stimulation electrodes over time due to surface electrochemistry, (b) tissue scarring due to foreign body reaction, and (c) need for charge balanced stimulation, the lack of which causes several side effects [69]. These potential advantages of using inductors warranted further characterization of the stimulation induced through sub-millimeter coils[1]. This chapter utilizes the tools of Finite- Element Analysis (FEA) for this purpose and evaluates the electric fields induced by sub-millimeter coils. As

[1]The terms inductors and coils are used interchangeably throughout the thesis.

the induced field strength alone does not provide much information about the excitability of neurons, the spatial distribution of these induced fields are examined in terms of the spatial gradient of these electric fields (see activating function -AppendixB). Magnetically induced fields and its derivatives are then compared with those induced electrically, with the overall goal of highlighting the differences between the two techniques and pointing out any advantages or disadvantages of one over the other.

3.1 Overview

Electrical stimulation of neurons is based on direct coupling between electric currents and electric fields. Here, the electrostatic potential ϕ, which is measured in volts and is generated through local charge transfer facilitated by implanted electrodes, is of prime importance. All analytic methods for source localization and membrane interaction are developed around this quantity [36]. In contrast, magnetic stimulation is based on direct coupling between electric fields and magnetic fields. These magnetic fields depend on the rate of change of the electric current, implying indirect coupling between electric currents and electric fields in magnetic stimulation (see Appendix A for equations). The induced electric field [V/m] is of importance in this case and most analytic methods use these fields to predict neuron behavior [70]. Hence, to compare the effects of both these stimulation techniques on the same scale, the first derivative of the induced electric field and second derivative of the electrical potential (see activating function -Appendix B) are analyzed.

Furthermore, magnetic stimulation is ill reputed for not being very power efficient and for producing unwanted heating, making the use of additional cooling panels in machines such as magnetic resonance imaging (MRI) scanners, necessary [71]. Such applications raise concerns regarding the level of power consumed and the amount of heat produced by the sub-millimeter coils. Moreover, these two parameters are essential for determining the viability of these inductors in implanted applications and hence the power consumption and heating due to the sub-millimeter coils is evaluated. We observe that the power consumption

is indeed high for the configuration of pulses used in the in-vivo study and high repetition rates produce large changes in temperature.

Finally, to relax the restriction of size on these inductors posed by the cochlea, its potential use in a vestibular application is analyzed. Vestibular prosthesis are not yet FDA approved, and the state-of-the art technology requires drilling a hole through the bony labyrinth of semi-circular canals (SCCs) to deliver stimulation [72]. We use FEA tools to analyze if a sub-millimeter inductor can modulate neuronal activity from outside the bony labyrinth to avoid the drilling of the canals. This analysis also calculates the activating function in an SCC model to predict the potential feasibility of micro-magnetic stimulation in vestibular implants.

Some of the important findings of the work presented in this chapter are listed below:

- Comparison between electrical and magnetic stimulation based on the induced activating function suggests that magnetic stimulation provides better spatial resolution than electrical stimulation.
- Power consumed by these sub-millimeter coils are high when compared to electrical stimulation on the same scale, but are considerably lower than the state-of-the art magnetic stimulation devices like transcranial magnetic stimulation probes [73].
- Even for high amplitudes of currents used in this study, the temperature changes depend on the repetition rate, suggesting that high current amplitudes are safe to be used at low repetition rates.
- The activating function analysis on the vestibular system suggests that the sub-millimeter coils can potentially be optimized for use in a vestibular prosthesis.

3.2 Methodology

This section describes the modeling approaches adopted for the finite-element analysis studies and the parameters tested. It also provides the rationale behind different values tested

and their practical implications. The software used to perform the FEA studies is COMSOL (Version 5.1, Burlington, MA), a finite element modeling software package tool. This tool solves Partial Differential Equations (PDEs) and presents the results graphically.

3.2.1 Fields induced by sub-millimeter inductors in the cochlea

COMSOL is used to model an inductor (with an inductance of $\sim$100 nH) that measures 0.5 mm x 0.5 mm in cross-section, has a quartz core, and is surrounded by 21-turns of copper coil. The dimensions of this inductor are large, so it may only be implanted in base of the cochlea. However, such inductors are easily available for experimentation (0402 packaging) hence provide a good starting point for performing analyses. The copper contacts for electrical connections are also modeled on either ends of the coil. This simulation setup is inspired from Bonmassar et al. to allow ease of validation of initial results [62]. A layer of Parylene-C is modeled around the entire assembly representing insulation (figure 3.1).

To accurately assess the effect of the the fields generated by a sub-millimeter inductor inside a cochlea, the domains surrounding the inductor are modeled to represent the cochlear environment comprising of perilymph, laminar tissue, bone and cochlear nerve[2]. The laminar tissue includes tissue that comprises the membranous labyrinth and the cells lining the Scala Tympani, the bone layer represents the osseous spiral lamina, and cochlear nerve region represents the region where spiral ganglion cell bodies are present. The electrical properties of all these layers are tabulated in Table 3.1 [74] [75] [76] [77] [78]. These layers are modeled to be homogeneous, isotropic, non-dispersive, and linear. As the relative permeability of all biological matter is close to one, discontinuities at anatomical tissue junctions are not considered in this model. Moreover, the greatest attenuation that the magnetic fields suffer is at the tissue-air interface, which is not a concern for an implanted coil, so not considered in this study [79].

To understand the features of electric fields induced by a sub-millimeter coil, a parametric

[2]Detailed description is provided in chapter 2.

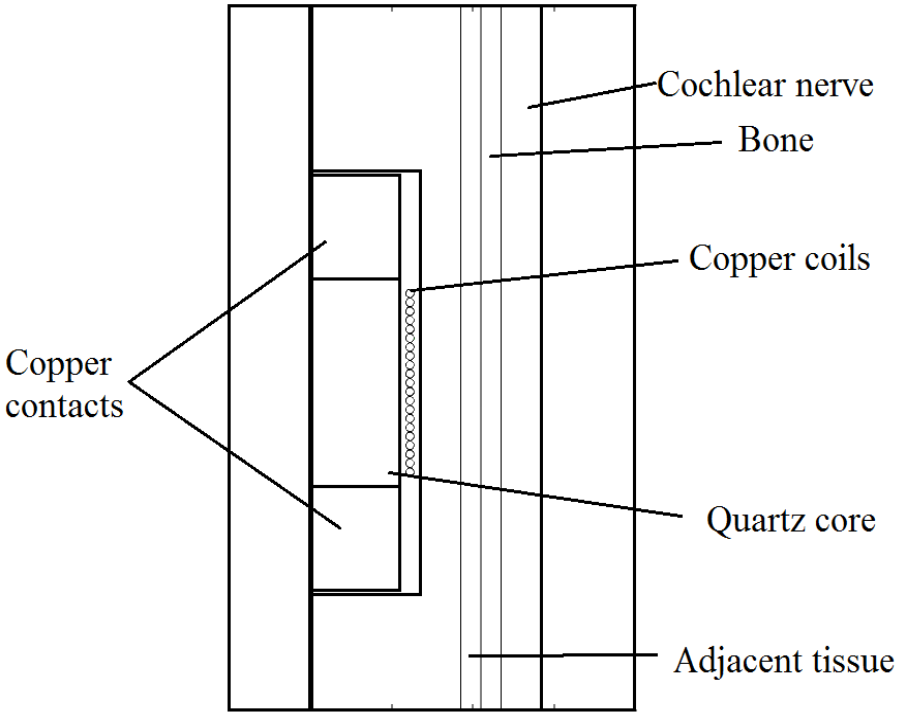

Figure 3.1: Geometry of the modeled inductor

Table 3.1: Electrical properties of materials

Material	Electrical conductivity [S/m]	Rel. permittivity	Rel. permeability
Quartz	1e-12	4.2	1
Copper	5.998e7	1	1
Parylene-C	1e-14	3.1	1
Perilymph	1.8	30	1
Tissue	0.00086	30770	1
Bone Tissue	0.02	1435.2	1
Nerve	0.03058	59931	1

study is performed on the input current pulses where the pulse width, maximum current amplitudes, and rise times are varied , with the constraint that an electric field with a peak intensity of 10 V/m must be induced in the vicinity of the coil[3] [80]. As an additional constraint, the product of pulse width and current amplitude is kept constant for all pulses, at 85 μC per pulse and is given by equation 3.1.

$$Q = I \times \Delta t \tag{3.1}$$

Here Q represents the total charge injected, I represents the electric current amplitude and t represents time. This value for Q is based on the prior pilot study and serves as an estimate of the net charge per pulse. Pulse widths in the range of 17 μs - 40 μs[4] are studied to examine the effect of amplitude and pulse width on magnetic stimulation (figure 3.2). Steeper rise times induce larger fields since the rate of change of magnetic flux density is higher in accordance with equation A.1 (Appendix A). These input parameters are listed in table 3.2.

Table 3.2: Input pulse parameters

Case	Pulse width [μs]	Current amplitude [A]	Rise time [μs]
1	40	2.125	1.5
2	34	2.5	2
3	21.25	4	4
4	17	5	5

3.2.2 Spatial distribution of induced fields

While the properties of induced electric fields are important to assess ability of a certain input pulse to modulate neuronal behavior, it does not capture the effect of the extra-cellular

[3]Literature reports that electric fields with intensity of 10 V/m are sufficient to elicit neuronal responses.

[4]The pilot study used pulses with 7 μs rise and fall times and 20 μs of hold time, making the stimulation pulse 34 μs long.

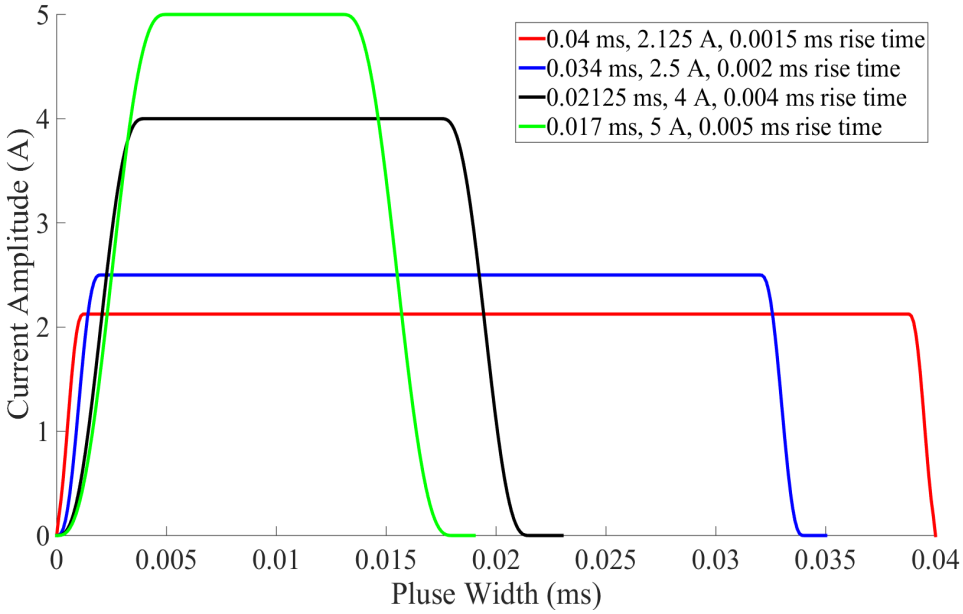

Figure 3.2: Input pulses to the sub millimeter coils with constant charge of 85 μC.

source on an axon. This effect is captured by the activating function (see Appendix B), which is a function of the distance along the axis of an axon and time. The effects of distance of the neuron from the stimulation electrode are also captured by this formulation.

As cochlear implants require an array of excitation elements to capture the incoming acoustic signals well, due to tonotopy, we simulate an array of inductors. The centers of any two consecutive inductors are placed 2 mm apart similar to contemporary cochlear electrode arrays. Then, an array of electrodes similar to those used for electric stimulation of the cochlea are simulated as well, using the Electric Currents Physics module in COMSOL. The distance between centers of two consecutive electrodes is set at 2 mm, with an end-to-end spacing of 1 mm [21]. Both these arrays are solved for their respective Activating Functions (Appendix B).

In the original formulation of the Activating Function, Cartesian coordinates are used, whereas COMSOL uses a cylindrical coordinate system to take advantage of the axial symmetry of an inductor's geometry. So, the axon is assumed to be aligned along the x direction in the original formulation, but it is assumed to be aligned along the z-direction

in COMSOL (figure 3.3 elucidates this difference). While z in the original formulation is used to represent the distance between the stimulation electrode and axon, in case of cylindrical coordinates, this information is captured by r. This is a crucial observation because COMSOL can calculate the derivative with respect to any dimension specified, hence the correct dimension must be specified to obtain accurate results.

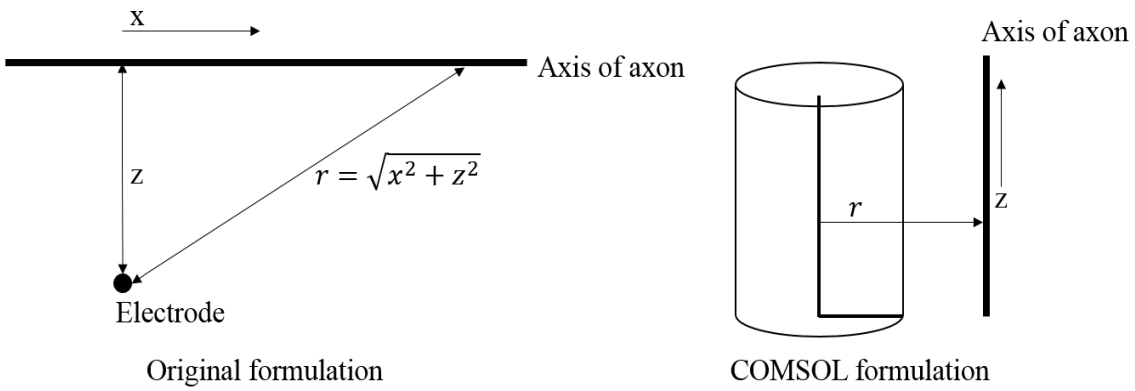

Figure 3.3: Original formulation of activating function as compared to the formulation in COMSOL

3.2.3 Heating in the cochlea

COMSOL allows the use of multiphysics such that PDEs from one study may be linked to PDEs from another physics study, thereby enabling the study of coupled effects. In this section, the magnetic field solver is coupled with a heat-transfer solver to analyze the heat produced during micro-scale magnetic stimulation. The heat transfer is studied as a stationary study where the ohmic loss from the inductor is specified as a steady state heat source and the propagation of the heat produced is studied. Two rates of stimulation are analyzed: (a) 1 Hz, as used in the pilot in-vivo study, and (b) 3 kHz, as used in most commonly implanted cochlear implant arrays[5].

[5]Though rates as high as 83 kHz have been used to transmit signals to the electrode arrays in CIs, the advantage of using high stimulation rates is not well established [69].

Table 3.3: Relevant human cochlear dimensions

Cochlear structure	Measure	Size
Scala tympani base	diameter	500 μm
Scala tympani apex	diameter	200 μm
Length of the cochlea	length	28 - 35 mm

3.2.4 Alternate coil design

The inductors modeled in the above studies measure approximately 1mm x 0.5 mm x 0.5 mm, making them non-ideal for implantation inside the cochlea that has much smaller dimensions as listed in table 3.3. So, we considered fabricating a set of coils that would fit inside the cochlea. The first step towards this goal was looking at how the induced fields changed with a different coil design. We decided to analyze a planar coil, keeping the ease of fabrication in mind. The dimensions of this coil are modeled to match the feature sizes that are practically achievable through micro-fabrication or printing. Chapter 6 further elaborates the work toward printed micro-coils.

3.3 Results

Results from the simulation studies are presented in this section. Each result is analyzed and its significance is highlighted. Physical quantities such as amplitude of the induced electric fields and heat produced are plotted as a function of distance from the inductor.

3.3.1 Electric fields induced in target tissue depends on the orientation of the inductor

Two different orientations of the inductor, with respect to the target tissues, is evaluated. In the first case, the long axis of the inductor is placed parallel to the assumed axis of the neuron bodies (figure 3.4a). In the second case, the cell bodies and the tissue surface are modeled to be perpendicular to the long axis of the inductor (figure 3.4b). The fields induced

in the surrounding tissue is calculated and this is represented qualitatively in the insets of figure 3.4. The induced fields are also plotted as a function of the distance from the tissue surface, after passing through the conductive perilymph, as seen in figure 3.5. The three colored sections in both these figures represent laminar tissue (cyan), bony labyrinth (dull yellow) and the cochlear nerve (light purple). Each of these layers is modeled to be 50 μm thick [81] and the distance between the edge of the coil and this tissue surface is kept at 100 μm, consistent with the distance between a thin film electrode array and the modiolus (figure 2.2) as measured via micro x-ray computed tomography imaging [82].

Figure 3.6 shows a one-on-one comparison of the highest induced electric field amplitudes in the two orientations. It is observed that the fields in parallel configuration are almost an order of magnitude higher than the fields in the perpendicular orientation.

3.3.2 Magnetic stimulation has better spatial resolution than electrical stimulation

Figure 3.7 shows Activating Function for a conventional electrically stimulated electrode array and the proposed magnetic array. In the electrically stimulated array, one electrode is the source and another electrode is the sink. Injected current flows between these two electrodes through the surrounding tissue, stimulating neurons en route. In the magnetically stimulated array, the source and sink regions lie within a single inductor, depending on the direction of flow of current. It can be seen from figure 3.7 that the regions likely to be depolarized[6] using electrical stimulation span more than the size of the electrode itself whereas, for magnetic stimulation the regions likely to be depolarized and hyper-polarized are much smaller. This observation is further corroborated by similar observations made by Lee et al. where they show that they can selectively excite neurons in-vivo using sub-millimeter coils [83].

[6]The terms depolarization or activation are used interchangeably to represent excitation of a neuron, or generation of an action potential, whereas the terms hyper-polarization or deactivation are used to represent the suppression of an action potential or inhibition of neuronal activity.

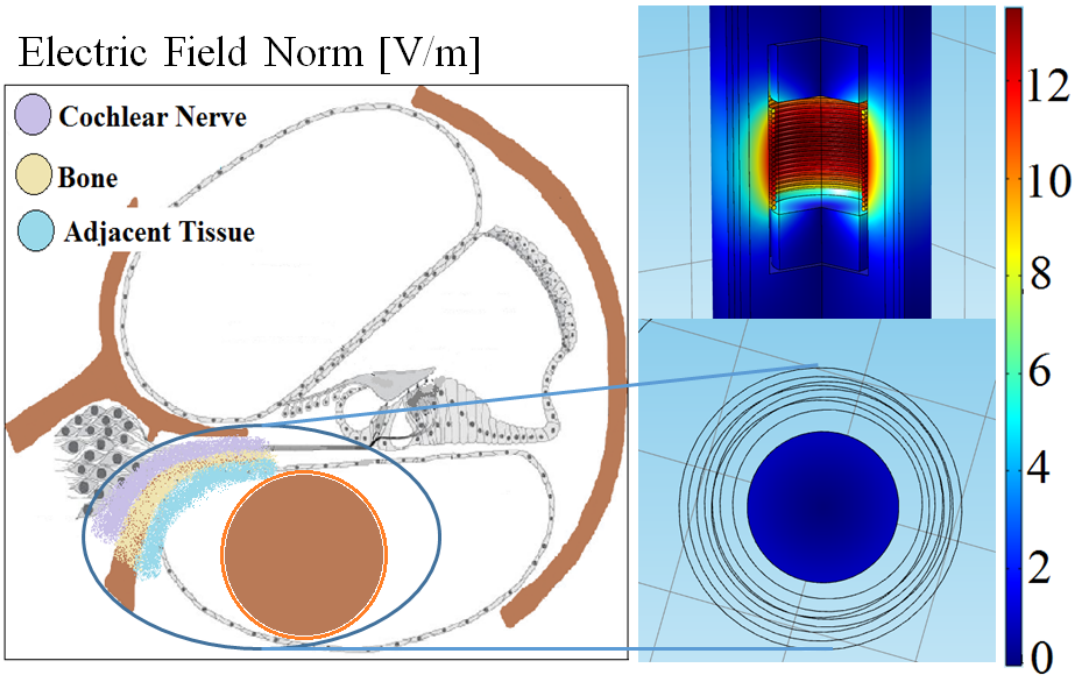

(a) Parallel orientation

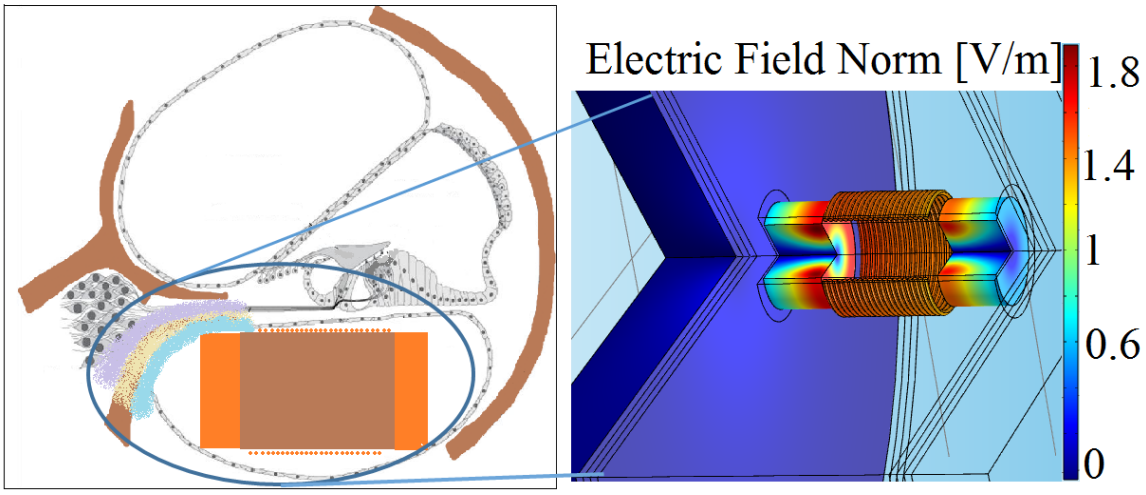

(b) Perpendicular orientation

Figure 3.4: (a) Schematic picture illustrating the placement of the inductor inside Scala Tympani parallel to the tissue surface (colored sections); Inset: COMSOL simulation of fields induced by inductor into surrounding material when inductor is placed parallel to the tissue surface. (b) Placement of the inductor inside Scala Tympani perpendicular to the tissue surface (colored sections); Inset: COMSOL simulation of fields induced by inductor into surrounding material when placed perpendicular to the tissue surface. For image (a) the inductor in inset is turned 90 degrees into the plane to appear as shown. For image (b), the inductor in inset does not undergo any transformation.

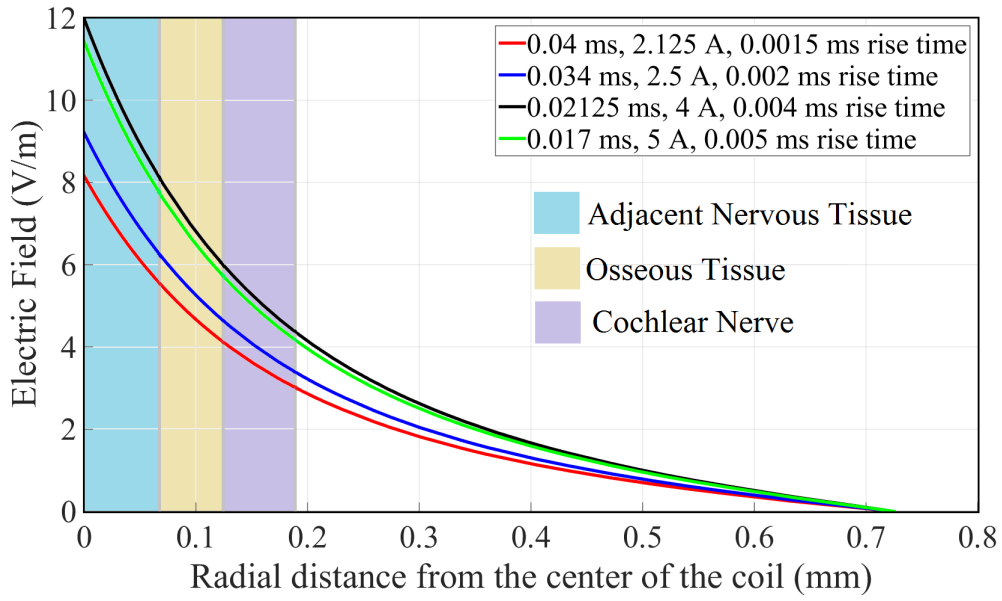

(a) Parallel orientation

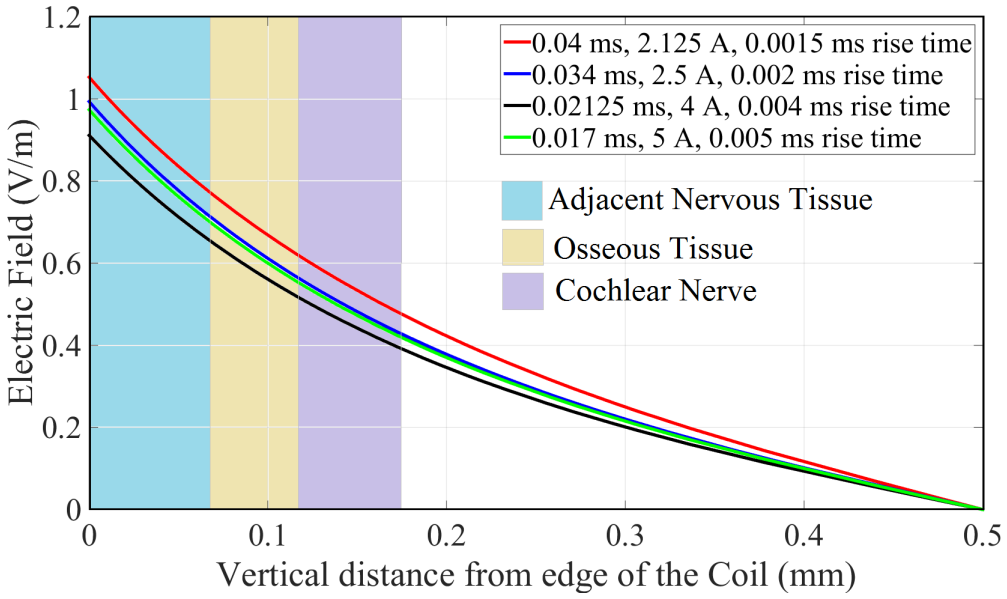

(b) Perpendicular orientation

Figure 3.5: (a) Electric field produced by sub-millimeter coils when placed parallel to the tissue surface as a function of radial distance from the coil; (b) Electric field produced by sub-millimeter coils when placed perpendicular to the tissue surface as a function of vertical distance from edge of the coil. Both cases use excitation parameters from Table 3.2 and zero on the horizontal axis corresponds to 100 microns in the *r* direction from edge of the coil.

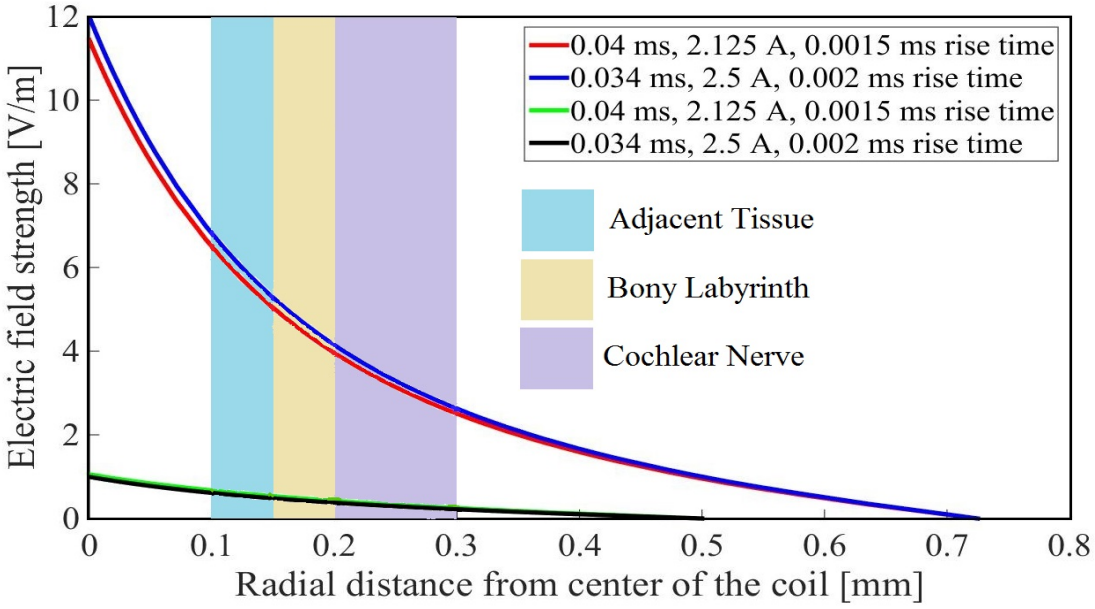

Figure 3.6: Comparison between fields induced by parallel and perpendicular orientations. The red and blue lines represent fields induced in parallel orientation and the green and black lines represent the fields induced in perpendicular orientation.

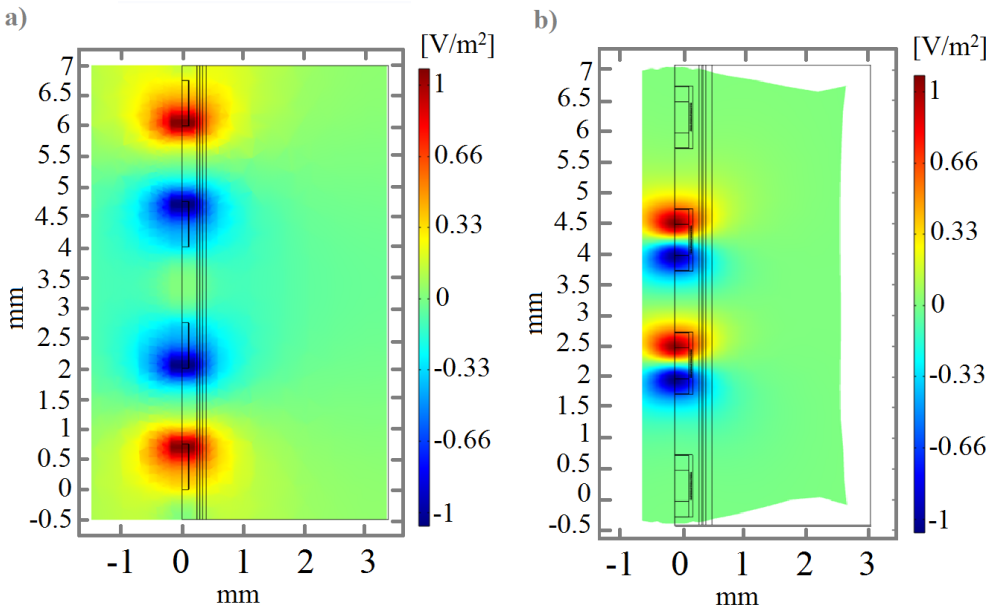

Figure 3.7: (a) Activating Function for a conventional electrically simulated electrode array with two active electrodes. (b) Activating Function for an array of inductors. Local depolarization and hyper-polarization regions can be clearly seen for the two active inductors adjacent to each other. (For equations, refer to Appendix B)

3.3.3 Power consumption for pulsed stimulation

The power consumed by each of the pulses tabulated in table 3.2 is evaluated at two different frequencies- 1 Hz and 3 kHz. For in-vivo and in-vitro experiments, the tested rate of stimulation is usually low, so that the effect of stimulation can be analyzed. Hence, the power consumption at 1 Hz of repetition rate is calculated. On the other hand, cochlear implants require a high stimulation rate to adequately encode the recorded sounds. While the stimulation rates vary a lot from one coding strategy to another, 3 kHz is considered an efficient stimulation rate [69]. So this is chosen to be the other frequency at which power consumption is evaluated. These results are presented in table 3.4.

Table 3.4: Power consumed by pulsed currents

Pulse width [μs]	Current amplitude [A]	Power consumed at 1 Hz [μW]	Power consumed at 3 kHz [W]
40	2.125	309.6	0.9288
34	2.5	364.48	1.093
21.25	4	583.1	1.7493
17	5	728.79	2.186

3.3.4 Stimulation at high rates results in large temperature changes

The stimulus pulse corresponding to 40 μs pulse width is selected for the heating study because this pulse consumes the least power, hence is most likely to be used in practical implementations. Heating caused by this pulse at a repetition rate of 1 Hz and 3 kHz is calculated and presented in figures 3.8 and 3.9.

3.3.5 Planar coils offer less directional dependence for magnetic coupling

The coils modeled in this study are essentially the magnetic equivalent of a capacitor that are used to store magnetic energy. However, we require our coil to dissipate its magnetic energy, so that it may be utilized towards neuronal modulation [84]. One such design is that of a

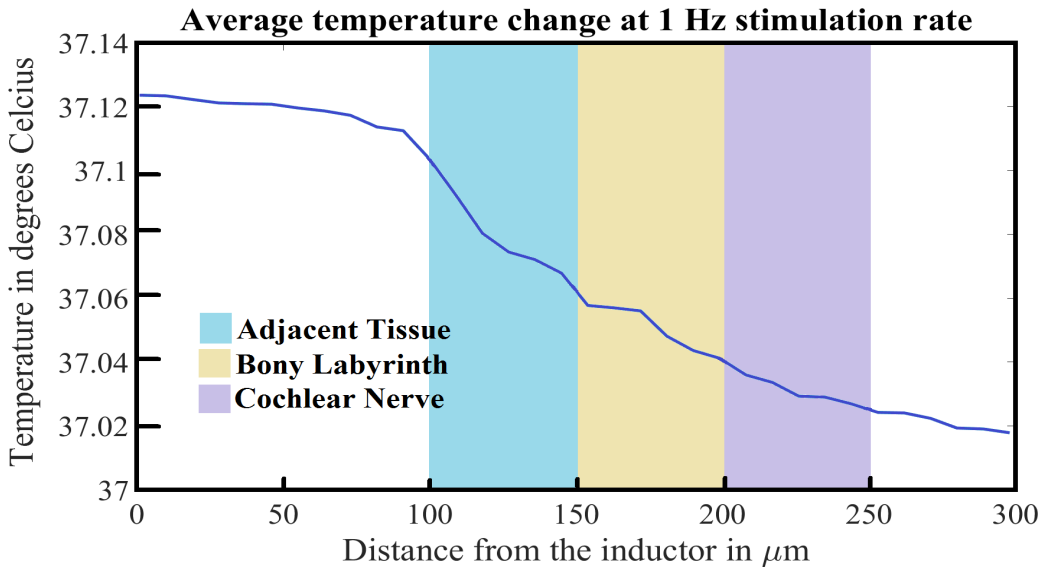

Figure 3.8: Temperature change due to a 40 μs wide trapezoidal current pulse with peak current of 2.125 A and rise time of 1.5 μs, at a repetition rate of 1 Hz.

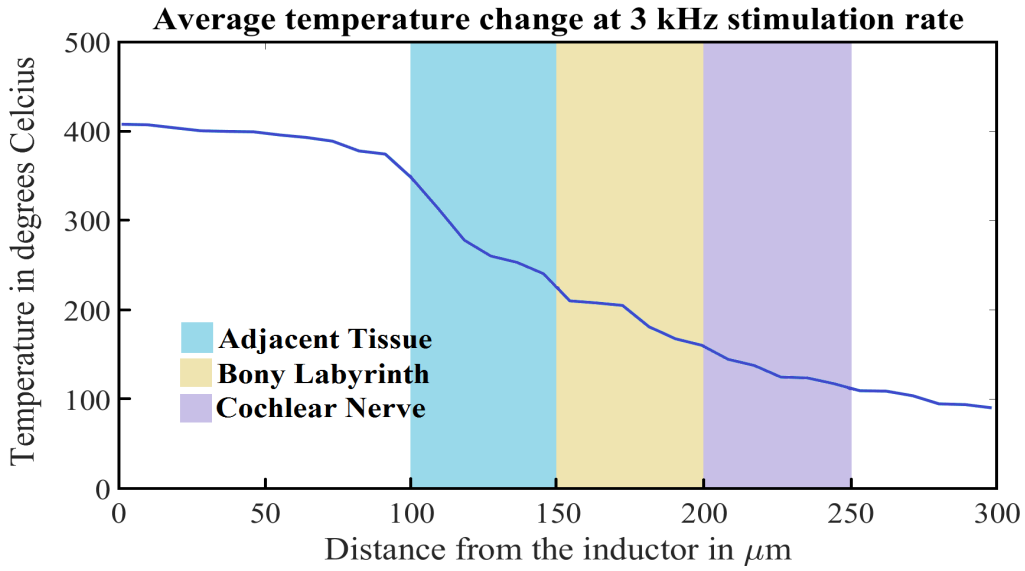

Figure 3.9: Temperature change due a 40 μs wide trapezoidal current pulse with peak current of 2.125 A and rise time of 1.5 μs, at a repetition rate of 3 kHz.

planar coil. So, we model a planar coil and analyze the features of the electric fields induced by it. An advantage of planar coils is that it is much easier to fabricate than a wire-wound inductor. The modeled coil is shown in figure 3.10 and the fields induced by it are analyzed.

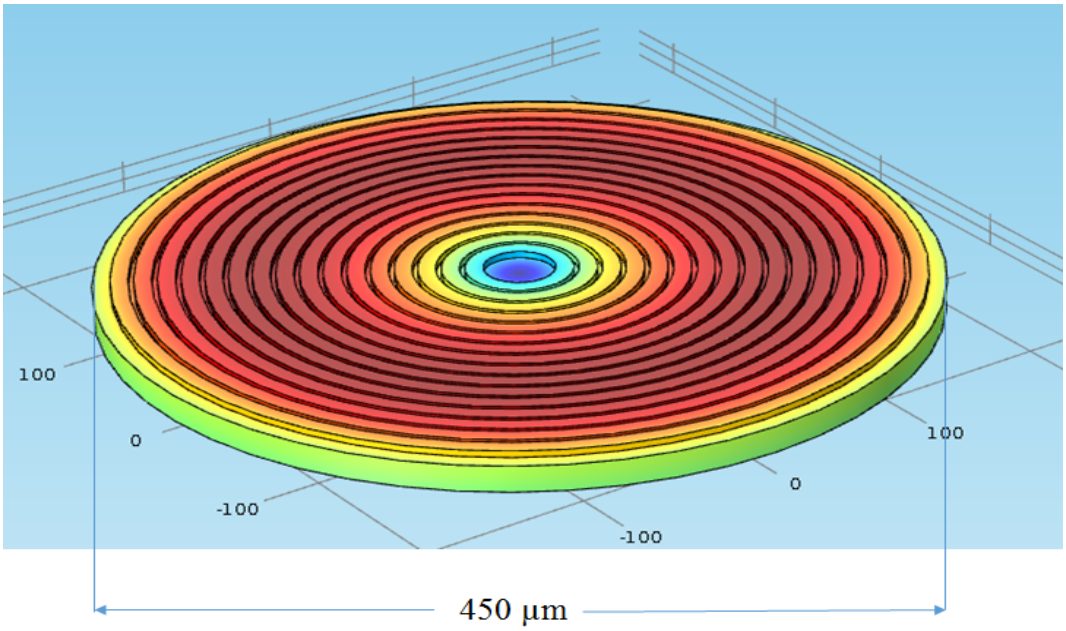

Figure 3.10: A planar coil is modeled with traces that are 30 μm wide and 5 μm high. This coil has 16 turns. The outer diameter of this coil is 450 μm and its inductance is 46.9 nH.

3.3.6 Observations

OBSERVATION 1: The target tissues see higher magnetic coupling with the inductor (as evident from the intensity of the induced electric fields) when the long axis of the inductor is aligned parallel to the tissue surface. This coupling is much lower when the axis of the inductor is perpendicular to the tissue surface.

OBSERVATION 2: An array of inductors show narrow regions of potential activation and deactivation when compared to similar regions produced by an array of electrical stimulation electrodes. This selectivity of stimulation is an advantage in the cochlear implant application, as it promises better frequency resolution.

OBSERVATION 3: Power consumption is directly proportional to the peak current values corresponding to each of the stimulation pulses. Shorter pulse duration offsets the

average power consumption a little but the effect of peak current amplitude dominates.

OBSERVATION 4: The steady-state temperature at the stimulation rate of 3 kHz is very high, suggesting that these coils are not safe for implantation if the tested parameters are used. However, the temperature change at a repetition rate of 1 Hz for the tested parameters is moderate. This result suggests that such low stimulation rates are not likely to induce thermal stimulation in neurons during in-vivo and in-vitro experiments [85].

OBSERVATION 5: Planar coils showed less directional dependence between parallel and perpendicular configurations with a difference of only 3 V/m in the peak induced electric fields. The power consumption was slightly lower in this configuration, but not very different.

3.4 Summary

In this work finite element analysis is used to characterize magnetic stimulation delivered through sub-millimeter inductors. The electric fields induced by a 100 nH inductor in a cochlear environment, when driven with current pulses with different amplitudes (2.125 - 5 A) and pulse widths (17 - 40 μs), is calculated. To analyze the effect of these fields on cochlear axons, the contribution of these fields towards neuronal modulation is evaluated in terms of the activating function. Then the power consumption and heating at different repetition frequencies is calculated. An alternate coil that promises better coupling with the neurons is also modeled. These analyses provide the following insights into micro-scale magnetic stimulation:

- Orientation of the inductor with respect to the axis of axons has an effect on the coupling between the inductor and the axon.
- Magnetic stimulation is more likely to provide better spatial resolution, thereby implying better frequency resolution in case of cochlear implants, based on comparison of activating function between electrical and magnetic stimulation.

- Power consumption and heating become a limiting factor at high repetition rates for the input pulses analyzed in this study.

3.5 Magnetic stimulation for vestibular implants: second-use case

This section talks about a finite-element study performed to assess the potential feasibility of magnetic stimulation in vestibular prosthesis. The induced electric fields are calculated and the activating function is computed and compared to those induced electrically. Heating and power consumption are also evaluated with the aim of developing better understanding of the advantages and limitations of magnetic stimulation in this application.

3.5.1 Background and motivation

The peripheral vestibular system, located in the inner ear, is responsible for detecting rotational and linear head motions with the help of five sensory organs: three semi-circular canals, which detect angular head acceleration, and two otolith organs, which detect gravity and linear acceleration. The three semi-circular canals, which are roughly aligned with the three spatial dimensions (x, y, and z) and which are filled with a viscous fluid called endolymph, are the anterior, posterior, and horizontal, or lateral, canals. These canals are attached to the vestibule at both ends. They expand at one of these ends to form an ampulla that houses the hair cells, or cilia, responsible for detecting angular head acceleration by encoding the movement of endolymph as the firing rate. This angular head acceleration is quantified by the firing rate of the cilia, which has a baseline frequency of 100 Hz. The cilia send signals that either activate or inhibit the medial-lateral recti (eye-muscles), which results in side-to-side eye movements [86]. Such movements produce stable images on the retina that are essential for a healthy sense of balance and the lack of which often results in dizziness and nausea, a condition referred to as vestibular dysfunction.

While patients who suffer from unilateral (one-sided) vestibular dysfunction often benefit from treatments such as medicine or rehabilitation exercises, those who suffer from bilateral

(two-sided) vestibular dysfunction reap marginal benefits from these treatment options. For these bilaterally dysfunctional patients, who suffer from a severely degraded quality of life, a corrective treatment, that is provided in the form of electrical stimulation of the vestibular neurons, is essential [72]. However this corrective option suffers from drawbacks such as: (a) current spread while encoding high acceleration rates, resulting in unintended stimulation, and (b) inability to encode inhibitory responses. Furthermore, for these implants to access the vestibular neurons, drilling of the bony labyrinth is required, which may result in potential complication during surgery. To this end, magnetic stimulation is studied to see if it provides added advantages for this application.

3.5.2 Methodology

Unlike cochlear stimulation, electrodes are placed outside the bony labyrinth for vestibular stimulation, so a different geometry is modeled. Figure 3.11 shows the model used to represent the semicircular canal in COMSOL. The depicted geometry comprises of an external bony labyrinth filled with Perilymph (outer ellipse) and the a membranous labyrinth filled with Endolymph (inner ellipse). The neurons reside in the region inside the inner ellipse. Material properties listed in table 3.1 are used and the 40 μs pulse from table 3.2 is applied as an input to the coil.

3.5.3 Results

Figure 3.12 plots the Activating Function for both electrical and magnetic stimulation. The right hand side of this figure depicts the geometry that is modeled to obtain the results. For electrical stimulation, only the membranous labyrinth cross section is modeled, because electrical stimulation requires drilling through the bony labyrinth; whereas, the bony labyrinth is also modeled for the magnetic stimulation study. The amplitudes for the activating function are normalized in both case to avoid any confusion during comparison. According to the literature, amplitudes of 11.2 mV/mm^2 have been shown to produce excitation in peripheral

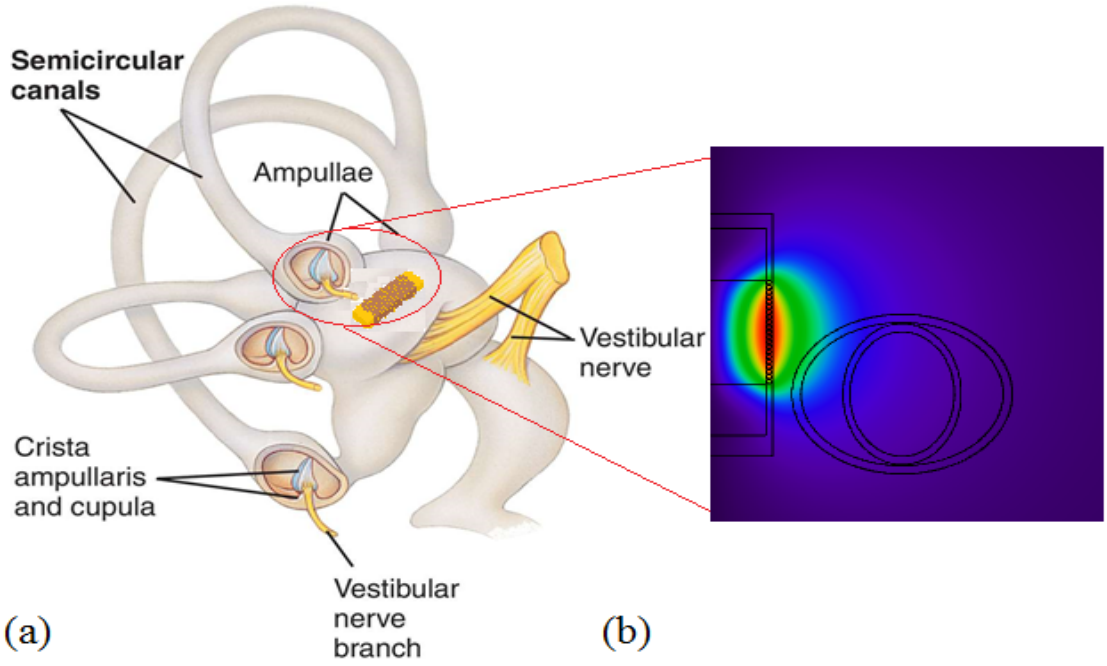

Figure 3.11: (a) Anatomy of the vestibular system. (b) Electric fields induced due to a 40 μs wide trapezoidal current pulse with peak current of 2.125 A and rise time of 1.5 μs

neurons in-vitro [87]. Values within one order of magnitude of this threshold were obtained, suggesting high likelihood of neuronal excitation.

3.5.4 Heating and power consumption

Requiring a maximum repetition rate of 500 Hz, the vestibular prostheses offer a less demanding application from the perspective of heating. However, simulating the natural functioning of SCCs requires maintaining a base firing rate which is usually around 100 Hz [88]. This implies that the vestibular prosthesis is continuously active. Therefore, frequencies of 100 Hz and 500 Hz were tested for heat generation.

The power consumed at a repetition rate of 500 Hz by the inductor described in this subsection is calculated to be 167.6 mW, and the power consumption at 100 Hz is 33.5 mW. COMSOL simulations show a change of more than 15°C in temperature at 100 Hz repetition rate and a change of over 50°C at 500 Hz. These values are steady state values, meaning if the stimulation is being applied over a long period of time, these changes in temperature

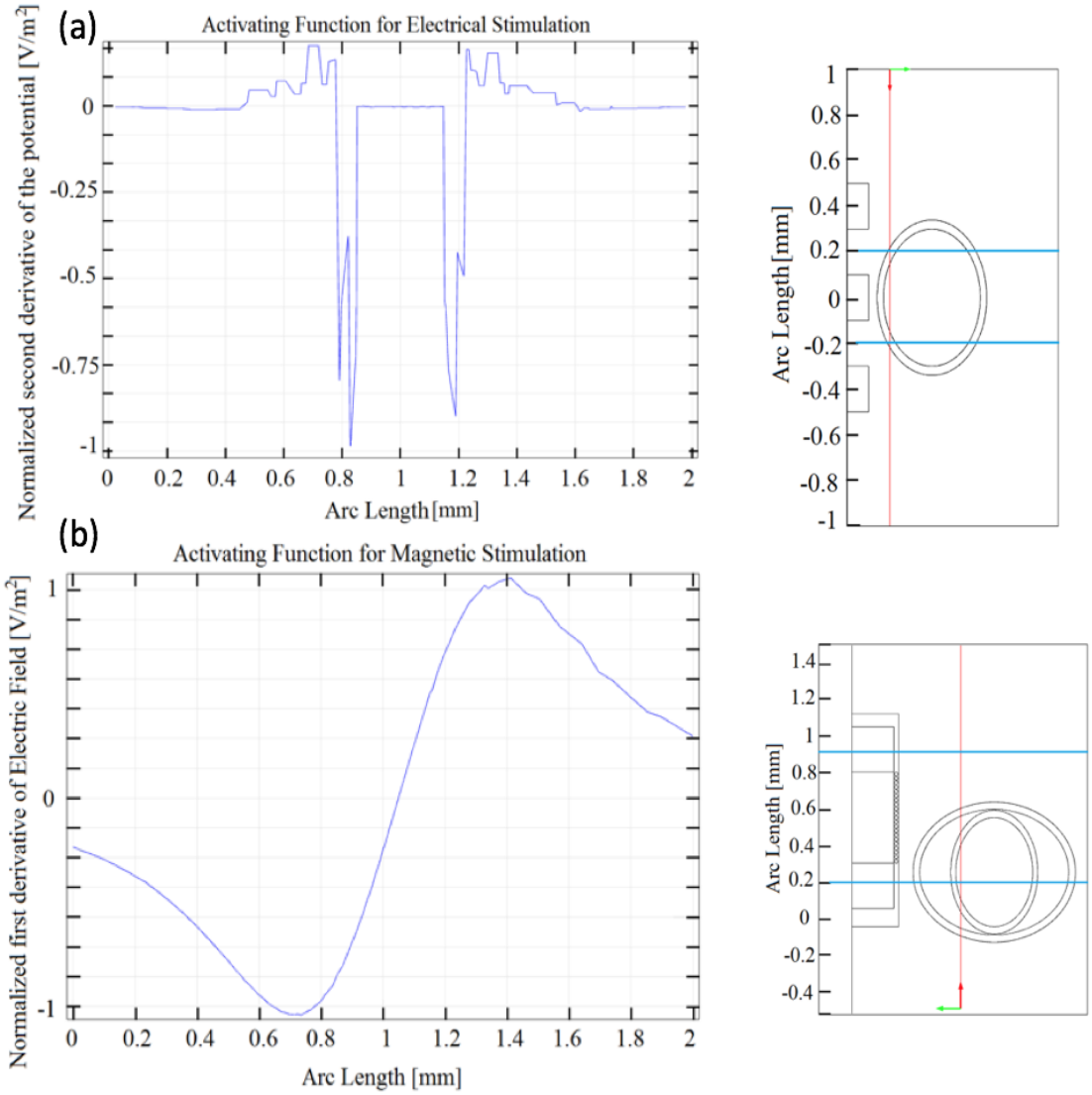

Figure 3.12: (a): This figure depicts the second derivative of potential induced (left) during electrical stimulation of the vestibular neurons present in the ampullae (b): This figure plots the first derivative of induced electric field (left) during magnetic stimulation of the vestibular neurons present in the ampullae. These potentials are along the red line in the geometry sketch on the right. The blue lines represent the regions where peaks are observed in this geometry.

will be observed. It must be noted here that heat dissipation due to blood flow or presence of surrounding fluids is ignored in these calculations, so the values obtained are the maximum possible heating produced in these regions.

3.5.5 Observations

OBSERVATION 6: The value of activating function calculated at a distance where neurons are expected to be present, suggests sub-millimeter inductors may be capable of modulating vestibular neuron activity.

OBSERVATION 7: As the modeled inductors are larger in size than the ampullae, they are likely to provide mono-polar stimulation, i.e., either activation or deactivation. This property may be useful for application in vestibular prosthesis as these devices encode either an increase or a decrease in firing rate at one point in time.

OBSERVATION 8: Large changes in temperature are observed at the inductor surface at the stimulation rates required by vestibular prosthesis.

OBSERVATION 9: The calculated power consumed for this application for a 40 μs wide pulse, with 2.125 A amplitude is 167.6 mW at 500 Hz and 33.5 mW at 100 Hz.

CHAPTER 4

EXPERIMENTAL SETUP FOR MICRO-SCALE MAGNETIC STIMULATION OF NEURONS ON A MULTIELECTRODE ARRAY

While modeling and theoretical analyses are an important part of improving the understanding of effects of magnetic stimulation on neurons, experimental validation of these analyses improves the model and highlights future needs. In the previous chapter we used finite element analysis to study the features of electric fields induced by sub-millimeter coils, and simulated its interaction with neurons in terms of activating function. We established that inductor orientation with respect to the axis of a group of axons plays an important role in its ability to induce excitation. We also demonstrated that at low stimulation rates (1 - 2 Hz), these inductors are less likely to cause thermal excitation in neurons, and that any induced activity is most likely due to magnetic coupling. We then compared electrical stimulation to magnetic stimulation and indicated that magnetic stimulation provides better spatial resolution as illustrated by their respective activating functions. This chapter details the methods involved in our efforts to experimentally compare the electrical and magnetic stimulation of neurons in an in-vitro setting.

4.1 Overview

Multielectrode arrays (MEAs) have been used extensively over the past decade and a half to examine the effects of electrical stimulation on dissociated cortical neurons. The knowledge base for this stimulation is rich, and several studies ranging from observing the regular life cycle of these neurons, to entraining the spontaneous bursts, based on rates of stimulation have been performed [49] [48]. As these studies require the culture to be living over a long period of time[1], several protocols have been established to optimize the reliability of data

[1]Typical life cycle being at least five weeks.

and life-cycle of these neurons. These protocols include maintaining hygiene while handling the cultures and keeping them covered at all times except when changing the media.

The external stimulus to neurons is presented in two different ways: (a) through a self-assembled magnetic stimulator, and (b) through a thin-film electrical array developed by NeuroNexus Technologies (Ann Arbor, MI) (figure 4.1). Data is recorded using multi-electrode arrays and pre-amplifiers manufactured by Multichannel Systems (Multi Channel Systems MCS, GmbH). This data is acquired and analyzed using an open-source software called Neurorighter [89]. The power consumption and heat produced during these two sets of experiments are also analyzed.

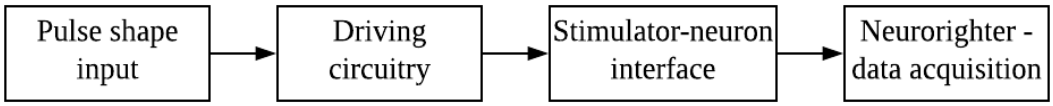

Figure 4.1: An overview of the in-vitro experimental setup.

4.2 Methodology

This section describes the methods employed to prepare the magnetic stimulator and the neuronal cultures, the components used to set up the electrical and magnetic stimulation drive, and the setup used to record neuronal activity. More detailed steps for caring for cultures and preparation of magnetic stimulator are provided in appendices C and D.

4.2.1 Preparation of the magnetic stimulator

Commercially available inductors (100 nH, MLZ2012N100LT000, TDK Corporation, Tokyo, Japan) were used to assemble a first version of the prototype magnetic stimulator, where 30-mil copper wire was soldered on to these inductors. Then this assembly was suspended from a small steel cannula tip that was attached to a glass rod using nylon cable ties. Hot glue was used to insulate the inductor and the surrounding solder, then this

stimulator was connected to the driving circuit. A micro-manipulator (MX6600 AutoMate Scientific, Inc, Berkeley, CA) was used to precisely control the position of this stimulator inside the well of the MEA, with a precision of 20 μm.

This first prototype was valuable in performing some preliminary tests such as debugging amplifier noise and recording and analyzing stimulation artifacts. However, this setup was crude and the use of hot glue did not allow precision in the thickness of the insulation layer. Additionally, some of such inductor assemblies broke down after a few electrical tests, due to the brittleness of the connecting wire. So, a new set of stimulators were assembled using 34-AWG copper wire (Belden, Richmond, IN, USA), a plastic pipette for precise placement of the inductor, and were insulated with a conformal, precise 10 μm layer of Parylene-C. The final magnetic stimulator is shown in figure 4.2. The protocol for assembling this stimulator is as follows:

- Use sand paper to strip off the ends of the 34-AWG copper wire.
- Use solder flux and 15-mils solder wire (Kester, Itasca, IL, USA) to solder the copper wire onto the inductors. Since the inductors are small, it is useful to have tweezers hold the inductor in place and a microscope or magnifying glass to see where to solder.
- Attach the inductor and wire to a plastic pipette using super glue, give it time to stick together. A micro-manipulator is used to keep the plastic pipette suspended while being glued to the soldered inductor, this allows the inductor to be precisely where it is intended to be for the experiments.
- Insulate the entire assembly using Parylene-C, a bio-compatible polymer capable of providing pinhole free insulation.

When this assembled magnetic stimulator is inserted in the media[2] containing cells for

[2]Media is like food for the culture and is optimized to provide necessary nutrients for its survival. There is a need for changing this media every few days to replenish the nutrients. More details are provided in following sections and Appendix-C.

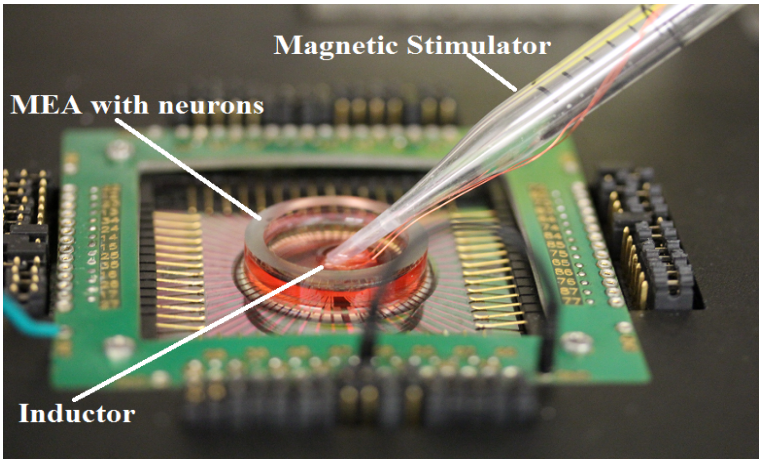

Figure 4.2: An image of a magnetic stimulator tip in MEA with cells

Table 4.1: Comparison of resistance across inductors due to Parylene-C coating

Inductance value	Ω dry	Ω in PBS	Ω in PBS after coating
100 nH	2.8	2.5	2.4
1 μH	1.5	1.6	1.4
1 μH	1.8	1.7	1.2
1 μH	1.5	1.4	1.2
10 μH	2.9	2.9	2.9

experiments, the inductor and media behave like two plates of a capacitor and the Parylene-C coating acts as the dielectric between them. So, while the Parylene-C coating is known to be pin-hole free at a thickness of 5 μm, an additional 5 μm is coated, to reduce this capacitive coupling between the inductor and the media. To see the effect of the Parylene-C coating on the inductors, they are submerged in an dish containing phosphate buffered saline (PBS) solution, and the resistance across these inductors is measured before and after the coating. These values are reported in table 4.1. A general reduction in the resistance value indicates that the Parylene-C coating is effective. Without the coating, the applied currents had the option to flow across the PBS solution, even though it is a higher resistance path. With the coating, this alternative path for the flow of current is eliminated, hence lower resistance values are observed.

The electrical stimulator

The electrical stimulating array is prepared by gluing a Polyimide thin-film array by NeuroNexus on to a 250 mm glass rod (ANK-Trade, Amazon.com) using super-glue (figure 4.3). This array was coated with a thin layer of silicone for mechanical stability in a prior work by our group [82]. The AutoMate micro-manipulator is used to precisely lower this electrical stimulator into the MEA well containing the culture, and stimuli are delivered using the PlexStim 2.0 (Plexon Inc., Dallas, TX) electrical stimulator.

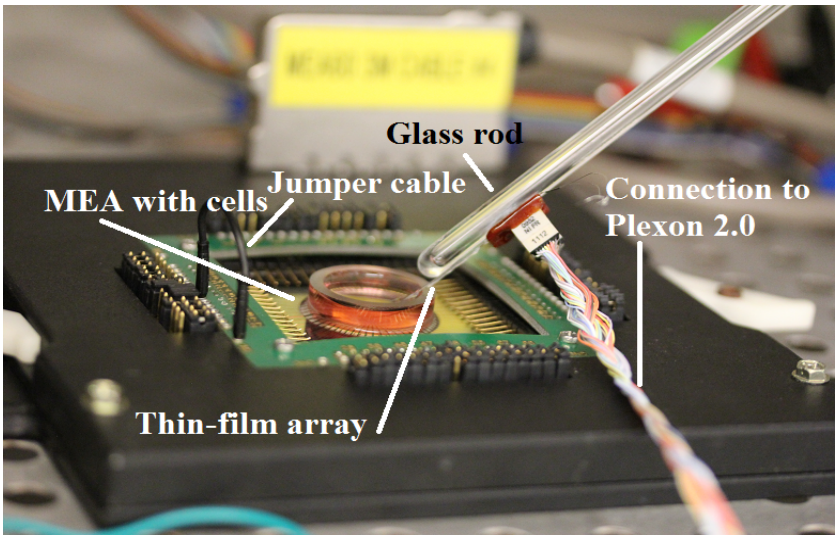

Figure 4.3: An image of the electrical stimulating array inserted into an MEA well for external electrical stimulation. The black jumper cable is connecting the ground electrode on MEA to the ground pin on MCS amplifier.

4.2.2 Electrical and magnetic stimulation drive

Three different types of stimulation are used to study the response of neurons to external stimuli. They are: (a) external electrical stimulation, (b) external magnetic stimulation, and (c) MEA-electrode delivered electrical stimulation. The MEA-electrode delivered electrical stimulation is used as a preliminary control to see whether the cultures are responding to stimulation or not. In some cases, when the cultures are too young (DIV 11-12)[3], they do

[3]DIV stands for days in-vitro.

not respond robustly even to MEA-electrode stimulation. This implies that it is less likely for them to respond to any other kind of stimulation. The following subsections describe the respective driving circuitry for each of these stimulation types.

Thin-film array driving circuitry

A PlexStim 2.0 (Plexon Inc., Dallas, TX) electrical stimulator is the core of the driving circuitry for external electrical stimulation. This stimulator is connected to a 60-Hz power supply and a personal computer to be fully operational. A software, which is required to define the stimulus pulses, needs to be downloaded from Plexon's website. To deliver stimulus to the thin-film array, the array manufacturer has provided two 16-channel connectors (Omnetics Connector Corp., Minneapolis, MN) bonded to the back-end of the array for signal transfer. These connectors are connected to the PlexStim 2.0 via a breakout box (figure 4.6). The default wiring of the breakout box allows access to electrodes 1, 2, 3 and 4 (figure 4.4), out of which electrode 1 is used for all the experiments reported in this chapter. The stimulus pulses tested are biphasic current pulses with amplitudes of 250 and 500 μA, and a pulse width of 200 μs per phase. These pulses are designed so that the negative phase is presented first (figure 4.5). The repetition frequency is varied between 2 -5 Hz.

The driving circuitry for magnetic stimulation

The driving circuitry for the preliminary and the final set of experiments consisted of the following components:

- Pyramid PB717x 1000W audio amplifier
- Agilent E3634 A DC power supply for the amplifier
- Agilent 33522A 30 MHz function/ arbitrary waveform generator
- Neurorighter for input waveform recordings

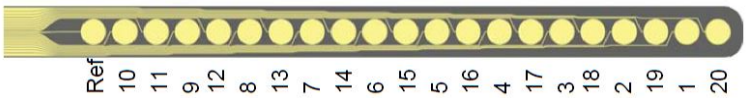

Figure 4.4: A picture illustrating the electrodes on the thin-film array. This Polyimide array measured 27.8 mm x 0.4 mm x 20 μm (L x W x H) with 20 functional platinum sites 180 μm-diameter, 250 μm-pitch).

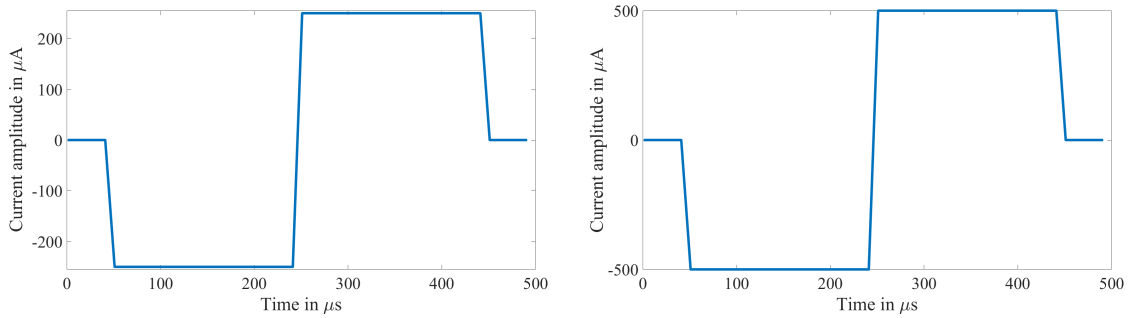

(a) 250 μA biphasic pulse

(b) 500 μA biphasic pulse

Figure 4.5: The pulses used for electrical stimulation of neurons, and for other studies without neurons.

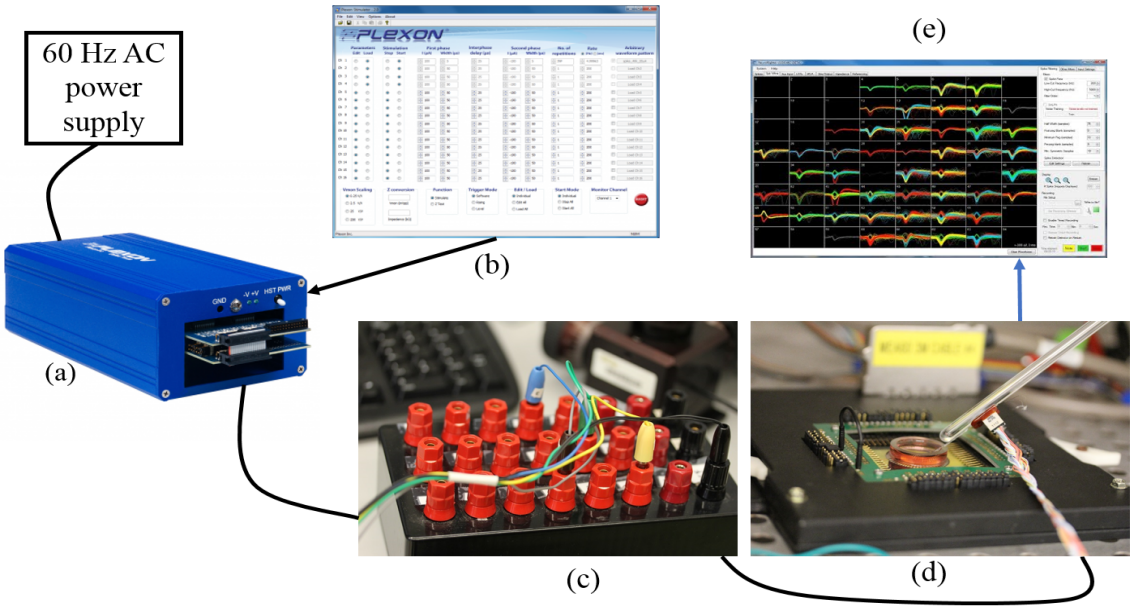

Figure 4.6: A block diagram of the electrical stimulation circuit that was used to drive biphasic waveform into the thin-film array. Here, (a) represents the Plexon 2.0 stimulator, (b) represents the Plexon GUI, which is used to define biphasic pulses, (c) represents the breakout box that connects the stimulator to the electrode array, (d) is an image of the electrode array interfacing with the MEA, and (e) represents Neurorighter for data acquisition.

- Connecting wires and BNC cables

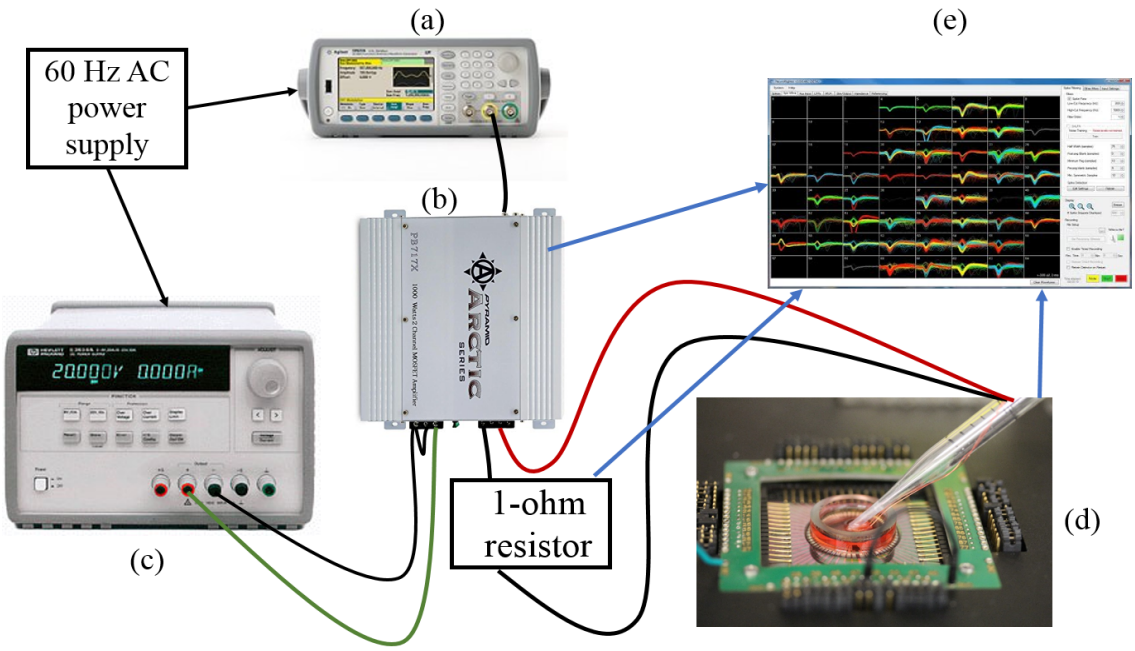

Figure 4.7: A block diagram of the driving circuit for magnetic stimulation. Here, (a) represents Agilent 33522A 30 MHz function/ arbitrary waveform generator, (b) represents Pyramid PB717x 1000W audio amplifier, (c) represents Agilent E3634 A DC power supply for the amplifier, (d) represents the inductor which is connected in series with a 1-Ω resistor, and (e) represents Neurorighter for input waveform recordings.

Figure 4.7 shows a block diagram representing this driving circuitry. Waveform from the Agilent 33522A waveform generator is applied as input to the Pyramid amplifier, which has a gain of 4.3 V/V. The amplifier is observed to introduce distortions or non-linear behavior at frequencies higher than 12 kHz and for voltages higher than 5 V. As a consequence, all experiments are performed within these limits, to avoid any non-linearity in the setup. The range of stimuli tested are presented in table 4.2. All stimuli are presented at a repetition rate of 2 Hz and the average experiment time for recording neuronal response is five minutes. In some cases, ten minutes long experiments are also performed, to study the spontaneous change in neuronal behavior in this time frame.

Table 4.2: Stimulation parameters tested during magnetic stimulation

Voltages [V]	0.175 - 4
Frequencies [kHz]	2.5 - 10
Number of cycles per pulse	1 - 4

MEA-electrode delivered electrical stimulation

MEA-electrode delivered electrical stimulation uses the Neurorighter graphical-user interface (GUI) (see section 4.2.5) in conjunction with a set of in-house stimulator modules (figure 4.8) [90]. The stimulus amplitude and pulse-width are modified using this GUI, and a basic MATLAB script is written to specify which electrodes to stimulate along with the specified frequency. For the purposes of control during our experiments, the stimulation electrode is randomized and biphasic stimulus pulses with amplitude of $\pm$ 0.9 V and pulse-width of 200 μs are delivered at 2 Hz. This allows us to screen the culture and note which electrodes are responding to the applied stimulus. Once a culture is confirmed to have multiple electrodes that record a response to stimulus, it is considered good for further testing. Multiple electrodes recording a response to stimulus indicates that the culture is in good health and has sufficient number of neurons in good contact with MEA electrodes. For this set of experiments, the MEAs are able to maintain sterility as there is no need to take off the Teflon cap which protects the culture from surrounding contaminants.

4.2.3 Preparation of cultures for in-vitro analysis

Plating is the process of spreading a sample of cells or microorganisms on a nutrient media in a petri dish. For our research we used dissociated cortical neurons of embryonic day 18 rats received from BrainBits LLC (Springfield, IL) and spread them on the area inside the well[4] of an MEA. The plating density is 1000-3000 cells per μL, and $\sim$20 μL of dilute cell

[4]Each MEA from MCS systems comes with a choice of well material, and an option to get an MEA without a well. Figure 4.11a shows an image of an MEA with a plastic well.

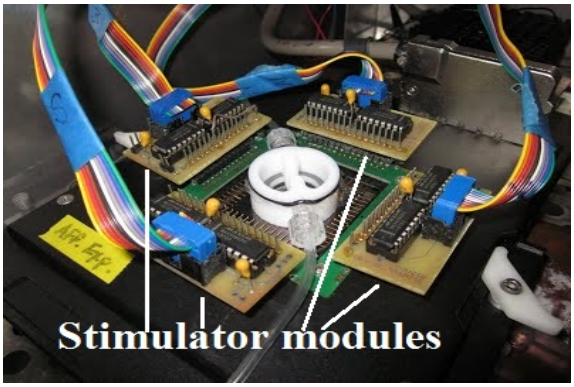

Figure 4.8: Stimulus multiplexing boards to deliver the stimuli from Neurorighter to the MEAs (Courtesy: Neurorighter Google sites).

suspension is applied to each MEA[5]. To get an average count of cells plated per dish[6], an extra dish is plated, the cells from which are stained and counted. Prior to the plating, the MEAs are washed with a mixture of Tergazyme (soap) mixed to instructions (1g per 100 ml of water), overnight, at 36°C, while being stirred in a water bath. For sterilizing the MEAs, they are soaked in ethanol for 30 minutes while under UV light in a laminar flow hood, then they are left to dry overnight under UV light. Figure 4.9 presents an image of a DIV 21 culture. The high density of cells at the center of the MEA can be seen here.

For the first couple of weeks after plating, the cultures go through three cycles of full media change per week, followed by at least two cycles of media changes for the remaining weeks. The media proposed by Jimbo et al. is used to maintain the cell cultures as it has been observed to maintain high levels of activity in neurons [92]. After 16 complete days of maintaining these cultures, they are considered ready for testing. To deliver external electric and magnetic stimulation, the stimulator tips are first sterilized with ethanol and then inserted in the glass well filled with media for the experiments.

These plated cultures have a variable life cycle. They have been known to live for as long as a year, if proper care is taken. However, performing non-sterile experiments on them places them at a great risk of infection. Moreover, cultures can detach from the MEA

[5]The plating procedure closely follows the one outlined by Hales et al. [91].
[6]The terms *cultures* and *dishes* are used interchangeably from this point onward.

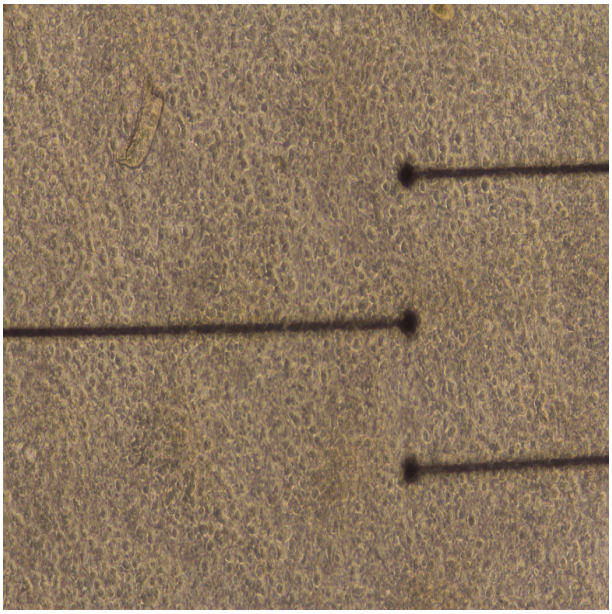

Figure 4.9: An image of the plated neurons on an MEA. It is difficult to discern the cells given their high density. The plating density is 1000-3000 cells per μL, and $\sim$20 μL of dilute cell suspension is applied to the MEA. The central three electrodes: 84, 14, and 85 are also seen in this picture (refer appendix F for map).

electrodes if they experience great force, such as, poking with a pipette tip during media change or probing with stimulator during experiments. In fact, sometimes the older cultures form large spheres of neurons, and detach from electrodes without outside disturbance, becoming too sparse to record from.

For the experiments reported in this thesis, three sets of plating were performed on 7 seven different MEAs. The first set of plating involved three MEAs that are referred to as A1, A2, and A3. In the second plating, five MEAs were plated. These include A2 from the previous set, which acquired an early infection and had to cleaned off. These are referred to as B1, B2, B3, B4, and B2A (the replated MEA). The third plating used MEAs A3, B2, and B3, as all of these were also lost to infection, and these are referred to as C1, C2, and C3. A1 was the longest living culture that lasted around 45 days and eventually detached from the MEA without external disturbance. All experiments were performed in a testing incubator (or recording rig) which is maintained at a temperature of 36.5 °C, with 5% CO_2 and humidity of 60%. Table 4.3 lists the cultures used in this study.

Table 4.3: Cultures plated per plating

Plating number	Culture names
1	A1, A2, A3
2	B1, B2, B3, B4, B2A
3	C1, C2, C3

4.2.4 Recording Apparatus

Figure 4.10 shows an overview of the data acquisition setup. Some of the components of this setup are described in details in the following subsections.

Figure 4.10: An overview of the recording setup used to record neuronal activity

Multichannel systems multielectrode arrays

The MEAs used for experiments in this thesis have 60 electrodes that include 59 active electrodes for stimulation and recording and one ground electrode (Table 4.4). Additionally, Neurorighter provides four auxiliary channels, to record external analog input, such as those provided using the magnetic driving circuit. An MCS array with four different quadrants is used for the ease of differentiating responses based on position of the electrodes (60-4QMEA1000iR-Ti-gr, MCS, GmbH). Figure 4.11a presents the typical MEA used for our experiments. Figure 4.11b displays an image of the electrodes; and a map of the MCS amplifier pins to the MEA electrodes is presented in appendix F. The critical measurements of this MEA are presented in table 4.5. The ring surrounding the electrodes (also called

Table 4.4: Electrode configuration

Electrode number	Configuration
1, 8, 57, 64	Auxiliary channels
33	Ground electrode
All others	Active recording electrodes

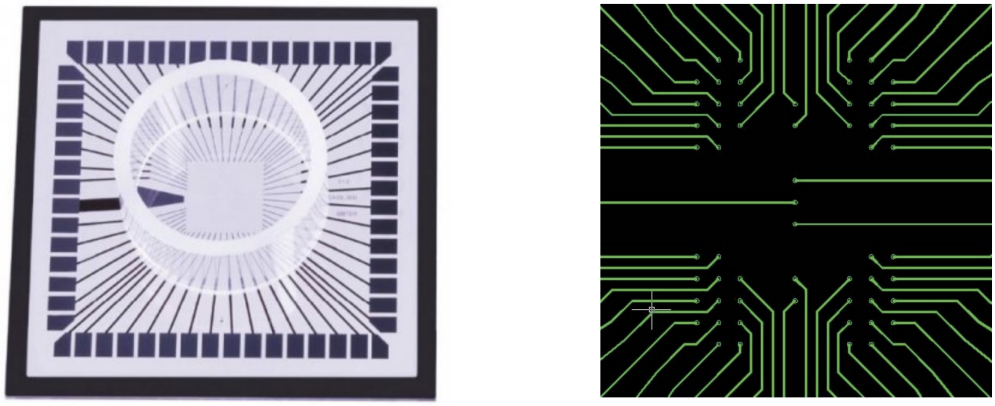

(a) An image of the MEA

(b) An image of the electrodes for the MEA

Figure 4.11: (a) An image of the MEA, and (b) its electrodes used for our experiments (courtesy: Multichannel Systems, MCS, GmbH)

the well), as seen in figure 4.11a, is used to keep the cultured cells in the region close to electrodes. For our preliminary experiments, this well was filled up with PBS solution, to imitate the condition when cells would be present on the electrodes. For the final set of experiments, dissociated cortical neurons are present on top of the electrodes and response to stimulus is recorded. The signals acquired from the electrodes are amplified by an MEA 1060 amplifier (Multi Channel Systems MCS GmbH) and can be acquired by a PC using a host of software. The software used in our work is Neurorighter, and it is discussed in details in the following subsections [89].

Table 4.5: Critical measurements for the multielectrode arrays

Parameter	Measurement in μm
Electrode diameter	40
Inter-electrode distance on each quadrant	200
Distance between two adjacent quadrants	1000
Distance between a quadrant and mid-line	500
Distance between central and peripheral mid-line electrodes	500

MCS MEA 1060 amplifier

Each of the 59 electrodes on the MEA record neuronal activity and stimulation artifacts[7]. These signals are then amplified using the MCS MEA 1060 amplifier (figure 4.12) and acquired by Neurorighter for data acquisition through a series of National Instruments' (Austin, TX) data acquisition cards. This amplifier should ideally provide at least 59 channels worth of useful data. However, over time, some of the channels in the amplifier become inherently noisy and start affecting the neighboring channels, as all these channels are moderately capacitively coupled. To maintain the fidelity of signals acquired, it is important to find these noisy channels and ground them to alleviate their effect on other channels. The objective of grounding certain channels is to reach a state where the overall noise level is sufficiently low and any recorded neuronal activity is not obscured. The most important step to eliminate overall noise and reduce the 60 Hz coupling is to connect the ground electrode on the MEA to any one of the ground pins on the MCS amplifier. The convention is to use the MEAs with their ground channel facing left as seen figure 4.11a.

4.2.5 Data acquisition

A large number of experiments are conducted on the plated MEAs and their respective raw data files are recorded. These experiments are broadly categorized into two different groups:

[7]Stimulation artifacts are the voltages recorded on each MEA electrode because of the stimulation pulse.

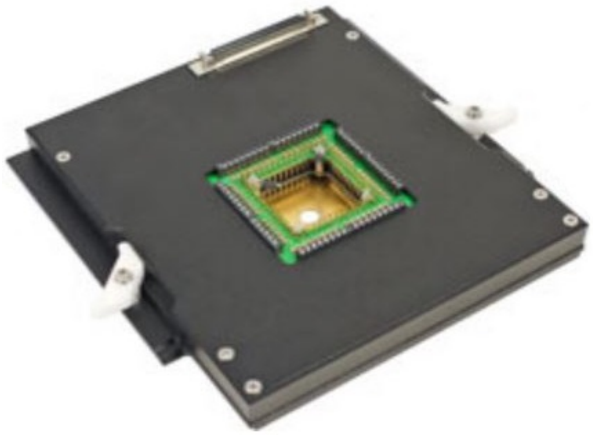

Figure 4.12: The MCS MEA 1060 amplifier

(a) experiments with neurons present on the MEAs, and (b) experiments with no neurons present on the MEAs. The neuronal response to stimulation and temperature change due to repetitive stimulation fall under the first category whereas studies regarding examination of stimulation artifact for different stimulation pulses falls under the second category. These experiments vary anywhere between ten seconds to ten minutes in duration, based on the nature of the data of interest. For example, an experiment performed to study the relative amplitude of stimulus artifacts across all electrodes requires a 10 seconds long recording of the stimulation artifacts. The magnetic stimulator is driven using a 100 mV, 1 kHz sine-wave for this experiment. Another experiment that required observing the change in neuronal activity in response to a 3.5 V, 5 kHz pulsed sine wave (2 cycles per pulse) with a repetition frequency of 2 Hz was ten minutes long. The in-built timer in Neurorighter is used to specify the duration of these experiments. Once recorded, the data is analyzed offline in MATLAB as described in the next section. Some of the important data sets recorded are listed below:

- The stimulation artifacts on an MEA without any cells, to characterize input pulses.
- Spontaneous activity of neurons before and after each stimulation experiment.
- Raw data files from Neurorighter for all experiments.
- Spike files from Neurorighter for all experiments.

- Voltage drop across the 1 Ω resistor using Neurorighter analog channels as an auxiliary file.

- Stimulation times for the MEA-electrode induced electrical stimulation.

Neurorighter System

Neurorighter is an open source software developed by researchers at California Institute of Technology and Georgia Institute of Technology that operates on a Windows system. It has a sampling rate of 25 kHz and employs neuronal spike detection through SALPA [93]. Neurorighter can also be used to provide stimulus to MEA electrodes, while generating a stimulation time file, and can be used to record analog signals using several available analog-input channels. In this thesis, these analog-input channels are used to record the input voltage waveform and the voltage across a 1-ohm resistor connected in series with the stimulation inductor. The analog-input channels saturate at $\sim$10.2 V, whereas, the MEA electrodes saturate $\sim$3.5 mV, so larger amplitude signals are clipped beyond these limits. Neurorighter also comes with a few digital output channels, which may be used as a waveform generator to provide biphasic pulses to an external device. For some control experiments, this capability is used to provide biphasic input to our magnetic stimulator. Further capabilities of this system may be explored through the Neurorighter Google sites.

The display screen of Neurorighter follows linear numbering so the MCS amplifier channels[8] need to be mapped on to the Neurorighter display channel. The advantage of this numbering shows up in data analysis where the row number from raw recordings correspond to the channel numbers on screen. The mapping of column-row notation on to linear mapping is fairly simple, for example, 11 corresponds to 1, 21 corresponds to 2, 22 corresponds to 10 and so on. This relationship may be easily represented using equation 4.1. For ease of reference, a map is created with both notations. We need this information to stabilize the amplifier through manual grounding of the excessively noisy channels as

[8]MCS amplifier channels follow a column-row notation.

explained in section 4.2.6.

$$L\_ch\_no. = C\_no. + (R\_no. - 1) * n \tag{4.1}$$

where

L_ch_no. is the linear channel number such as 1, 2, 3,and so on till 64

C_no. is the column number from the column-row notation (11, 21, ...,88)

R_no. is the row number from column-row notation

n is the number of columns in the array

4.2.6 Preliminary testing

Several mock tests were performed on MEAs without cells with the aim of understanding the test setup in the absence of any biological variables. As a first measure of whether the MEAs are capable of detecting induced fields, a hand-held permanent magnet was moved around the electrodes to induce eddy currents similar to an inductor with time-varying current flowing through it (Appendix A). Changes in voltage traces were observed, proving that the MEAs were capable of responding to the electric currents induced by a changing magnetic field (a moving magnet). The next step was to see if the stimulus artifact due to the current flowing through an inductor is observed, this would provide an idea about the sensitivity of the MEAs. This sensitivity of the MEAs was found to be close to 12.9 mV, meaning when a square pulse with amplitude of 3 mV and a duty cycle of 50 $\%$ is applied as an input to the amplifier, stimulation artifacts are observed; for voltages below this value, the changes are too small to be distinguished from default channel noise. These tests were considered important to establish the MEAs as a reliable recording device for detecting eddy currents produced by time-varying magnetic fields (an inductor carrying time-varying electric current).

Reducing noise levels

When the recording apparatus was first interfaced with the driving circuitry by inserting the stimulator into the MEA's PBS-filled well, it was observed that the MEA channels became two times as noisy as they were before the setup was interfaced, even when the driving circuit was switched off. This posed a problem because such high levels of noise would obscure the neuronal signals and grounding noisy channels was not an option, as this effect was observed on all the active channels. Through some trial-and-error based modifications to the circuit, we observed that this sudden change in noise levels was due to the driving circuit, and the MEA and MCS amplifier being at different grounds, resulting in a ground loop. To fix this problem it was ensured that the MCS amplifier and the driving circuitry shared a common ground. This is achieved by connecting the ground end of the stimulator to the ground of the amplifier.

4.2.7 Experimental protocol for in-vitro experiments

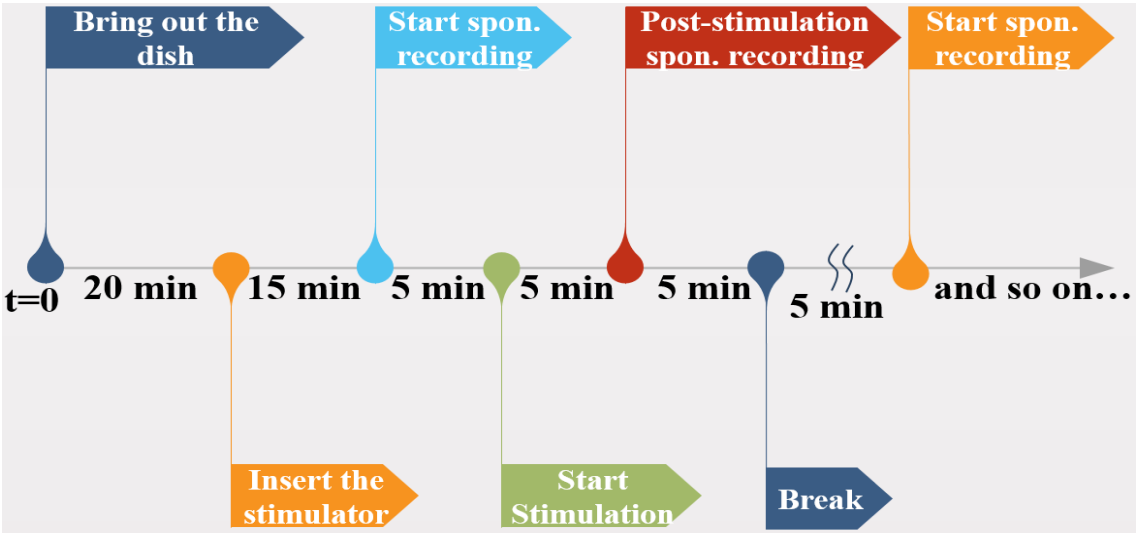

Figure 4.13: Time-line for performing the experiments.

Physical movement of a plated MEA can cause significant change in activity of the neurons. However, this activity is known to subside within the first five minutes of the

movement [49]. To avoid any effects of this movement on our recording, all the cultures were allowed to rest for at least 20 minutes before inserting the electrical or magnetic stimulator into them. Once the stimulator was inserted, another 15 minutes were allowed before recording the first set of spontaneous data. Typically the experiments were performed in three stages. First, the spontaneous data was recorded for five minutes, then stimulation was applied (sections 4.2.2 and 4.2.2), and finally post stimulation spontaneous activity was recorded. Around five minutes were allowed before testing the next set of stimuli. Figure 4.13 represents this time-line of performing experiments.

4.3 Data analysis

Neurorighter provides raw data in the form of a 64$\times$n matrix, where 64 corresponds to the total number of input data channels and n is the number of samples. However, as explained in section 4.2.6, not all channels contain useful information. So, the first step in data analysis is to reduce size of the raw data by eliminating noisy and grounded channels, for further analysis. This is done by calculating the standard deviation across all channels and then eliminating the channels with standard deviation below a threshold level. This threshold for elimination varies, depending on the type of data file. For example, the threshold for determining grounded channels is lower in spontaneous data than in data with stimulation artifacts. A typical value of this threshold across all cultures for spontaneous recording is 4 μV, while it varies between 50 μV - 500 μV for the other recordings. Any channels showing unusually high values of standard deviation are also removed as they correspond to extremely noisy channels, but this is a rare observation as the recording amplifier is stabilized through manual grounding of noisy channels before each experiment[9]. Figure 4.14 presents the standard deviation across one of the data sets for magnetic stimulation. It is important to store the indices of the channels that are not grounded for comparison against spontaneous activity. Once the useful channels are extracted, further analysis is performed on these

[9]This step is necessary only when extremely noisy channels are observed during an experiment.

channels.

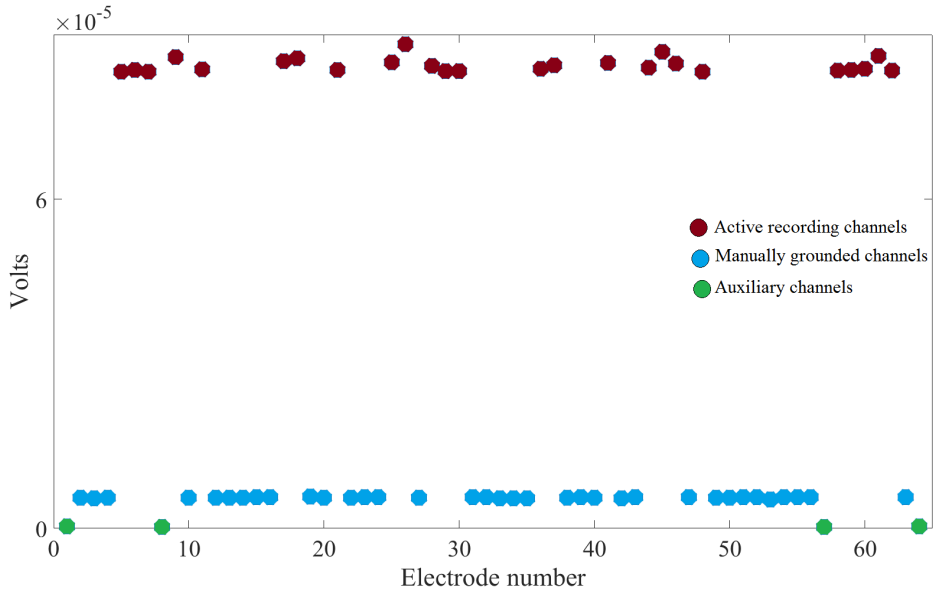

Figure 4.14: Standard deviation on all channels of a recorded raw data file with magnetic stimulation. The channels in blue are manually grounded, the channels in green are the auxiliary channels, and the channels in maroon are the active channels.

The channels filtered through the above step contain the response of neurons to stimulation. To analyze this response, the stimulation artifacts need to be removed from the raw recording. Once these artifacts are removed, neuronal spikes may then be detected for further analysis. A MATLAB code is written for both these purposes and the following subsections detail the process of stimulation artifact removal and spike detection for our experiments.

4.3.1 Stimulation artifact removal

It is important to remove the stimulation artifacts from the raw file to analyze the response to stimulation. However, there are several challenges in effectively removing the stimulation artifacts, some of these are:

- Blanking out just enough data to still be able to see stimulation evoked response. If a large amount of data around the stimulation pulse is blanked out, important

information may be lost.

- If the recording channels saturate in response to a stimulus pulse, then the stimulation artifact can become exaggerated, making it difficult to see a response. So experiments using external stimulators were performed using parameters to avoid this situation.

- Sometimes a stimulus pulse can induce a low frequency oscillation in the raw data which can result in erroneous spikes at the end of the artifact blanking period.

Keeping these constraints in mind, simple code was developed in MATLAB (Appendix E) to effectively remove stimulation artifact from the raw data and its algorithm works as follows:

- It uses an input threshold value to find peaks corresponding to stimulation pulses. These peaks are usually much higher in amplitude than spikes of neuronal origin.

- The duration of the stimulation pulse is used to determine how many samples to set to zero (0.5 ms before and after the pulse).

- The data points calculated in the previous step are set to zero to produce a cleaned waveform.

While this algorithm works very well for most data sets, it is inefficient in stimulation artifact removal in two cases: (a) when the induced stimulation artifact is very low amplitude and is in the range of amplitudes of neuronal spikes, and (b) when large low frequency oscillations are introduced due to stimulation. In both these cases, the spike detector ends up detecting erroneous spikes, hence the data sets corresponding to these cases are discarded from further analysis. Figure 4.15 shows a data set before and after the stimulation artifact removal.

Once the clean raw data file is received, traditionally the two most important set of data points to be extracted from these files are: (a) spike times and spike channels, and (b)

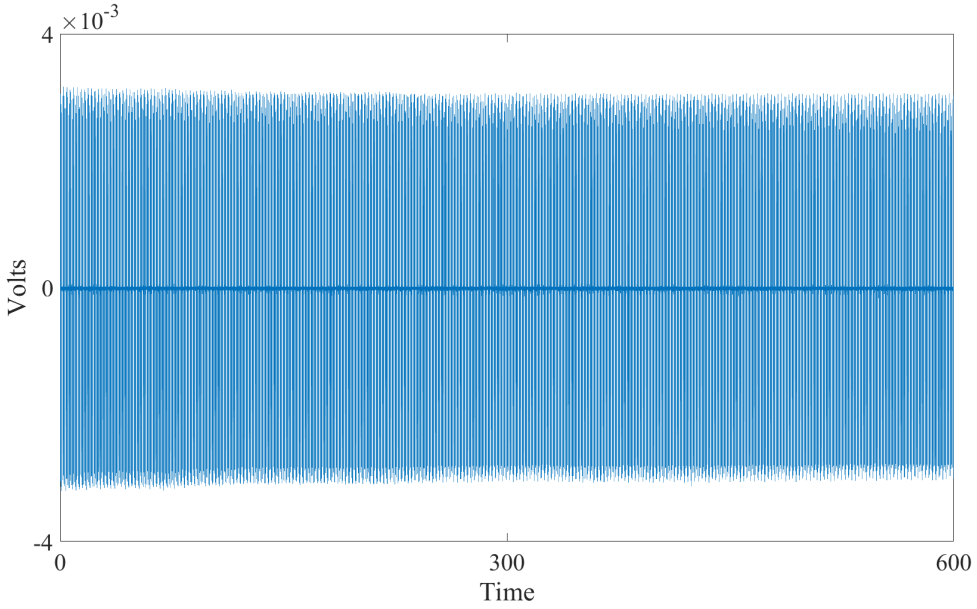

(a) Raw file with stimulation artifacts

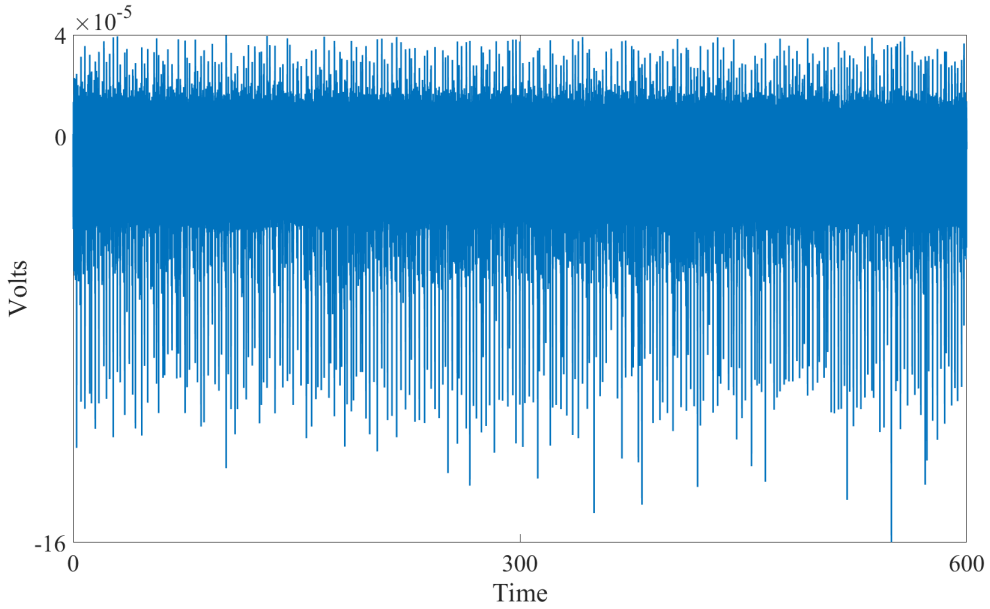

(b) The same raw file without stimulation artifacts

Figure 4.15: A code written in MATLAB is used to detect stimulation artifact spikes (a) and remove them from raw data (b) for further analysis. The change of amplitude can be seen on the y-axis, showing efficient artifact removal.

stimulation times and stimulation channels. In the case of external electric or magnetic stimulation, the concept of stimulation channels is irrelevant, but it is useful in MEA-electrode stimulation. While the stimulation times and channels are available through the '.stim' file produced by Neurorighter for MEA-electrode delivered electrical stimulation, custom programs were written in MATLAB to extract the stimulation times, and the spike times and spike channels for external electrical or magnetic stimulation, respectively.

4.3.2 Neuronal spike detection

A typical spike detector is one that identifies neuronal spikes based on the amplitude of this spike with respect to the average channel noise (*vrms*). The most common threshold value for such spike detection is five times the *vrms* of the channel [93]. However, it is observed that this threshold value, similar to the default spike detector (SALPA) in Neurorighter, often registers stimulation artifacts and amplifier induced noise into the recorded spike data, making manual sorting of spikes necessary. While, open-source software such as SqueakySpk [94] provide the capability of such spike sorting, it can become a cumbersome task for long experiments with tens of thousands of spikes. Hence, we looked for alternatives and found that a spike detection code[10] with a high threshold value of seven times the *vrms* of the channel, efficiently records only the neuronal activity, eliminating the need for manual spike sorting. The efficiency of our spike detector is verified through testing on data recorded from an MEA with no cells and no external stimulus applied. The only content of this data set is the amplifier induced noise, and our algorithm effectively detected zero spikes in this data. Figure 4.16 displays a spike detected by our spike detector at a threshold of 7 times *vrms*.

While this spike detector robustly identifies neuronal spikes, the recorded spike waveform are verified to ensure they are indeed neuronal in origin. To determine whether a detected spike is good (neuronal in origin) or not, two different set of experiments are performed and

[10]The spike detection code was originally written in MATLAB by our collaborator Riley Zeller-Townson at Butera Lab, Georgia Institute of Technology.

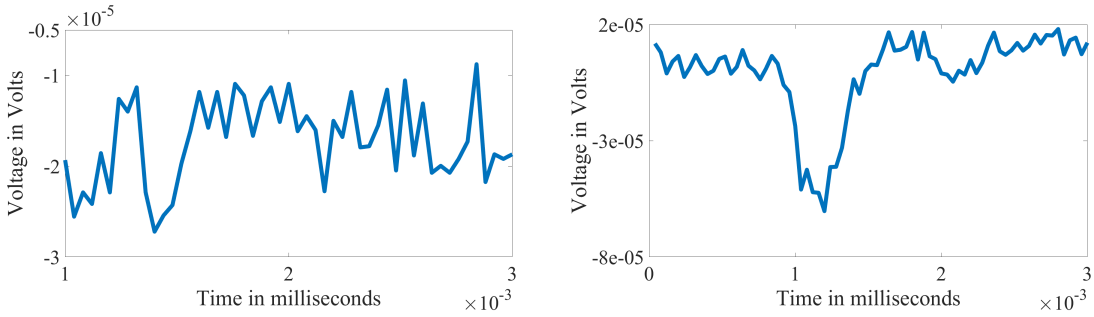

(a) Amplifier glitch (b) Neuronal spike

Figure 4.16: (a) An erroneous spike detected by the spike detector at threshold of 5 times vrms, and (b) a neuronal spike detected by the spike detector at threshold of 7 times vrms.

the recorded files examined. These two data sets comprise of the following:

- Recording from an MEA with no cells on it (only PBS solution) and without any stimulation pulses. This records the default spikes introduced by the driving circuitry.
- Recording of spontaneous activity from the plated cultures. This provides an idea of the nature of neuronal activity and what the 'good' spikes should look like.

Based on looking at several of these files, a robust spike selection criteria is designed, which is applied to spike selection during external electrical and magnetic stimulation. Two main features of this criteria are:

- All peaks that have amplitude lower than 40 μV are rejected. This criteria is selected because the recording amplifier is capable of inducing spikes as high as 35 μV when no cells are present on the MEA being tested. So, selecting a 40 μV threshold, effectively removes such spikes from being detected.
- If the peak power is evenly distributed between the positive and negative parts of a peak, it is considered noise, as neuronal peaks have a larger negative peak in the middle with smaller positive peaks on either sides. Bursts are an exception to this criteria.

If the detected spikes don't meet the above criteria, they are discarded from further analysis. If a burst of neuronal activity is observed in a culture, in order to ensure its neuronal origin, data across all electrodes are analyzed and we look for the following characteristics of neuronal activity:

- Direct and indirect responses occur reliably within 10 - 200 ms of the stimulation pulse.
- The responses are seldom observed across all channels at the same time.
- Stimulation evoked-response amplitudes and shapes is likely to vary from channel-to-channel as they are from different neurons.

Once, cleaned raw files with neuronal activity are obtained through data analysis, as discussed above, a set of statistical metrics are calculated to characterize the response to different stimuli. While traditionally response to stimulus is represented in terms of number of spikes recorded after application of stimulation pulse, there's no way of determining whether the spike detected is in response to stimulation or occurring spontaneously. In general, synaptic blockers are used to eliminate culture wide bursts, but spontaneous spiking still continues in individual neurons. In our case, we observed that the spontaneous spiking went down significantly upon addition of synaptic blockers. So, we decided to perform the experiments without adding these blockers to the culture. Figure 4.17 illustrates the peri-stimulus histogram of the cleaned data shown in figure 4.15b. While there's an apparent increase in spiking, post-stimulus, this data is not easy to interpret. So, we adopted an alternative approach to analyzing this data, where statistical significance of change in firing rate is calculated before and during stimulation.

4.3.3 Calculating the firing rate per channel

As we lean towards a more statistical approach to determine the effect of stimulation on dissociated cortical neurons, the quantity of prime importance is the firing rate per channel.

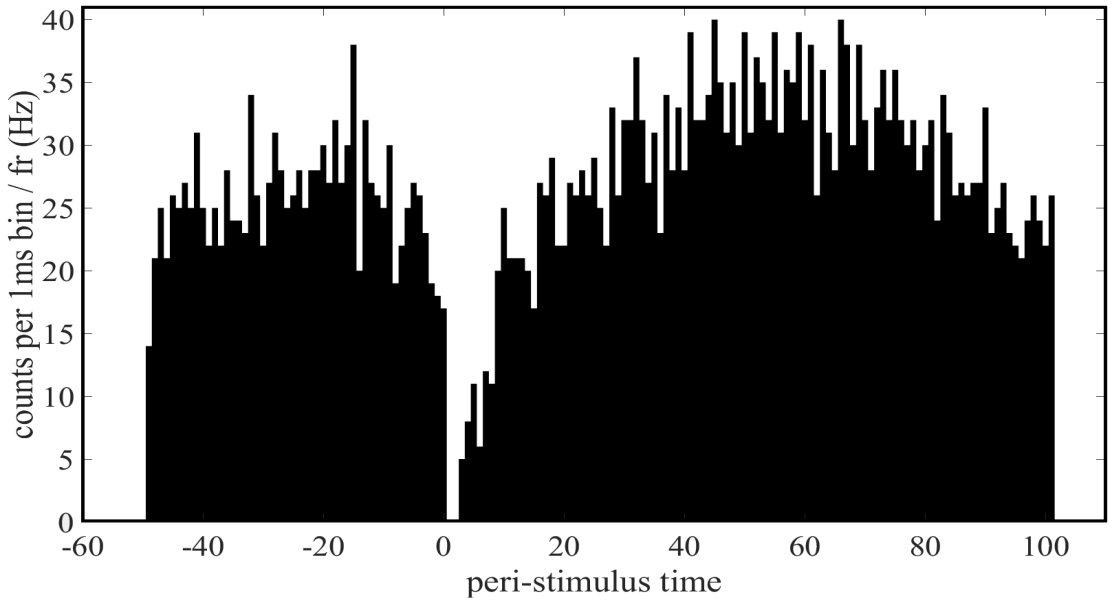

Figure 4.17: Peri-stimulus histogram for magnetic stimulation (4 V, 5 kHz two cycles of sine wave) presented at 2 Hz to Dish B4.

As the name suggests, it is the number of spikes produced per second per channel. It is important to divide the total number of spikes by the total number of channels because this number varies from one experiment to the other. In some cases, even between the spontaneous recording before stimulation and the recording during stimulation. For the spiking rate for spontaneous data, it is a simple division of the total number of spikes by the duration of the experiment in seconds. However, for the peri-stimulus data, the blanking periods introduced due to stimulation artifact removal render the adjustment of firing rate necessary. For example, if a period of 1.6 ms is blanked around each stimulus pulse, over a period of five minutes, a total of 0.96 s of data is blanked out, so instead of diving the total number of spikes by 300, we divide it by 299.04, thereby accounting for the effect of the blanking period on firing rate. The results obtained from the experiments described in this chapter are analyzed and presented in the following chapter.

4.4 Observations

Some of the important observations from this chapter are:

◦ To avoid creation of a ground loop, all distinct circuit elements should share a common ground.

◦ Noisy channels on the recording amplifier must be manually grounded to avoid erroneous spikes in the recorded data.

◦ For calculation of firing rate of the stimulation data, the number of samples set to zero during cleaning of raw data must be accounted for.

CHAPTER 5
EVALUATION OF MICRO-SCALE MAGNETIC STIMULATION: RESULTS AND FINDINGS

5.1 Motivation

Micro-scale magnetic stimulation is a relatively new field of research where the results of in-vivo and in-vitro studies reported so far vary from one study to the other or even within the same study. For example, the studies performed by Lee and Fried highlight the difference in responses produced by the same stimulation pulse on different neurons[1] [67]. They show that a single pulse of 500 Hz sinusoidal waveform could not produce any response, even at amplitudes as high as 40 V, at low repetition rates. A repetitive stimulation[2], on the other hand, was successful in activating the pyramidal neurons and produced different responses in the different types of cells examined. For example, in Type II PFC cells, spiking was observed after a 30 s period of applying continuous stimulation, which then continued during stimulation, and stopped when stimulation was stopped. However, in Type I PFC neurons, spiking started more than 45 s after application of stimulus and continued even after the stimulation was turned off.

These studies also report different power levels required for stimulation of neurons (10 mW - 2 W). In general, the power levels reported for electrical stimulation are much lower than the power levels reported for magnetic stimulation. But, there aren't many studies that provide a one-on-one comparison between the two. Thus we performed a parametric study to examine a range of factors such as power consumption, heating, as well as the respective response of neurons to electrical and magnetic stimulation.

Two sets of experiments are performed to evaluate micro-scale magnetic stimulation and

[1] Type 1 and Type 2 PFC, and Type 1 and Type 2 M1 pyramidal neurons were studied.
[2] Delivered at 10 Hz for a duration of 4 s.

compare it to electrical stimulation. The first set of experiments are performed on MEAs without any neurons. In these experiments, the MEA well is filled with a PBS solution and the stimulation artifacts are recorded and analyzed for a set of parametric studies. The goal of performing these experiments is to gauge how the experimental values compare to the theoretical predictions. Once the setup is confirmed to behave as expected, a second set of experiments are performed where the response of dissociated cortical neurons to micro-scale magnetic stimulation is analyzed. The neuronal activity is recorded using MEAs, acquired using Neurorighter, and analyzed using MATLAB (Natick, MA). The following sections present and discuss these results in detail.

Some of the important observations of the work presented in this chapter are:

- Magnetic stimulation induces change in firing rate of neurons, but a specific trend in this change is not observed.
- Factors other than magnetic stimulation that may induce a change in firing rate are analyzed, and it is concluded that the magnetic induction continues to be the dominating force in the experimental setup employed.
- No considerable change in temperature is observed for magnetic or electrical stimulation at repetition rates of 2 Hz, consistent with the findings in the previous chapter.
- The induced potential varies as a function of 1/r as the distance between the recording electrodes and the stimulator is increased.
- Finally, the simulation results presented in the previous chapter are refined based on the stimulation parameters used during experiments and thresholds for neural stimulation using magnetic stimulators are predicted.

5.2 Experiments without neurons

As micro-scale magnetic stimulation has never been used for experiments in conjunction with a multielectrode array before, we perform a set of parametric studies to characterize the stimulation artifacts observed from magnetic stimulation. The recorded values are compared with the expected theoretical values, or with COMSOL predictions. The following subsections discuss these experiments and their results.

5.2.1 Induced stimulation artifact amplitude decreases with increase in distance between the stimulator and the recording electrodes

Induced potentials change as an inverse function of r, which is the distance between the source and the point of measurement [95]. For MEA-electrode delivered electrical stimulation this means that the electrodes farthest from the stimulating electrode will record the smallest stimulation artifact. However, for external magnetic stimulation, similar amplitude of potentials are induced in more than one electrode, because each MEA electrode measures 30 μm, and the external magnetic stimulator measures 1 mm by 0.5 mm. So, we vary the distance between the recording electrodes and the stimulator, in steps of 500 μm, to study the 1/r effect. A 1 kHz, 100 mV signal is provided as input to the amplifier and the induced stimulation artifacts are recorded. The changes in recorded potentials are plotted in figure 5.1a. The error bars show the highest and the lowest induced potentials, suggesting that not all electrodes see the same induced potential, as expected. This experiment is then modeled in COMSOL, where the stimulation pulse, the inductor geometry, and the media surrounding this inductor, are modeled to be the same as the physical experiment, and the induced potentials are also calculated at similar distances. This plot is shown in figure 5.1b. We thus verify that the induced potentials are in agreement with the theory, and the difference between the two plots may be attributed to the non-linearity in the stimulation and recording circuits.

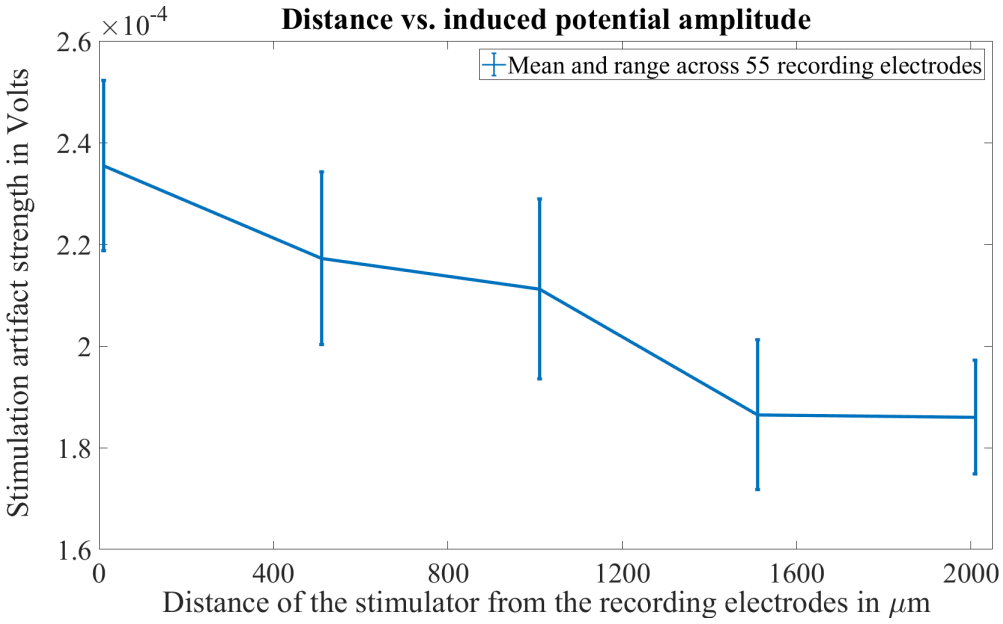

(a) Experimental results

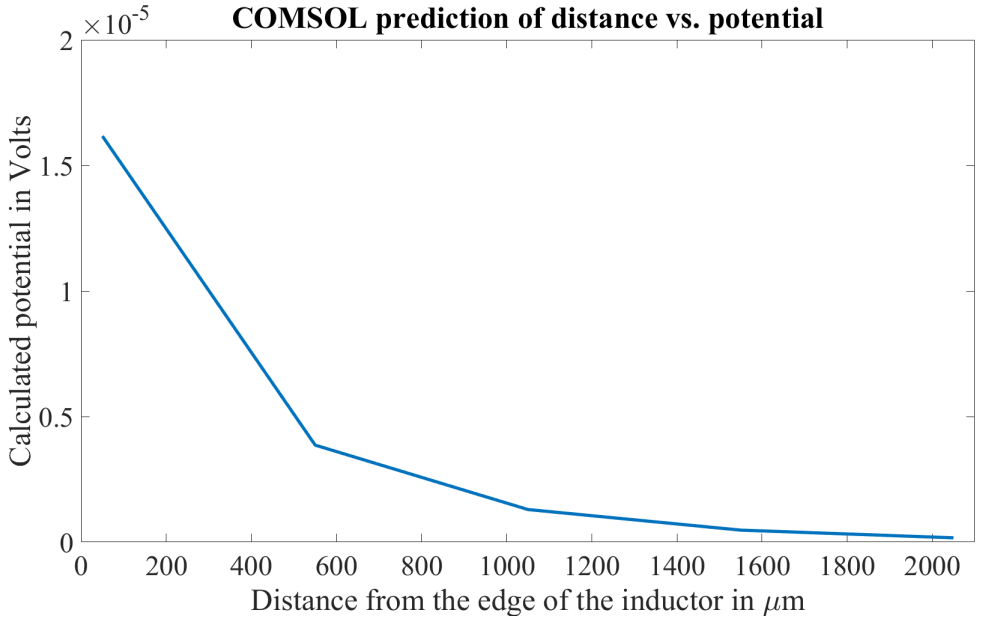

(b) COMSOL prediction

Figure 5.1: Experimental measurement of distance vs. induced potentials and COMSOL prediction of the same. (a) For the experimental values, the induced potential is averaged over all the recording electrodes (n=55) and the mean is plotted. The bars indicate the range of values. (b) For the COMSOL simulation, a line is defined at the point where measurement is needed and the induced potential is integrated over this line.

5.2.2 Characterization of the stimulation artifacts

It is standard for micro-scale magnetic stimulation studies to perform control experiments to ensure that the neuronal stimulation is induced inductively, not capacitively. We adopt a simulation assisted approach to address this concern, where we use COMSOL to model the stimulation pulse used in physical experiments and simulate the stimulation artifacts. We also simulate a capacitively generated stimulation artifact. We then compare the experimentally recorded stimulation artifacts to the COMSOL predictions. The input pulse modeled and tested experimentally is a single cycle of a sine wave with a frequency of 2.5 kHz, an amplitude of 3.5 V, and with two different phases, 0 degrees and 180 degrees. The results are illustrated by figures 5.2 - 5.4. We observe that the recorded stimulation artifacts closely follow the COMSOL predictions for inductively induced artifacts.

5.2.3 Coupling between the magnetic stimulator and the recording electrodes increases in presence of PBS solution

Micro-scale magnetic stimulation induces neuronal activation at much lower power levels than external magnetic stimulators, such as trans-cranial magnetic stimulators. The reason for this lower power consumption is two-fold: (a) the magnetic field generator is much closer to the target neurons, and (b) the air-tissue interface is eliminated. In this experiment, we analyze the change in coupling due to elimination of the air-media interface. For this, the stimulator is placed above an MEA while very little PBS is present in the MEA well, such that there is air between the stimulator and the PBS solution. Then PBS solution is added drop-by-drop using a plastic pipette tip, till it submerges the stimulator tip completely. Distance between the recording electrodes and magnetic stimulator is kept constant here. Figure 5.5 shows the recorded changes in coupling where the coupling strength increases 30 times. This increase in amplitude corresponds to a 900 times increase in the power delivered, which is in agreement with the general understanding that micro-scale magnetic stimulators have a lower power consumption.

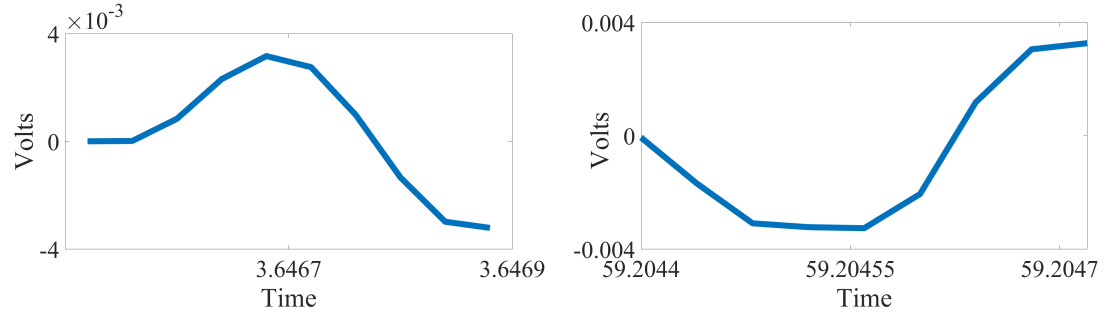

(a) Input sine phase is 0 (b) Input sine phase is 180

Figure 5.2: Recorded stimulation artifact from MEAs

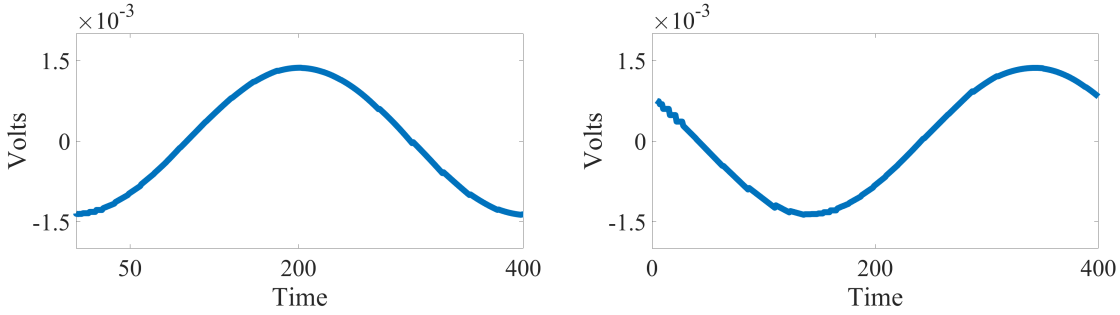

(a) Input sine phase is 0 (b) Input sine phase is 180

Figure 5.3: COMSOL predicted stimulation artifact for magnetic stimulation

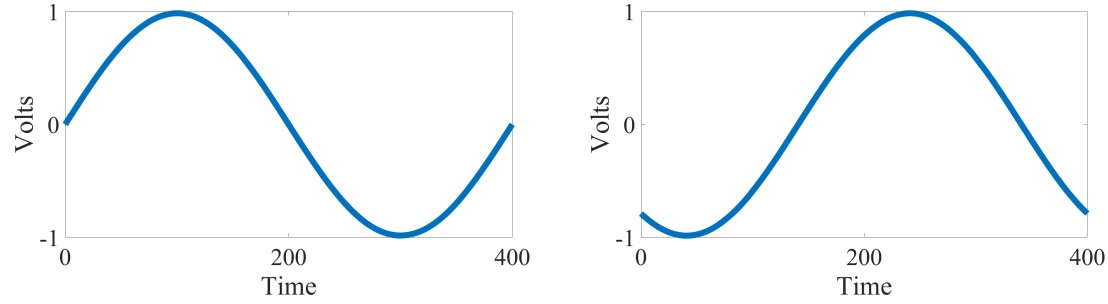

(a) Input sine phase is 0 (b) Input sine phase is 180

Figure 5.4: COMSOL predicted stimulation artifact for electrical stimulation

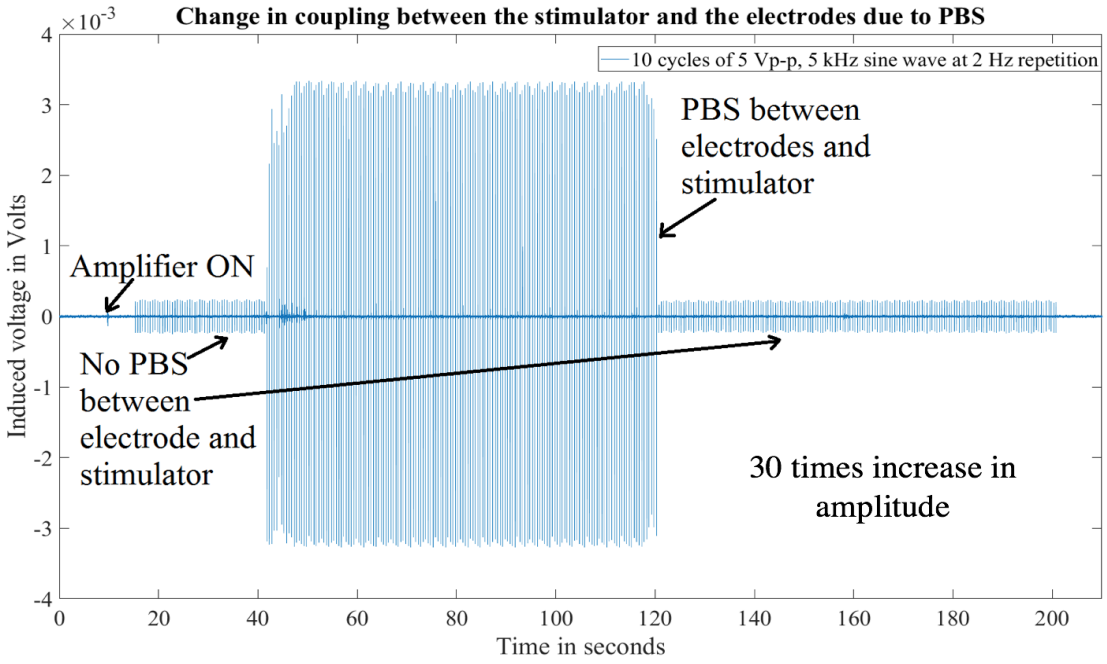

Figure 5.5: Change in coupling between the magnetic stimulator and the recording electrodes due to the addition of PBS between them.

We thus show that a multielectrode array is capable of characterizing micro-scale magnetic stimulation. Moreover, these arrays have been used to stimulate and study neurons before, so we know they are capable of recording neuronal activity. So, as a next step, we replace the PBS filled MEAs (used in the above experiments) with plated MEAs and study the effects of micro-scale magnetic stimulation on neurons. The following section details the experiments performed and the results thus obtained.

5.3 Experiments with neurons

For the results reported in this section, experiments are performed on plated MEAs, where micro-scale magnetic stimulator is inserted into the MEA well and stimulation is delivered using parameters listed in table 4.2. The recorded raw files are analyzed using MATLAB, and the important findings are presented.

5.3.1 Magnetic stimulation of dissociated cortical neurons results in change in firing rate

Firing rate[3] of neurons during spontaneous activity before stimulation is compared with the firing rate of neurons during stimulation, and a test for statistical significance is performed. For each experiment reported here, 600 stimulus pulses are delivered over a period of 5 minutes and the response to stimuli is recorded. This response is averaged over the number of channels it is recorded from, and the duration of the experiment, to estimate the firing rate per channel. This helps normalize the data across experiments performed on different dishes on different days. Table 5.1 reports the parameters tested and the results for statistical significance.

The null hypothesis tested here is: *There is no significant difference between the firing rate per channel between the two data sets tested*. A 5% significance level is tested. An h-value of zero means the hypothesis cannot be rejected, whereas an h-value of one indicates rejection of null hypothesis. The Wilcoxon signed rank test is used to obtain the h-values, where the data sets compared contain total number of spikes recorded per second per channel before and during magnetic stimulation.

Table 5.1: The signed rank test on 'before' and 'during' stimulation firing rate of cultures

Dish	Voltage [V]	Frequency [kHz]	Number of cycles	h-value
B4	3	10	4	1
B2A	3.5	2.5	1	0
B1	4	5	2	0
C1	3.5	2.5	1	1
C2	0.5	2.5	1	1
C3	0.25	2.5	1	1

[3]Total number of spikes recorded divided by the duration of the experiment in seconds.

Statistically significant difference in activity is observed in response to stimulus

Four out of the six cultures that were tested show a statistically significant change in firing rate in response to stimulus. To confirm that this change is because of stimulation and not a spontaneous change in behavior of neurons, ten minutes of spontaneous activity is recorded from three different cultures and the acquired data is divided into two five-minute long data sets. The same statistical significance test is performed on these data sets (see table 5.2). The rejection of null hypothesis in all these recordings suggests that, there is no significant change in spontaneous activity during a short span of ten minutes, if no stimulus is applied. We performed these tests on firing rates for electrical stimulation of neurons as well, to determine the threshold for neuronal activation and found that neurons responded robustly to ± 500 μA pulses. We use this value for all later analyses.

Table 5.2: The signed rank test on continuous recording of spontaneous data

Dish	h-value
B4	0
B2A	0
B1	0

Next, the firing rate for the four cultures that showed an h-value of one are compared to observe any trends in stimulation as shown in figure 5.6, and no specific pattern is observed. We also examine the firing rate of cultures that failed the test for statistical significance (figure 5.7) and notice that the firing rate for both these cultures is much higher compared to the other cultures. This implies that the effect of stimulation may have been obscured by the high spontaneous firing rate. We then analyze the factors that may have caused this change in firing rate, instead of the applied magnetic stimulation. Some of these factors are temperature changes, physical movement of the dish or movement inside the dish, gradual reduction in activity over time because of changing physical conditions inside the incubator, and capacitive currents between the stimulator and the electrodes.

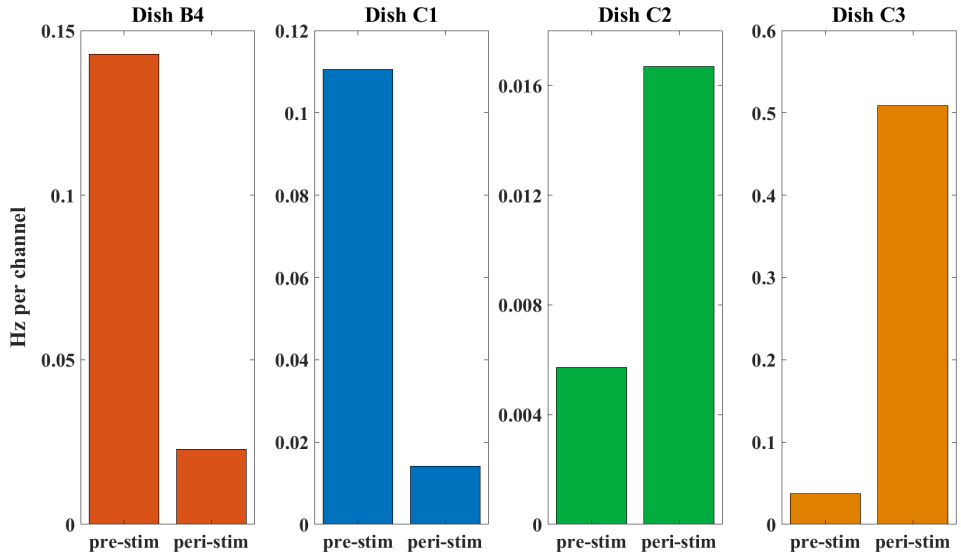

Figure 5.6: Firing rate before and during stimulation for dishes B4, C1, C2, and C3 are plotted.

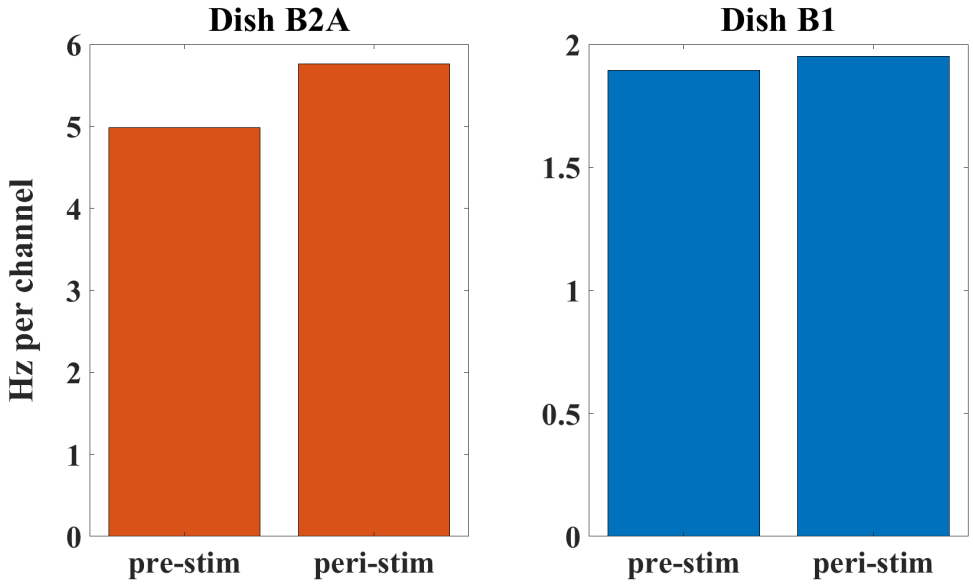

Figure 5.7: Firing rate before and during stimulation for dishes B1 and B2A are plotted.

5.3.2 Analysis of factors that may cause a change in firing rate

We calculated the temperature changes on a plated MEA (see section 5.3.5), in response to magnetic stimulation at one of the higher voltages tested, 3.5 V, over a period of five minutes, and recorded a net change of 0.23°C in temperature. This rise in temperature is not sufficient to significantly alter the firing rate, as one degree rise in temperature is reported to produce about 2.8 $\%$ change in firing rate [85], whereas our test looks for a difference of at least 5 $\%$ change in firing rate. While physical movement can cause significant change in activity, our experimental protocol (section 4.2.7) ensures that this effect has subsided before the experiments are performed. The movement of the inductor alone is restricted as it is glued to the plastic pipette tip (see section 4.2.1), so the possibility of this causing a change in firing rate is also eliminated.

The magnetic stimulator inserted in the media essentially acts like a capacitor, where the inductor and the media are its plates, and the Parylene-C coating is the dielectric. A control experiment is performed to compare the effects of these capacitive currents versus the effects of inductive currents in our experiments. For this, stimulation is applied through an insulated but busted inductor and compared to the stimulation applied through a conducting inductor. The two inductors have the same inductance value, and the same stimulus is applied to both of them. We hope to capture only the capacitive effects of the inductor by testing the busted inductor. Figure 5.8 shows the results of this experiment, where it is noted that the inductively induced stimulation artifacts are $\sim$20 times larger than the capacitively induced artifacts. This implies that inductive effects of the inductor are much stronger than its capacitive effects.

We performed another experiment to observe the effects of poor insulation on stimulation artifacts, where an uninsulated inductor was inserted into the media for testing. We noticed that an uninsulated inductor introduced a lot of noise into the whole MEA-setup and obscured neuronal recording. So, we conclude that proper insulation was important for recording neuronal activity in this setup. Based on the above analysis we can say that whatever changes

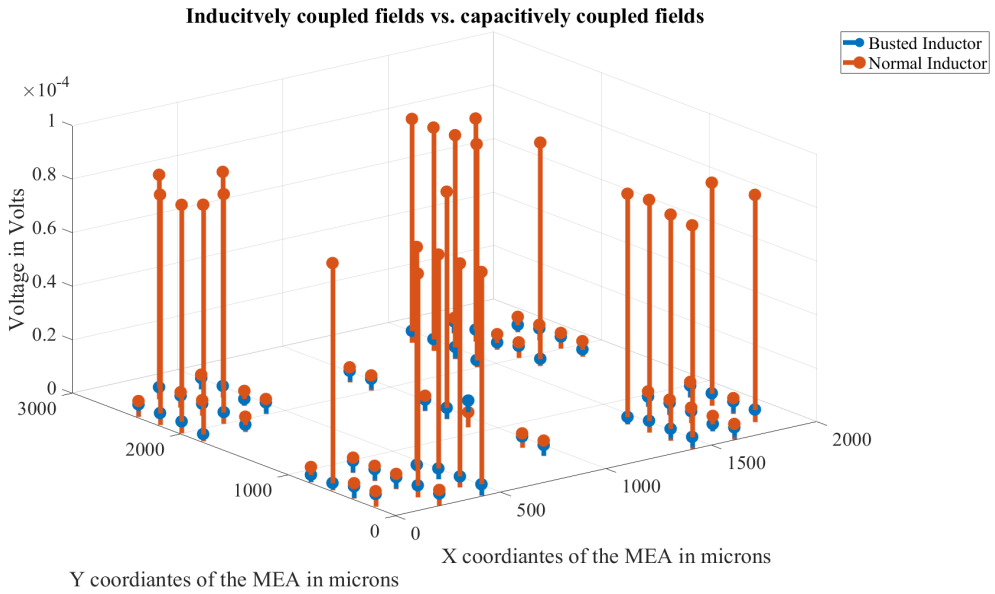

Figure 5.8: Comparison of the average induced potential strength between a busted inductor (representing capacitive effects of the inductor) and a working inductor. It is seen that the potential induced by a working inductor is almost 20 times larger than the potential induced by a busted inductor.

were observed during experiments were in fact due to the magnetic stimulus applied.

5.3.3 Cultures lose spontaneous activity over time

As the experiments described in this chapter are performed without a Teflon cap covering the MEA well, the moisture content of the MEA dish changes over time. This happens despite the test incubator being maintained at a level of 60 % humidity[4]. This change in physical property of the media has an effect on the overall responsiveness of the culture, which is captured in figure 5.9. This figure plots the spontaneous activity of a culture over a course of four hours, while experiments were being performed on it. This figure suggests that all experiments performed after 1300 hours on this day do not contain any useful data.

[4]Maintaining higher levels of humidity can damage the electronics inside the incubator.

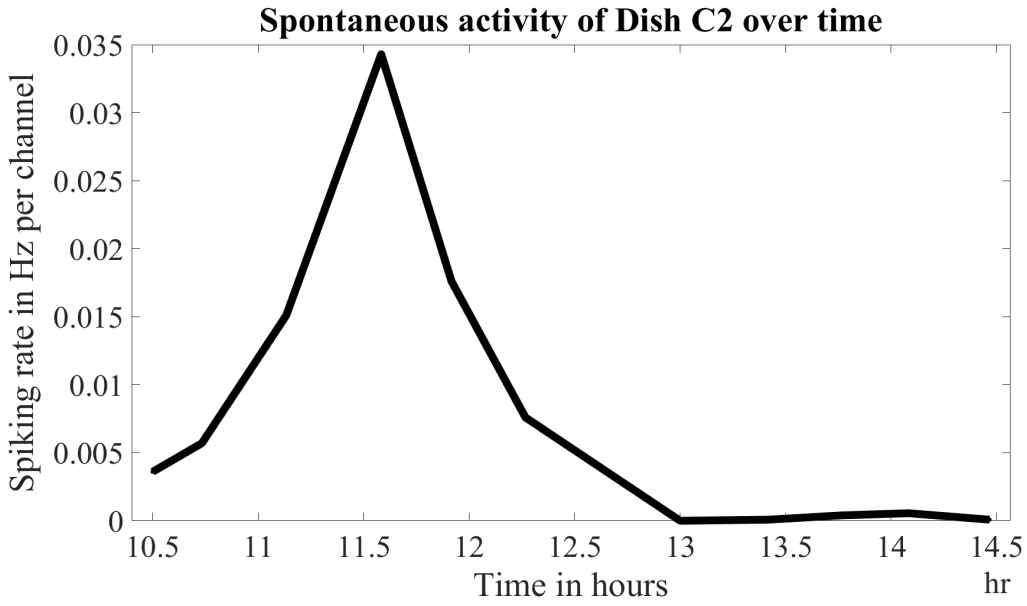

Figure 5.9: Firing rate for dish C2 over a period of four hours. While these are the spontaneous firing rates, stimulation was applied to this culture every 15 to 20 minutes. The decrease in spontaneous activity over time is evident.

5.3.4 Power comparison: magnetic vs. electrical

We next calculate the power consumed by electrical and magnetic stimulation, based on the parameters that were used to study the neuronal responses described above. For magnetic stimulation pulses delivered at 2 Hz in the form of a 2.5 kHz single cycle of sine wave, the average power consumption is:

- 60.4 mW at an amplitude of 3.5 V to the amplifier, and
- 370 μW at an amplitude of 250 mV to the amplifier.

The effect of amplifier's amplification is included in these calculations. For electrical stimulation pulses delivered at 2 Hz in the form of a biphasic current waveform with peak amplitude of $\pm$500 μA, the average power consumption is 40 μW. Here the electrode impedance is considered to be 0.2 MΩ, which is at the higher end of the spectrum [82].

The COMSOL calculation for average power for a 250 mV input, at 2 Hz is 3.17 mW, which is almost an order of magnitude higher than the experimentally calculated value (370

μW). This is because the modeled inductor has a resistance that is an order of magnitude smaller than the resistance of the inductor tested experimentally. Modeling the inductor in 2-D leads to such discrepancies. However, being cognizant of such differences helps improve modeling.

5.3.5 Minimal temperature change in media is observed at a 2 Hz repetition rate of stimulus

Traceable Excursion-Trac USB Datalogging Refrigerator/ Freezer thermometer (Cole Parmer, Vernon Hills, IL) is used to record temperature changes during five minute long experiments, where the stimulus is applied at the maximum values tested, that is, $\pm$500 μA for electrical stimulation and 3.5 V for magnetic stimulation. Figure 5.10 captures the experimental setup and figure 5.11 illustrates the temperature changes.

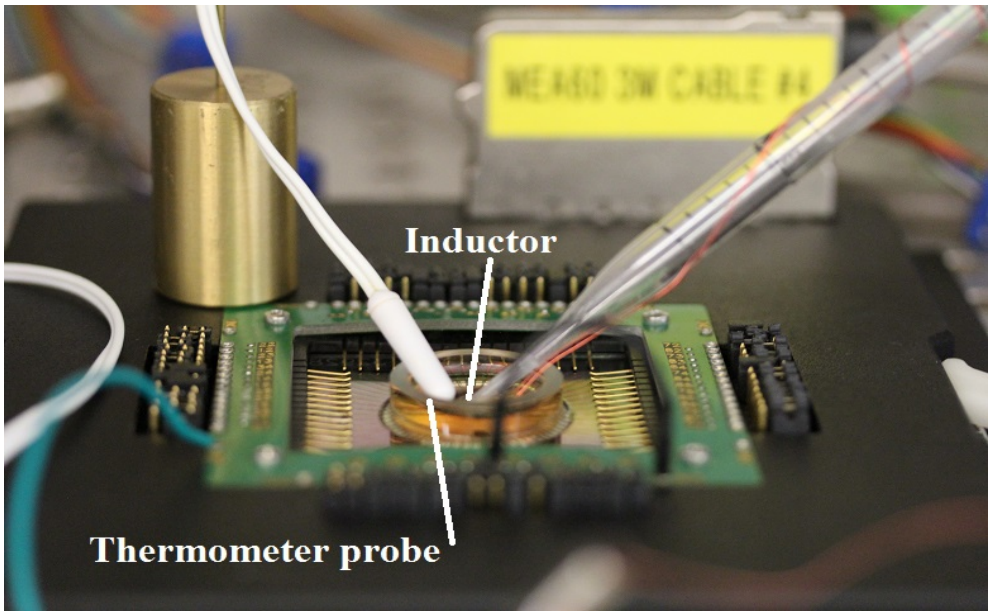

Figure 5.10: An image showing the temperature recording apparatus. The thermometer is inserted in the MEA well containing cells and the stimulus is delivered through the magnetic stimulator. Similar setup is used for measuring temperature changes for electrical stimulation as well.

A general increase in temperature is observed as the media, and the thermometer along with it, is adjusting to the incubator temperature. So, the changes in temperature recorded

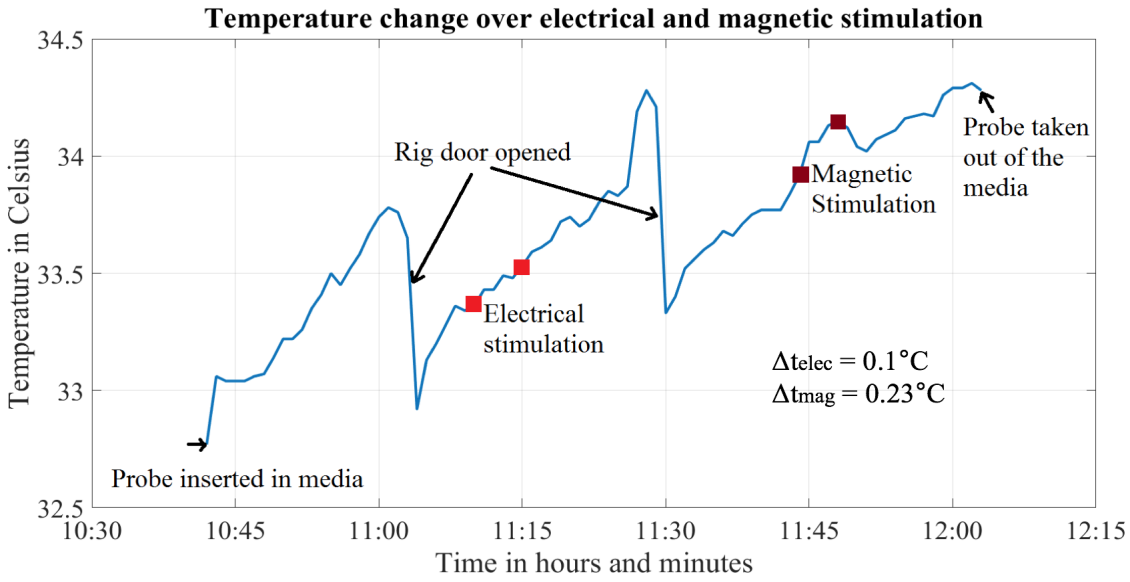

Figure 5.11: Temperature change due to electrical and magnetic stimulation during a five minute long experiment where the stimulus is applied at the maximum values tested, that is, ± 500 μA for electrical stimulation and 3.5 V for magnetic stimulation.

(0.1°C for electrical and 0.23°C for magnetic) include the default temperature change that the media is undergoing already, implying that the actual change in temperature is even lower.

5.4 Revisiting simulations

An interesting application of using COMSOL in conjunction with these experiments is that we can use the stimulation parameters tested and predict the amplitude of induced electric fields and the activating function values at different distances. The activating function quantifies the effect of extra-cellular stimulation on neurons, as discussed in chapter 3. These induced values are calculated at the distances of $\sim$10 μm, corresponding to the thickness of insulation, and $\sim$50 μm, corresponding to roughness introduced due to super glue, and presented in table 5.3. These results are in agreement with the results reported by Lee et. al where mild response to stimulus is observed in an in-vivo study at voltages as low as 11.2 mV [67]. We must note that the actual induced field values can be up to an

order of magnitude lower, given the discrepancy between the resistance of the simulated and the actual inductors. These calculations are valuable for further simulation studies for the analysis of pulse shapes and coil designs.

Table 5.3: Predicted induced electric field and induced activating function (f) values

Voltage [V]	Frequency [kHz]	Distance [μm]	Induced e-field [V/m]	Induced f value [V/m^2]
3.5	2.5	10	1.6	4250
3.5	2.5	50	1.3	2880
0.25	2.5	10	0.12	304
0.25	2.5	50	0.09	206

5.5 Observations

OBSERVATION 1: There is a statistically significant change in the firing rate of neurons before and during stimulation, but no specific change in the rate, in terms of its increase or decrease, is observed.

OBSERVATION 2: The overall spontaneous activity of neurons decreases over time, allowing only a two-hour window to perform experiments at a time. The data obtained beyond this 2-hour mark is not very informative, as the neurons become highly unresponsive.

OBSERVATION 3: Factors that may cause a change in firing rate are analyzed and we conclude that the change observed during experiments is most likely caused by magnetic stimulation.

OBSERVATION 4: On an average, power consumption for magnetic stimulation (60.4 mW for 3.5 V, and 310 μW for 250 mV) is higher than that for electrical stimulation (40 μW at $\pm$500 μA stimulation amplitude).

OBSERVATION 5: At a stimulation rate of 2 Hz, magnetic stimulation leads to a temperature change of 0.23°C when 3.5 V is the input to the amplifier. Electrical stimulation on the other hand leads to a temperature change of 0.1°C at $\pm$500 μA stimulation amplitude.

OBSERVATION 6: The experimentally measured distance vs. potential plot roughly follows the 1/r behavior. The prediction of distance vs. potential using COMSOL is closer to the ideal behavior. This discrepancy in behavior may be attributed to the non-linearity in the stimulation and recording circuits, where mild fluctuations in supplied voltage can result in the observed step-like response.

OBSERVATION 7: Submerging the stimulator in PBS solution increases the coupling between the stimulator and the recording electrodes by more than 30 times.

5.6 Discussion

In chapter 3 we proposed that magnetic stimulation may be a better option for cochlear implants, than electrical stimulation. In this chapter, we performed a set of experiments to validate the results presented in that chapter. We could not validate the spatial resolution of magnetic stimulation vs. that of electrical stimulation because the size of inductors used in the above experiments is larger than the size of one quadrant of the MEA. So, spatial probing of neurons was not possible. Moreover, amplifier instability required grounding of channels, which, at times, made an entire quadrant unavailable for testing, further reducing the sample size. We will need inductors that are smaller in size, and more stable amplifiers, to verify this finding. However, we did verify heating, power consumption, effect of variation of distance, and shape of stimulation artifact, suggesting that the predictions of COMSOL are reasonable.

For data analysis, traditionally the response to stimulus is represented in the form of number of spikes generated in the 50 - 200 ms duration after a stimulation pulse is applied. The work presented in this chapter adopts an alternative approach because of the following reasons. Firstly, synaptic blockers[5] were noticed to significantly reduce spontaneous activity in the cultures, so they were not used for the experiments discussed above. As a result, there were spontaneous bursts in the cultures, implying that the spikes showing up in

[5] 100 μm APV (amino-5-phosphonopentanoic acid), 50 μM Bicuculline (Bicuculline Methiodide), and 10 μM CNQX (6-cyano-7-nitroquinoxaline-2, 3-dione).

peri-stimulus histograms were not necessarily stimulus-evoked, making this method of representing the response to stimulus erroneous. Plotting data before and after the stimulus pulse (figure 4.17) showed a change in spiking, but the change could not be appreciated qualitatively. Secondly, as MEAs record the extra-cellular potentials[6], the amplitude of the recorded evoked potentials is in general lower than those measured in a more invasive manner. Additionally, the recording hardware presented inherent noise, which may be mistakenly detected as spikes. Therefore, a high threshold for spike detection is used to eliminate the detection of spikes produced by the amplifier[7]. This may have led to the detection of fewer spikes than were actually generated. However, this threshold for spike detection was consistent for all data sets analyzed in this work.

Even so, the results regarding neuron stimulation presented in this chapter warrant further investigation into the mechanisms of magnetic stimulation and can be considered as a first step towards their better understanding. However, the method of using MEAs to study the response to stimulus allowed us to examine several aspects of magnetic stimulation that had not been quantified for micro-scale stimulation before. For example, the quantification of coupling strength due to the presence of a conducting media (PBS) strongly supports the fact that magnetic stimulation will consume less power when the air-tissue barrier is removed from the equation. Also, a one-on-one comparison with electrical stimulation helps dispel the notion that magnetic stimulation consumes several orders of magnitude higher power than electrical stimulation. For the lowest stimulus pulse tested (250 mV), that elicited a response, the power consumption for magnetic stimulation (370 μW) was within one order of magnitude of that of electrical stimulation (40 μW).

[6]This is in comparison with patch-clamps that record potentials from the cell membrane.

[7]The threshold used here is 7 times the root-mean square value of the general channel noise. A typical threshold is 5. [93]

5.7 Future Work

As magnetic stimulation does not elicit a specific behaviour in neurons as shown in the experiments above, a two-step approach may be adopted to better understand and characterize this response. The first step is to study specific neurons instead of undifferentiated neurons, such as Spiral Ganglion Neurons (SGNs) for the purposes of the studies proposed in this thesis. This would allow a direct analysis of potential use of magnetic stimulators in cochlear implants [50]. Also, it will be useful to study the response of these neurons on a large number of dishes. This will allow the researcher to establish a general trend in response to magnetic stimulation by rejecting outliers. In addition to this, drugs that alter the physiological behavior of neurons may be used to further understand the response. The most common drugs used in in-vitro experiments are synaptic blockers and Tetrodotoxin (TTX) to block the transfer of action potential and sodium channels, respectively.

Some other avenues of improvement of the proposed experimental design is through the use of a more stable amplifier for recording neuronal response, and potentially, through use of smaller, planar coils, to study spatial resolution of this stimulation technique. It must be noted that for fair comparison of spatial resolution, the magnetic stimulator and the electrical stimulator need to be at the same distance from the target neuron, as spatial resolution effects become prominent at larger distances. This can be challenging to achieve for electrical stimulation as the thin-film array is a flexible structure, so there may be a need to use a different kind of electrical stimulation array.

5.8 Chapter Summary

A setup to experimentally compare electrical and magnetic stimulation of neurons was validated. Stimulus was applied to dissociated cortical neurons plated on multielectrode arrays (MEAs) through external electrical and magnetic stimulators. Seven MEAs were plated and a set of stimuli consisting of single or multiple cycles of sine wave at voltages

varying from 175 mV to 4 V were tested for magnetic stimulation. A commercially available thin-film array was used to determine the threshold for neuronal activation using electric current in this setting, and this information was then utilized for power and heating comparison.

We also showed the steps used to analyze a set of very dense neuronal data. It was a challenge to reduce this neuronal information into easily understandable metrics. The metric used in this body of work was the firing rate per channel, to analyze the behavior of neurons before and during stimulation. Out of the six dishes tested for statistically significant change in firing rate, four showed positive results. The dishes that showed negative results were analyzed, and we observed that these dishes had very high levels of spontaneous activity, which possibly obscured the effect of stimulation on these cultures.

One of the limitations of using MEAs to perform the studies described above, was that neurons lost spontaneous activity after being left in the test incubator for a duration more than 2 hours. This implied that experiments less than 2-hour long may be performed in this setting. Another limitation was introduced by the audio amplifier that started showing non-linear behavior at input amplitudes higher than 5 V and at frequencies higher than 12 kHz. Additionally, the recording amplifier for Neurorighter also saturated at voltages larger than 3.5 mV on the electrodes, introducing noise in the recorded data for amplitudes larger than this. However, the two-hour window is the only absolute limit, as a different amplifier can always be used, and Neurorighter settings can be changed to record higher amplitudes of voltages. In conclusion, we can say that MEAs are capable of providing an inexpensive alternative to traditional in-vitro experimental setup for analyzing magnetic stimulation, if the experiments are carefully designed.

CHAPTER 6
DESIGN AND FABRICATION OF A PLANAR COIL ON FLEXIBLE SUBSTRATE

6.1 Motivation

Chapters 3,4, and 5 characterize magnetic stimulation of neurons through simulations and experiments, along with comparing it to the traditional electrical stimulation. While a better understanding of the effect of micro-scale coils on neurons needs to be developed through further experiments and simulations, we can start identifying and addressing the challenges in using such coils in a cochlear implant (CI) system, in parallel. To begin, we note that the implanted electrode array component of the CI systems will have to be replaced by a novel magnetic stimulation array that will consist of several sub-millimeter coils. These coils that would constitute the stimulation array will need to conform to the dimensions of the cochlea, as specified in table 3.3. This stringent size requirement posed by the cochlea presents a compelling need for design of coils appropriate for use in CIs. Additionally, a smaller coil[1] would allow us to perform position based probing of neurons in the setup described in the previous chapter, which may lead a more refined understanding of the induced field - neuron interaction. Moreover, researchers have suggested that the use of a planar coil instead of a solenoid will make more electromagnetic energy available for neuronal stimulation [84]. Motivated by these challenges and possibilities, we explore the fabrication of sub-millimeter planar coils.

As a first step, a planar coil is modeled in COMSOL (section 3.3.5). Next, we analyze the various options available to us for fabrication of a planar multi-turn coil. We use of additive manufacturing, informally called printing, over traditional micro-fabrication in

[1] Smaller than the size of one quadrant of the MEA (400 μm x 800 μm).

clean room because of the following reasons:

- Feature size reliably achieved through micro-fabrication on a flexible substrate ($\sim$5 μm) are similar to those achieved through aerosol-jet or industrial ink-jet printing [96].
- Printing takes considerably less time (tens of minutes, depending on the feature size) than a standard micro-fabrication process (several hours if completed in one stretch).
- Additive manufacturing is a less complicated process, so it allows for a quick feedback cycle, which is useful for novel-prototyping.

6.2 Overview

Three different additive manufacturing techniques are evaluated for their capability to produce sub-millimeter coils. The main constraint applied to these coils, in this study, is that of size. The techniques evaluated are: printing using desktop printers[2], 3-D ink-jet printing, and aerosol-jet printing. While desktop printing and aerosol-jet printing use AutoCAD generated masks, ink-jet printing requires a mask designed as a monochromatic bitmap image. The goal of this body of work is to identify printing techniques that are capable of reliably producing sub-millimeter coils for in-vitro and in-vivo testing. As the ultimate goal of fabricating these coils is to induce neuronal stimulation, several constraints other than the size are also taken into consideration while designing them. Some of these constrains are:

- Flexible substrate for ease of implantation/ to not damage neurons in-vitro.
- Bio-compatibility of the substrate and the insulation material.
- Large contact pads for interfacing with the driving circuitry.

Once these coils are designed and fabricated, the resistance of these coils is measured to estimate the conductivity of the printed traces. This provides an estimate of the current

[2]This printing method will be referred to as desktop printing for the rest of the chapter.

carrying capability of these coils. They are also examined under a 10 x magnification microscope (Carl Zeiss Microscopy, Cambridge, UK), to measure the actual feature sizes. The following sections cover the background, methods adopted, and results obtained for each of the three printing techniques, which are desktop printing, 3-D ink-jet printing and aerosol-jet printing. Then a potential existing option is analyzed and future directions are proposed.

6.3 Background

The recent years have seen great advances in the field of additive manufacturing, for generation of time-efficient and inexpensive sensors and circuits, due to an immense increase in interest in flexible electronics and internet of things [97]. These advances have lead to improvements in several key areas of additive manufacturing technology including the synthesis, deposition, curing, adhesion, and spacing of conductive inks [98]. For example, curing or sintering is the process of drying an ink and the method of curing usually has an effect on the electrical characteristics of the printed component. While traditionally curing was achieved through keeping a sample in a thermal oven for a couple of hours, now an ultraviolet pulse based curing equipment can achieve the same results in one minute. Additionally, the conductive inks are also being tested to print on various substrate materials such as paper, polyethylene terephthalate (PET), and Kapton, allowing the flexibility of choosing appropriate substrate material based on the application and future processing steps. We leverage these advancements toward exploring an alternative to micro-fabrication of coils.

Overall, the field of additive manufacturing has been developed as a cheaper and faster alternative to traditional micro-fabrication (also called subtractive manufacturing) [99]. It eliminates several etching steps thereby reducing expensive metal waste, adding to the benefits of this technology. Few groups have also explored incorporating some micro-fabrication steps into the additive manufacturing steps, thereby achieving smaller feature

sizes and reliable 3-D structures [96] [100]. This hybrid approach promises the advantages of both additive manufacturing and micro-fabrication. So, several options are available to someone looking to achieve certain results using this technology. For our project, this is a planar coil. While there are several advantages and limitations for each of these available options, instead of picking one, we decided to try three different techniques and assess them. The following subsections introduce these techniques, which are: (a) desktop printing, (b) 3-D ink-jet printing, and (c) aerosol-jet printing.

6.3.1 Desktop printing

Desktop ink-jet printing utilizes a regular office printer and prints electrically conductive ink on any substrate of choice, including paper, plastic, and polymer. The properties of these conductive inks are modified to work with the default refillable cartridges and the default ink-jet print-head of the printer. Two important components of this desktop ink-jet printer are the paper feed stepper motor and the rollers. The stepper motor is responsible for controlling the rate at which the rollers move and rollers move the sheet from the tray or feeder and advance it when the print head assembly is ready for another pass. The print-head for such a piezoelectric ink-jet printer works as follows:

- An ink tank (marked as (a) in figure 6.1) supplies ink to the printer setup through capillary action and a droplet of ink is waiting at the very end of this tube (marked as (b)).
- When the printer is ready to print, the electrical contacts (marked as (c)) are energized, which in turn energizes the piezoelectric crystal (marked as (d)).
- This causes the crystal (d) to flex out and press against the membrane (marked as (e)). The outward movement of the membrane causes it to crush against the hole (marked as (f)).

- This increases the pressure at the tip of the tube (b) causing the ink droplet to dispense out.

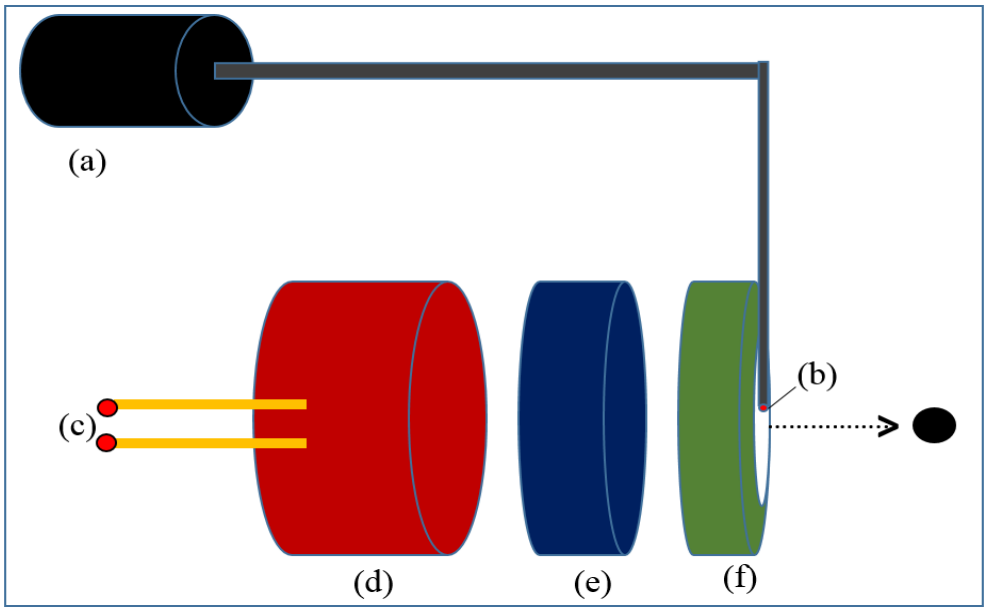

Figure 6.1: Schematic showing the mechanism of piezoelectric ink-jet printing. Here, (a) represents the ink tank, (b) represents a droplet of conductive ink, (c) is the electrical contacts, (d) represents a piezoelectric crystal, (e) represents a membrane, and (f) is the hole through which mechanical movement of the piezoelectric crystal is converted into a signal to print. (Source: [101])

An average ink-jet printer can print 600 dots per inch (dpi), which corresponds to a diameter of 42 μm per dot. The high resolution printers can print up to 5000 dpi, which corresponds to a diameter of 5 μm per dot. However, these numbers are for ink printed on paper. This resolution changes for conductive inks because of the surface chemistry of the ink and the substrate, which leads to the spreading out of each ink droplet, resulting in much poor resolution.

We next explore the 3-D ink-jet printer which provides the capability of printing multiple layers of conductor and polymer on to a substrate. This is ideal for the printing of multi-turn inductors.

6.3.2 3-D ink-jet printing

3-D ink-jet material printers are used to print multiple layers of conductive inks and polymers on top of each other to create 3-D structures such as inductors, antennae, and 3-D capacitors [102]. While the print-head works similar to the description provided in the previous subsection, the primary purpose of this printer is to print conductive traces. Several aspects of this process have been studied in great detail over the last decade including the behavior of the ink drop jetted out from the print-head, the effect of size of the print-head nozzle on the printed trace, the mechanical properties of the ink droplet including viscosity and surface tension, and the interaction between the ink and the substrate [98]. With improved understanding of all these aspects of printing, the solvents carrying the ink have been successfully optimized to achieve consistent application-based performance. Additionally, some groups have also used techniques like UV-ozone exposure to modify substrate properties to facilitate better printing [103].

A typical Dimatix Materials Printer DMP-2850 (Fujifilm, Tokyo, Japan) can print metal with a thickness of 500 nm per pass. Typically three to five passes are used for each layer. The volume of each drop of ink varies between 1 pL to 10 pL, and up to five metal layers with a total thickness varying from 4 μm to 100 μm can be printed. This printer can also print dielectric materials with their thickness varying between 200 nm to 200 μm per layer. SU-8 in particular can be printed at a thickness of 6 μm per pass [102] [100]. Some of the factors that affect the feature sizes in this method of printing are: (a) viscosity of the ink, (b) spacing between each droplet of ink, (c) number of layers or cartridge passes, and (d) surface chemistry of the substrate material, determining how much a drop of ink spreads.

We next look at aerosol-jet printing which offers the advantage of printing on curved surfaces, which may be beneficial for cochlear implants.

6.3.3 Aerosol-jet printing

Aerosol-jet printing (AJP) is another additive manufacturing technique that can achieve feature sizes as small as 10 μm [104]. This technique shares the the qualities of increased rate of manufacturing and reduced amount of waste with ink-jet printing. AJP is relatively new compared to ink-jet printing and there are several fundamental differences between the two techniques. An aerosol-jet printer uses an aerosol of ink, typically created by an atomizer, along with a carrier gas to spray the ink on the substrate, whereas, ink-jet printing places individual drops of ink on the substrate that combine to form a continuous layer. The print-head-equivalent in this system is a deposition head[3], whose tip has an opening with diameter between 100 μm and 300 μm. To allow fine features to be printed on a substrate, the aerosol-carrying nitrogen is combined with a second gas flow, called the sheath flow, such that the two gases flow co-axially throught the tip of the dep-head. The rate of sheath flow determines the thickness of the features printed, along with the diameter of the tip. Mahajan et al. identified the focus ratio, which is the ratio of the sheath gas flow rate to the atomizer gas flow rate, as a key quantity in controlling the aspect ratio of the line [105]. The process of printing out the patterns is carried out by an automated platen or stage, such that the tip remains fixed and the platform carrying the substrate moves around. These aerosol-jet printers come equipped with custom software to enable smooth operation of the equipment. An overview of working of the AJP is illustrated in figure 6.2.

Aerosol-jet printing is conformal and the dep-head does not need to come in contact with the substrate, allowing printing on uneven or curved surfaces, and also on top of existing patterns. The aerosol may consist of materials in different phases such as liquid chemicals, solvents and solid particles. This system is compatible with a large variety of ink materials such as metals, polymers, conductors, and insulators. Moreover, this printer can also be used to print biological materials such as enzymes, proteins and cells on to substrates [107].

[3]Referred to as dep-head now on.

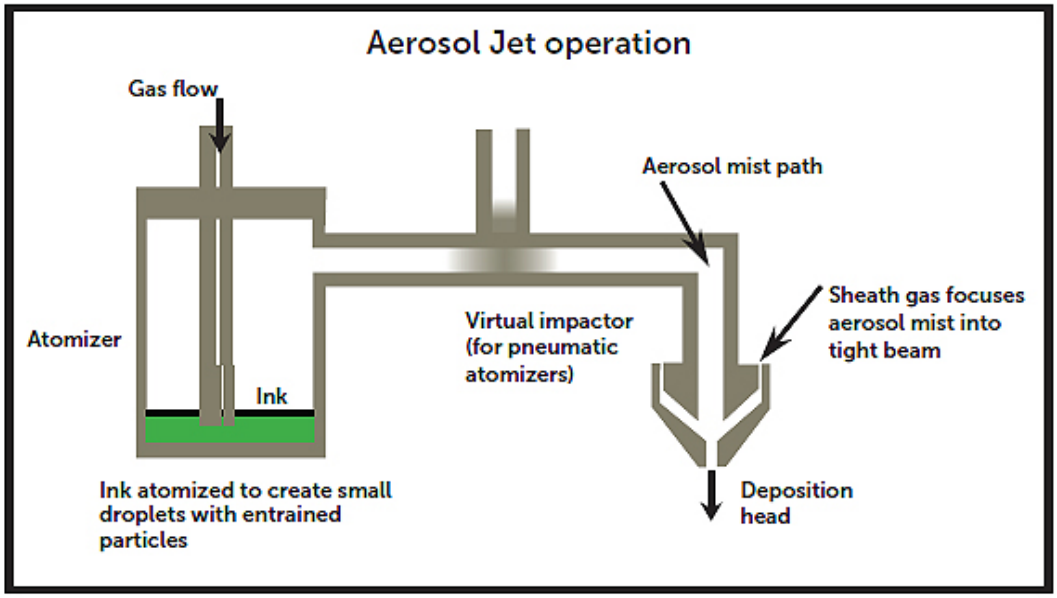

Figure 6.2: Artwork showing the components and working of an aerosol-jet printer (Source: [106])

6.4 Methodology

This section specifies the equipment used, illustrates the masks designed, and provides other pertinent details related to our work. We collaborated with three different labs at Georgia Institute of Technology to try the three different printing methods. The Computer-Aided Simulation of Packaging Reliability (CASPaR) Lab at the manufacturing research center[4] helped us with the desktop printing. The A.T.H.E.N.A. Research Group[5] helped us with the ink-jet printing, and the Yeo research group[6] helped us with the aerosol-jet printing.

6.4.1 Desktop printing

Among the three different printing techniques analyzed, desktop printing is found to be most easily accessible and replicable as the apparatus costs a very nominal amount -$110 for the printer and $335 for the cartridges (NovaCentrix, Austin, TX), and the mask may

[4]Lab Director: Dr. Suresh Sitaraman, Woodruff school of mechanical engineering; Students: Christina Taylor and Isaac Bower.

[5]Lab Director: Dr. Emmanouil Tentzeris, Van Leer, Department of electrical and computer engineering; Student: Bijan Tehrani.

[6]Lab Director: Dr. W. Hong Yeo, Woodruff school of mechanical engineering; Student: Saswat Mishra.

be designed using any software capable of producing a PDF output. The NovaCentrix starter kit (used for our project) comes with a printer, a set of cartridges for conductive ink printing, and a ream of PET sheets that have a micro-porous ink-jet-receptive coating on them. This entry level kit uses a common off-the-shelf piezoelectric on-demand ink-jet printer with refillable cartridges. These cartridges are filled with aqueous-solvent based patented nano-particle conductive ink -Metalon JS-B25P - capable of being cured at room temperature [108].

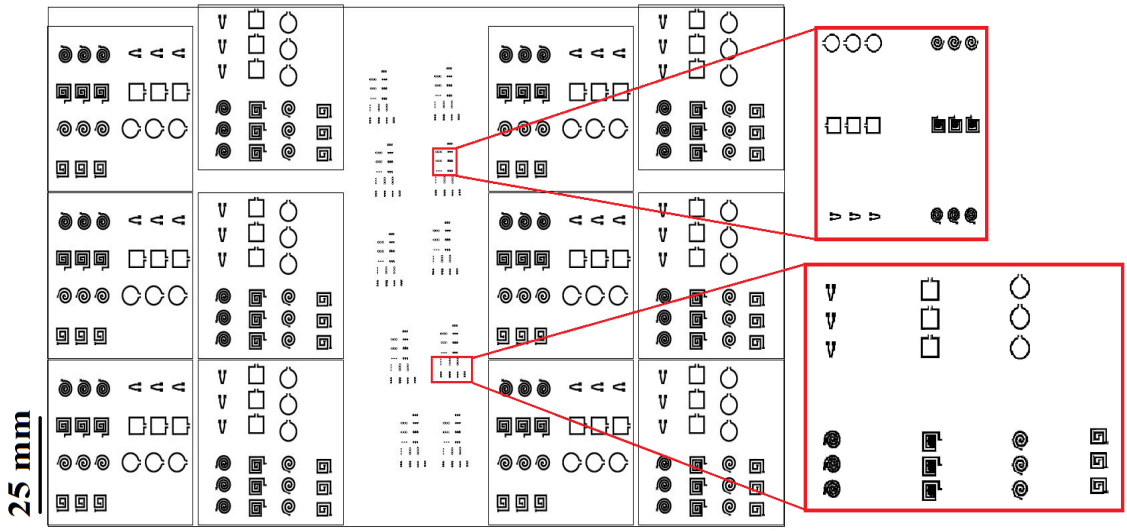

Figure 6.3: Mask designed using AutoCAD software for desktop printing. The smaller coils have a trace width of 50 μm and the larger coils are 10x larger, so the critical trace dimensions are $\sim$500 μm

We used this starter kit in collaboration with the CASPaR lab. Once the printing process was understood, a mask was designed using AutoCAD (Autodesk, San Rafael, CA), to be printed (figure 6.3). The initial mask prepared had critical dimensions of $\sim$50 μm, which was transformed into a mask with 10x dimensions, in addition to the original designs to better evaluate the limits of printing using this setup.

6.4.2 3-D ink-jet printing

An industrial ink-jet printer by Fujifilm (Dimatix Materials Printer DMP-2850 with DMC-11610 cartridge) was used to print coils with feature sizes as small as $\sim$50 μm in collabora-

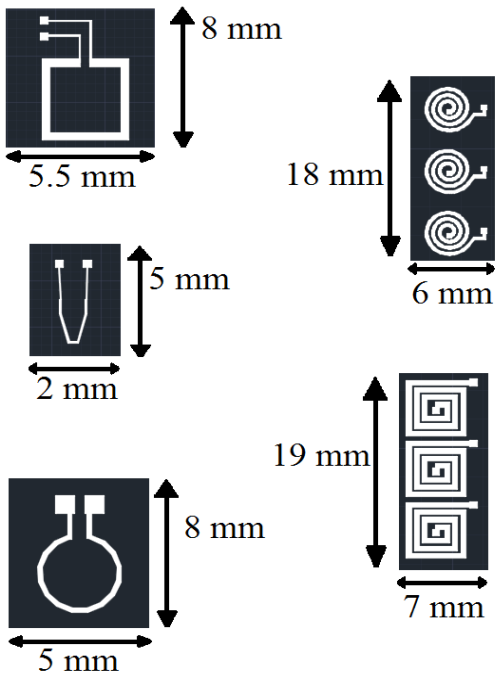

Figure 6.4: A figure illustrating the dimensions of the larger features from figure 6.3. The critical dimension of each feature is 50 μm. This thickness is assigned by changing the line width of the features in AutoCAD.

tion with the A.T.H.E.N.A. lab. To leverage the in-house expertise of this group a 4-layer mask was first designed using AutoCAD, complete with alignment markers as .dwg and .dxf files. However, the small feature sizes (critical dimension of 30 μm) demanded by our project led to errors while downloading these files into the printer in the Gerber format (figure 6.5a). The mask was then modified, but these modified mask designs also faced problems where there were many deviations in the width of the traces and gaps between them (figure 6.5b). Such errors are usually observed when dealing with small feature sizes, so an alternative approach to mask design was adopted where the features were hand-drawn in MS-Paint. A monochromatic bitmap file was created where every black pixel represented a metal drop and every white pixel represented the absence of metal. The pixels translate to printed drops for the pattern, where the scaling is determined by the drop spacing used in the printer (typically 20–30 μm). For example, a 36 x 35 pixels image with the desired drop spacing of 30 μm translates into a printed pattern of 1.08 x 1.05 mm.

(a) Type 1 error (b) Type 2 error

Figure 6.5: Errors observed while downloading .dxf file into the ink-jet printer. In errors of type 1, an extra strip of metal erroneously appears in the downloaded file. In errors of type 2, the printer reads the input file to be discontinuous. As these printers work on a drop-on-demand basis, discontinuities in mask will translate to discontinuities in the printed traces.

The first set of masks designed used a single white pixel representing the gaps between traces with the assumption that a 30 μm ink drop would expand up to $\sim$50 μm, but still allow some gap between two consecutive traces. However, preliminary testing proved that a one-pixel gap was too little between two metal traces. So, the final mask design has one black pixel representing metal and two white pixels representing the gaps between traces (figure 6.6). The steps involved in the printing these coils are as follows:

- The files are loaded into the printer and the printer temperature is set at 60°C to allow rapid drying of the ink after each run.
- An initial line of horizontal ink is printed on the Kapton substrate, as reference for alignment.
- The first layer (figure 6.6a), which is a layer of metal consisting of silver nano-particles is printed. This layer comprises of three layers of metal, where five minutes are allowed for drying after printing each layer.
- Layer 2 (figure 6.6b) is the dielectric layer where SU-8 is printed, followed by a

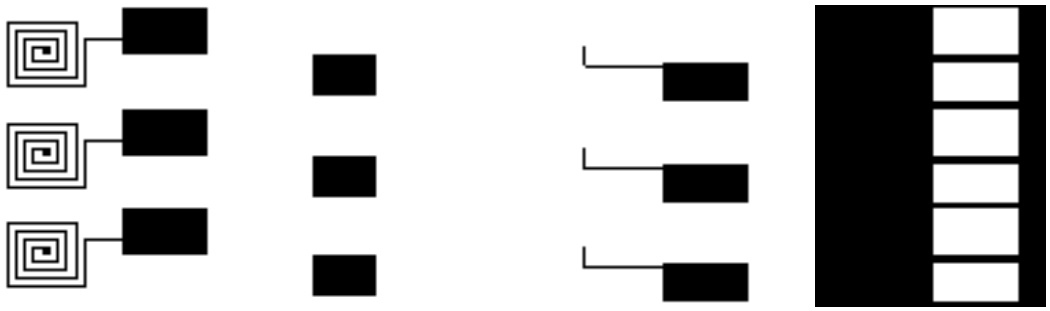

(a) layer 1: metal (b) layer 2: SU-8 (c) layer 3: metal (d) layer 4: SU-8

Figure 6.6: 4-layer mask for ink-jet printing designed using MS-Paint. The first layer (a) is a layer of silver-nano-particle ink, which is covered by a layer of SU-8 (b), leaving some metal in the centre exposed. The second layer of metal (c) is drawn on top of this layer, which is finally followed by the final encapsulation layer of SU-8 (d), leaving only the two leads exposed.

four-step bake and UV-exposure process described below. This is a single layer of SU-8, which serves to insulate a small section in middle exposed, to enable connecting contact pads to the inner end of the coil.

- Following the UV Ozone exposure, layer 3 (figure 6.6c) of silver-ink is printed. This layer also consists of three layers of metal where each layer is allowed to dry for five minutes. This layer connects the inner end of the coil to the contact pads.

- Finally, layer 4 (figure 6.6d) is printed and the first three steps of the 4-step bake are repeated. This layer insulates the entire structure, leaving only the contact pads exposed.

- Following the curing of SU-8, the Kapton film is sintered at 180°C for about two hours to allow the nano-particles to bond and form a continuous layer.

A four-step bake and UV-exposure process is used to cure the printed SU-8 layers. The steps followed are listed below:

- First a hot-plate bake at 60°C to 100°C is performed over ten minutes (soft-bake).

- Then a UV-exposure is performed, the duration of which depends on the thickness of the SU-8 layer. UV crosslinking: UVP CL-1000 Ultraviolet Crosslinker is used for this step and for a layer thickness of $\sim$15 μm, 300 $\frac{mJ}{cm^2}$ exposure is used.

- Another hot-plate bake is performed following the UV-exposure at 100°C for seven minutes.

- This is followed by a UV Ozone (O3) exposure (UV ozone: Jelight UVO Cleaner Model No. 42), performed before silver is printed onto SU-8 to modify the surface energy of the printed SU-8 and to ensure good wetting of the silver ink. In our case an exposure of 2.5 minutes was used.

6.4.3 Aerosol-jet printing

The Aerosol Jet (AJ) 200 system (Optomec, Albuquerque, NM) is used, in collaboration with the Yeo research group, to print coils on Kapton sheets (DuPont, Wilmington, DE) and on cochlear implant insertion devices. The ink used is the EXPT Prelect TPS 50G2 ink by Clariant (Muttenz, Switzerland). This AJ system provides the ability to print fine-feature electronic, structural, and biological patterns on almost any surface, with feature sizes as small as 10 μm. In addition, it comes with a graphical user interface (GUI) to aid in printing material. The input for this system is provided in the form of masks designed using AutoCAD. Unlike the masks designed for desktop printing, there is no need to specify the thickness of the traces to be printed in this method of printing. Initially the coils were printed on Kapton tape and the CI insertion device (figure 6.7). However, the contact pads on these patterns were too small to be easily accessed, so, new masks were designed with larger contact pads (figure 6.8). In order to cure the printed silver inks, the substrate is put in a thermal oven for one hour at 200°C.

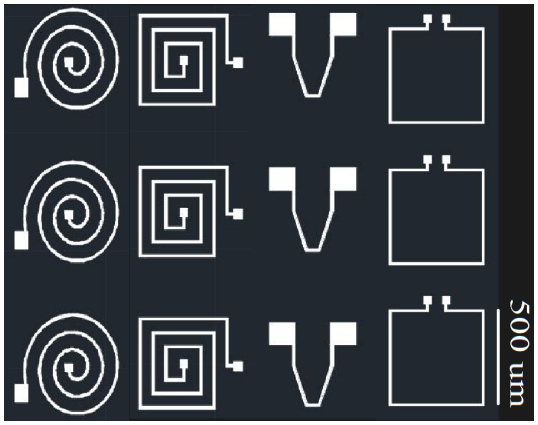

Figure 6.7: Mask for aerosol-jet printing showing features with small contact pads

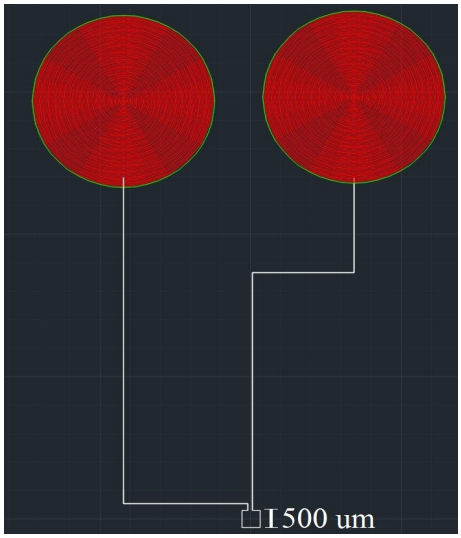

Figure 6.8: Mask for aerosol-jet printing showing features with large contact pads

6.5 Results and discussion

This section presents the printing results and discusses the characteristics of the coils printed using each technique. The following subsections discuss the results from each technique in detail.

6.5.1 Desktop printing

Desktop printing was observed to be sub-optimal for printing features with critical dimensions of $\sim$50 μm. This observation is attributed to the rate at which the paper feed stepper motor feeds the PET sheet into the printer, which results in discontinuity in the printed traces. Feature sizes as small as 50 μm correspond to a single line of printing by the printer, meaning, this printer cannot print a line smaller than $\sim$50 μm. Additionally, the conductive inks are dissolved in a solvent for ease of printing so, after curing, the printed traces for the smaller features ($\sim$50 μm) are not dense enough to be conductive. As a result, most of the printed designs with these feature sizes had very high resistance values, in the range of a few mega-ohms (representing an open circuit; figure 6.11). This printing technique performed much better for critical dimensions of $\sim$500 μm. As a result, some of the larger coils had higher conductivity, thus lower resistance values, typically in the range of 2-5 ohms (figure 6.9– 6.10).

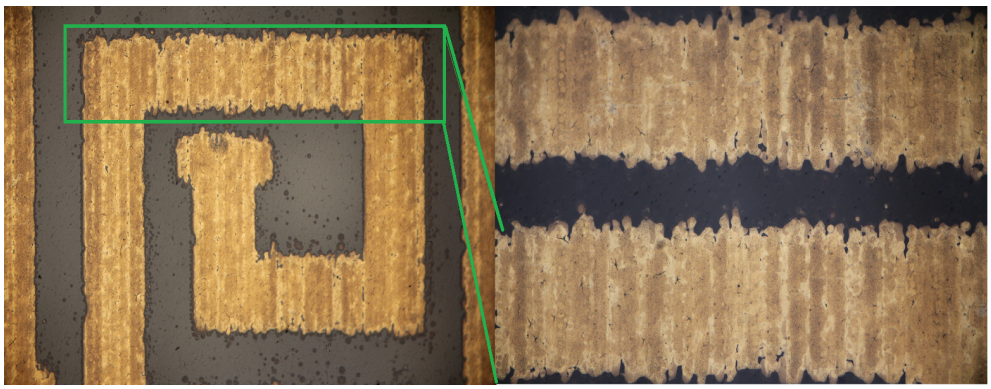

Figure 6.9: An image of a rectangular coil with critical dimension of 500 μm printed using desktop printing on a PET sheet

Figure 6.10: An image of a circular coil with critical dimension of 500 μm printed using desktop printing on a PET sheet

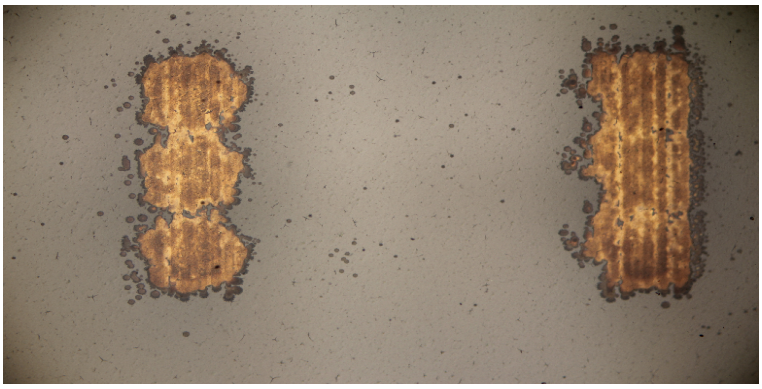

Figure 6.11: An image of a rectangular coil array and a circular coil array with critical dimension of 50 μm printed using desktop printing on a PET sheet

A challenge that presented itself even at these early stages was how to interface such a coil with a setup similar to the driving-circuit and multielectrode array setup discussed in chapter 4. Usually, Silver-epoxy, which is a two-part epoxy from Electron Microscopy Sciences (Hatfield, PA; part number 12670-EE), is used for interfacing with such circuitry. However, we observed that while the larger coils were easier to interface with, they were too large to be used with the MEAs, whereas the smaller coils were almost an open circuit and really difficult to interface with. So, we looked at other options which offered the possibility of printing electrically continuous coils with small feature sizes in the range of $\sim$50 μm.

6.5.2 3-D ink-jet printing

The coils produced using 3-D ink-jet printing had critical dimensions of $\sim$50 μm and an array of three coils was successfully printed. The overall dimension of these coils turned out to be 750 μm by 750 μm. Figure 6.12 shows an image of such an array of coils complete with a top SU-8 layer, insulating the entire assembly other than the contact pads. As mentioned

in section 6.4.2, these coils are printed in 4 different layers. Figure 6.13 illustrates the first three layers, i.e., the base metal layer, the intermediate SU-8 layer, and the top metal layer. While printing these coils was over all successful, slight misalignment resulted in highly displaced assemblies as shown in figure 6.14. As a result, only two out of 12 printed arrays were properly aligned and were used for resistance measurement.

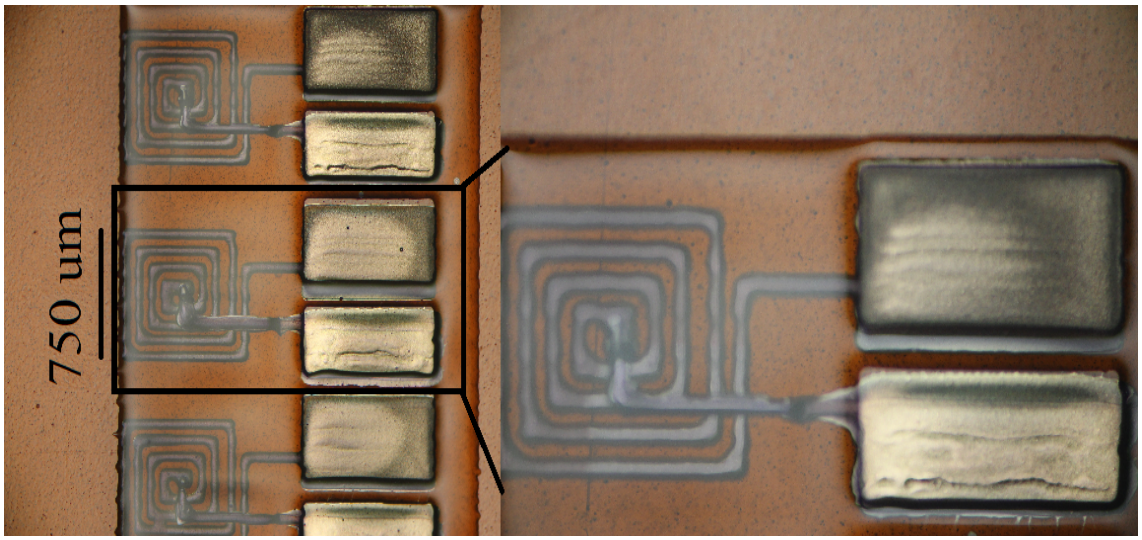

Figure 6.12: An array of coils printed using 3-D ink-jet printing. Slight misalignment between the contact pads and the layer of silicone is seen in the inset. Each turn has a width of $\sim$50 μm and the height of the entire structure is measured to be $\sim$9 μm using a profilometer.

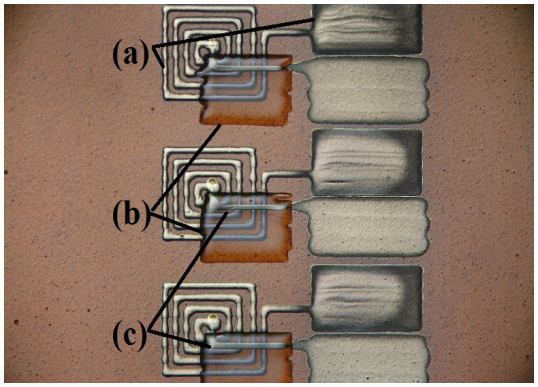

Figure 6.13: Image illustrating first three layers of ink-jet printing. (a) represents the first layer of metal, which includes the entire coil and the contact pads; (b) represents the SU-8 layer which insulates a part of the printed coil; (c) represents the second metal layer which connects the inner end of the coil to the contact pads.

Figure 6.14: Observed printing defects due to misalignment during 3-D inkjet printing.

Figure 6.15: 50x image of the printed coils with a focus on one of the edges.

One of the objectives of printing coils with edges (not circular) was to potentially exploit the asymmetry in the induced electric fields at these edges [66]. To examine this, the printed coils were observed under a 50x magnification lens (figure 6.15). It was observed that the edges were curvy and not sharp, however, the effect of this geometry on the induced fields may only be observed through testing.

6.5.3 Aerosol-jet printing

We utilize the conformal nature of aerosol-jet printing to print a set of coils on a cochlear insertion device as a proof-of-concept (figure 6.16). Figure 6.17, on the other hand, shows coils printed on a Kapton tape. Though both these sets of coils were printed within a few minutes, the contact pads were too small in both cases to be easily accessed, so these coils had to be redesigned and reprinted.

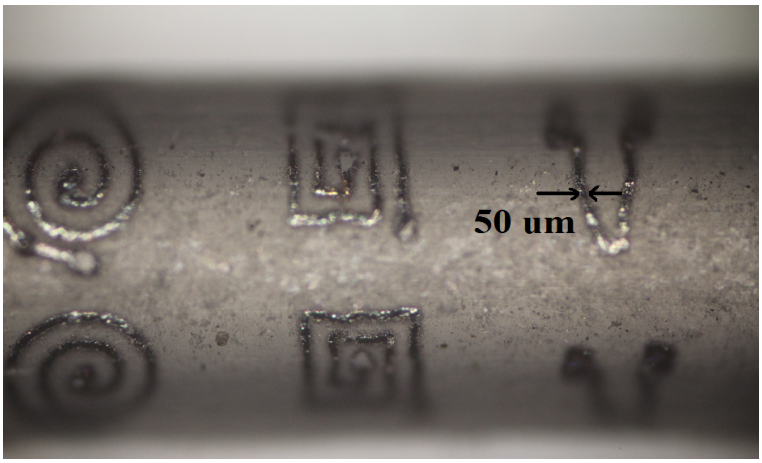

Figure 6.16: Aerosol-jet printed coils with small contact pads on a cochlear insertion device. The curvature of the device precludes good photography of the printed coils.

Printing larger contact pads took longer time, and a consistent misalignment issue was encountered while printing such coils (figure 6.18). These coils had more discontinuities and often resulted in open circuits, which may be attributed to the mismatch between the speed of printing and degrees of freedom of the platen. However, a couple of single loop coils were successfully printed and were used as representative coils for this printing style. We also tried multi-layer printing using this technique, but the results were not very promising-

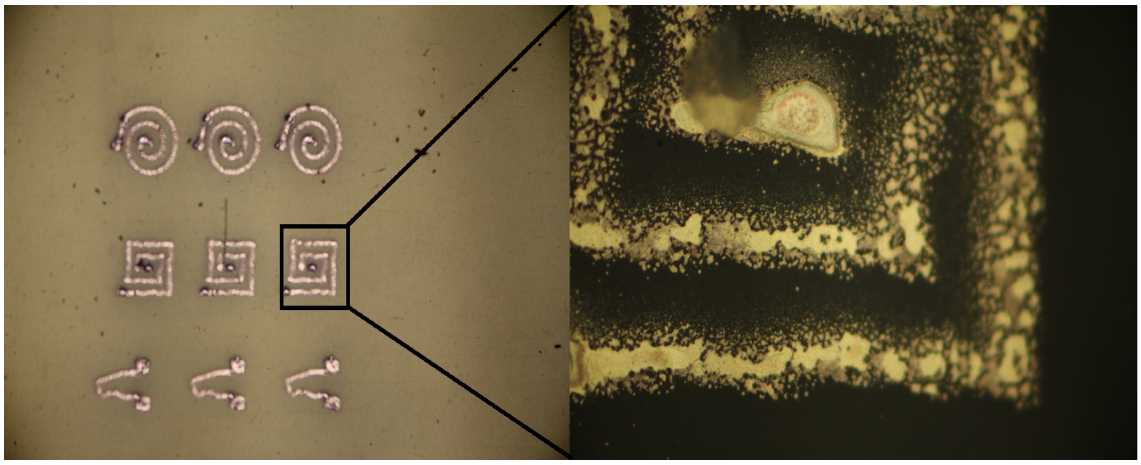

Figure 6.17: Aerosol-jet printed coils with small contact pads on a Kapton tape. The inset shows a 50x image of a rectangular coil. The dispersed ink deposition, characteristic of aerosol-jet printing, is evident.

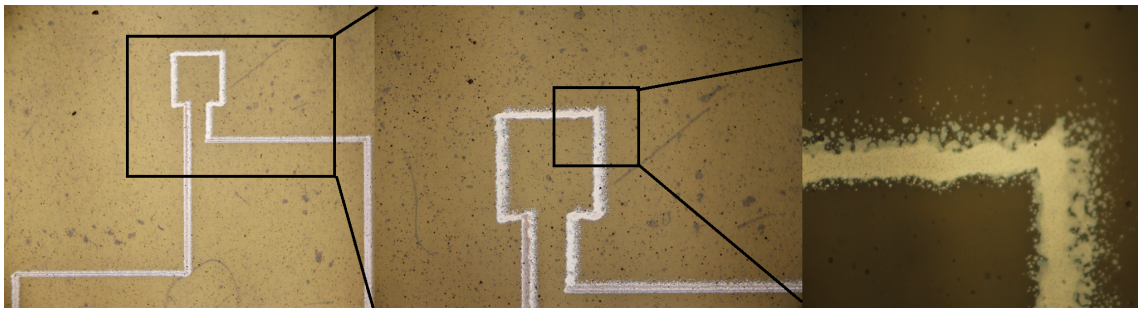

Figure 6.18: Image shows a single square loop with leads leading up to large contact pads similar to figure 6.8. Insets show 10x and 50x magnification.

Table 6.1: Resistance of the printed coils

Printing technique used	Resistance in Ohms
Desktop printing	9.76
Aerosol-jet printing	40
Ink-jet printing	5.16

the polymer layer was very dispersed and there were alignment issues with printing the second layer of metal. Overall, this technique seems useful for printing fine features with small contact pads on uneven, curved surfaces.

6.5.4 Electrical measurement of the printed coils

From each set of printed coils, a few samples were selected and their resistance was measured. For the coils printed using desktop printer, the smaller coils showed really high values of resistance, corresponding to open circuits, so the resistance for only the larger coils is reported. All measurements were performed using a FLUKE 73 III digital multimeter (Everett, WA). These results are presented in Table 6.1.

To estimate the inductance of these coils, a theoretical approach was adopted where the formulae proposed by [109] were used [110]. In this method, three different inductance values are calculated based on three different estimation methods. The average of these three values are reported. These values are calculated based on the following parameters: (a) number of turns, (b) distance between the turns, (c) width of the traces, and (d) outer diameter of the coil. The inductance values calculated are:

- $\sim$78.17 nH for the larger square shaped coils printed using desktop printing (figure 6.4). The trace width for this coil is 500 μm and the overall dimension is 7 mm.
- $\sim$6.68 nH for the coils printed using 3-D ink-jet printing (figure 6.12). The trace width for this coil is 50 μm and the overall dimension is 750 μm.

- $\sim$2.44 nH for the square coils printed using aerosol-jet printing (figure 6.16). The trace width for this coil is 50 μm and the overall dimension is 500 μm.

We cannot comment on the capability of these coils to induce neuronal stimulation based on these parameters. However, from a purely theoretical perspective, larger number of turns, leading to higher inductance values are desirable.

6.6 Existing options

The smallest, commercially-available coils measure 400 μm by 200 μm in size and are readily available through Digi-Key (Thief River Falls, MN). Table 6.2 shows some of the properties of these coils when compared with the coils that were actually tested during this thesis, and the properties relevant for magnetic stimulation are highlighted. These coils, which are smaller in dimensions, may potentially be used to stimulate cochlear neurons although, lower inductance may warrant higher power. Moreover, as cochlear implants require an array of electrodes to stimulate multiple areas inside the cochlea, use of these commercially available coils for this application would require a packaging strategy designed to integrate these commercially available coils into an array. Additionally, the flexibility to modify the design of the inductor as per our requirements is lost, hence we lean towards an in-house design and fabrication of micro-scale coils; which will allow the design and printing of an entire circuit. This circuit could be partly printed and partly fabricated to achieve the desired functionality - an array of inductors, capable of inducing neuronal response inside the cochlea.

6.7 Discussion

During the in-vitro experiments, it was observed that a shielded inductor did not induce neuronal modulation as well as an unshielded inductor. The difference between these two inductors is that a shielded inductor is designed to keep most of the magnetic flux within

Table 6.2: Comparison between commercially available small coils and the coils tested

Properties	Commercially available coil	Tested coil
Size	0.4 mm by 0.2 mm	1mm by 0.5mm
Inductance	39 nH	100 nH
Current rating	90 mA	90 mA
Type	thick film	multilayer
DC Resistance	7 Ohm max	5.5 Ohm max
Unit Price (USD)	0.13	0.07

itself, thereby not interfering with neighboring circuit elements, whereas an unshielded inductor is more likely to interfere with the neighboring circuitry [111]. The coils designed in this chapter are unshielded, and being planar, they have an even lower tendency to store magnetic energy, implying that most of the generated energy will be available for neuronal stimulation. However, studying the effect of these coils as a function of distance from the neurons will be interesting, because the fields induced through this coil decrease rapidly, compared to a solenoid coil.

6.8 Future directions

Upon evaluation of the three printing techniques described in this chapter, it is concluded that ink-jet printing may be the best alternative for developing micro-coils in-house. However, the challenge of efficiently interfacing with the coil so as to test on a setup similar to that described in chapter 4 remains. Perhaps, the coils can be printed on substrates designed to fit in the desired experimental setup. Additionally, given the capability of this printing technique to print multiple layers, a 3-D inductor maybe designed to amplify the fields induced. Aerosol-jet printing is also an attractive option, with its conformal printing capabilities. But, further research needs to be conducted to print multi-turn coils, as they typically require more than one layer of metal. Finally, the problem of lack of accessibility to the contact pads can be solved by developing the entire circuit prior to printing and printing

contact pads as per these circuit requirements. The true value of these printed coils lie in their capability to elicit neuronal responses. So it is important to test out the capabilities of these coils to modulate neuronal activity and develop a quick feedback cycle to further optimize coil design.

6.9 Summary

In this work, three different additive manufacturing techniques are evaluated for their capability to produce sub-millimeter coils. These three techniques are: ink-jet printing[7], 3-D ink-jet printing, and aerosol-jet printing. Masks for each technique is designed, then the coils are printed and analyzed. It must be noted that all techniques use silver nano-particle based inks for printing, but from different manufacturers. Table 6.3 summarizes these results.

Table 6.3: Summary of printing sub-millimeter coils

Method	Ink-jet	3-D ink-jet	Aerosol-jet
Ink used	Metalon JS-B25P	DMC-11610 cartridge	EXPT Prelect TPS 50G2
Substrate	PET	Kapton	Kapton
Critical feature size	500 μm	50 μm	50 μm
Overall feature size	7 mm	750 μm	500 μm
Number of turns	3	4.25	3
Mask input file	.pdf	.bmp	.dxf
Insulating layer	None	SU-8	None
Number of layers printed	1	4	1
Time taken in minutes	3-5	120	3-5

[7] Also called desktop printing as it uses desktop printer.

CHAPTER 7
CONCLUSION

7.1 Thesis conclusions

This thesis evaluated micro-scale magnetic stimulation through finite-element analysis and in-vitro experiments, and highlighted the need for an even better understanding of the interaction of induced-fields with neurons. We demonstrated that sub-millimeter coils are capable of modulating neuronal activity at voltages as low as 1 V applied to the coil. The nature of this response was measured in terms of a change in the firing rate of neurons. Power consumption and heating were calculated for the modeled inductors, then compared with values measured experimentally. We also compared this stimulation technique to the state-of-the-art electrical stimulation. Finally, additive manufacturing techniques were evaluated for their capability to produce sub-millimeter coils. The important contributions of this thesis are:

- Evaluation of induced electric fields and its derivative (activating function) to show that orientation of the stimulating coil (a solenoid) with respect to the axis of a group of axons has an effect on the coil's capability to induce neuronal modulation.
- Comparison of activating function induced by magnetic stimulation to that induced by electrical stimulation, to highlight better spatial resolution in the case of magnetic stimulation.
- Calculations predicting that power consumption and heating can be limiting factors for micro-scale magnetic stimulation at high repetition rates of stimulation.
- Experimental validation that multielectrode arrays can be used to study micro-scale magnetic stimulation in-vitro.

- Experimental validation that sub-millimeter coils induce a statistically significant change in the firing rate of dissociated cortical neurons plated on a multielectrode array.

- Experimental validation that 3-D ink-jet printing can reliably produce sub-millimeter coils that may be interfaced with the in-vitro experiment designed in this thesis.

The models developed in COMSOL were refined using the parameters used during experiments, and a validation of the predicted values, such as temperature change and power consumption, was carried out. The stimulation thresholds for magnetic stimulation were also predicted by calculating the induced electric field, and the activating function values due to the parameters used during experiments. These thresholds were found to be much lower than the generally accepted threshold of 10 V/m [80]. Finally, planar sub-millimeter coils were fabricated using state-of-the-art additive manufacturing techniques, and their electrical properties were analyzed.

7.2 Future work

This work models the stimulation electrodes and predicts their effect on axons through the activating function. While this is a good approximation of the first order effects of stimulation, more detailed neuronal models may be added to study these effects in detail, similar to the studies with external field generators [43] [112]. In addition, several improvements to the in-vitro study can be made.

One of the limitations of using MEAs to study stimulus evoked responses in cortical neurons is that the resolution of monitoring cellular activity is low. This means, though we study a large population of neurons, we cannot access all of them because of the following reasons: (a) the number of recording electrodes is small (n = 59), (b) not all channels are available for recording due to amplifier instability, and (c) the neuronal activity is recorded using extra-cellular electrodes. Though there are ways to overcome each of these issues,

the need to overcome them will depend on the experimental design. For example, it will be beneficial to compare the spatial resolution of magnetic stimulation vs. electrical stimulation experimentally, to pursue magnetic stimulation as an alternative to electrical stimulation in cochlear implants. For this study, there is a need to study a population of neurons, so extra-cellular recording will be apt, as opposed to cell-attached patch clamp-like intracellular recording, which allows better sensitivity but less global response. The density of electrodes required will depend on the desired resolution, where more electrodes equal better resolution. However, amplifier stability will be important for this study, so there is a need for a more stable recording amplifier.

To compare the spatial resolution of magnetic stimulation vs. electrical stimulation, there is also a need to have the electrical and magnetic stimulation sources with the same dimension, so that the effects of stimulation may be compared objectively. This requires the fabrication of a coil, and an electrode with the same outer dimensions. Additionally, it is important that both these sources of stimulation are at the same distance from the target neurons, as the effect of spatial resolution is easier to observe from a distance. We thus identify a need to fabricate a hybrid array (potentially through additive manufacturing), with both magnetic and electrical stimulation capabilities. A first step here could be to interface the coils fabricated in chapter 6 with the setup described in chapter 4, characterize their ability to stimulate neurons, and then modify the coil design based on the results of this experiment.

Finally, there is a need to understand and characterize micro-scale magnetic stimulation better. The studies so far, including this one, show the effects of magnetic stimulation on a set of neurons. However, similar to electrical stimulation studies, there is a need to study the mechanisms of stimulation in greater detail, and the first step toward that goal is to have some basic standardized protocols to follow. For micro-scale magnetic stimulation, most studies use the same 100 nH inductors, and audio amplifier as used in this study. Some studies have reported innovative coil designs, while others study different types of neurons

in-vitro, and in-vivo [64] [66]. Most of the stimulation pulses used are either sinusoidal or rectangular pulses, but a well-established threshold has not yet been defined. Multielectrode arrays do provide a standard testing platform that is capable of functioning with different types of neurons, and may be the platform that this field of research needs. Even though there is poor resolution of neuronal activity compared to cell-attached patch clamps, studying a large population of neurons in an isolated system like the MEA is needed to establish the clinical viability of micro-scale magnetic stimulation.

Appendices

APPENDIX A

MATHEMATICAL PREAMBLE FOR FINITE-ELEMENT MODELLING

The pilot study was encouraging and provided a solid base to set-up the problem for finite-element analysis (FEA). To broadly define our problem, we consider the two Maxwell's equations that best sum up the working of microscopic-magnetic stimulator. In their most basic form they are as follows:

$$\nabla \times \mathbf{E} = -\frac{\partial \mathbf{B}}{\partial t} \tag{A.1}$$

$$\nabla \times \mathbf{H} = \frac{\partial \mathbf{D}}{\partial t} + \mathbf{J} \tag{A.2}$$

where **D** represents the displacement current or the electric flux density, **H** represents magnetic field, **B** represents magnetic flux density, **E** represents electric field and **J** represents the current density. ∇ is the differential vector operator used to represent the curl (cross product) of these field vectors. As per equations (1) and (2) a changing magnetic field induces electric field whereas, electric current and changing electric flux produce magnetic field. These form the basic principle of operation of the micro-magnetic stimulator.

A direct implication of the Maxwell's equations is based on the finite speed of electromagnetic waves. There is time-retardation in the fields produced by a source. However, in some cases, where the ratio between the size of the object and the electromagnetic wavelength of the excitation is small enough, these effects can be neglected. The measure of the above mentioned ratio is called electrical size. Studies where this delay may be neglected fall under the quasi-static domain [113]. In magnetoquasistatic fields, the Ampere-Maxwell law takes the following form:

$$\nabla \times H = J \tag{A.3}$$

That is, the time rate of change of electric flux density can be ignored. Inductors used for the stimulating the cochlea along with their stimulation parameters, fall under this category of quasi-statics. Here the current is given by:

$$\mathbf{J} = \sigma \mathbf{v} \times \mathbf{B} + \mathbf{J}^e \tag{A.4}$$

$\mathbf{J}^e$ represents the external current density and $\mathbf{v}$ is the charge velocity [114]. The variable to be solved for using the partial differential equations formulation is $\mathbf{A}$, the magnetic vector potential. The relation between magnetic flux density and $\mathbf{A}$ is $\mathbf{B} = \nabla \times \mathbf{A}$. Using the constitutive relation $\mathbf{B} = \mu_0 \mathbf{H}$ in conjunction with the expression for $\mathbf{A}$ gives us the final equation in magnetostatics:

$$\nabla \times (\mu_0^{-1} \mu_r^{-1} \nabla \times \mathbf{A}) - \sigma \mathbf{v} \times (\nabla \times \mathbf{A}) = \mathbf{J} \tag{A.5}$$

However, no electromagnetic problem is complete without a set of boundary conditions at various interfaces between materials and physical boundaries. In the case of modeling fields in tiny inductors, magnetic insulation was applied at the boundary of physiological components, given by $\mathbf{n} \times \mathbf{A} = 0$. This formulation also utilizes the geometrical symmetry in order to further simplify the solution. In addition to these, the time varying current was modeled using the following equations:

$$I_{coil} = \int \mathbf{J}.e_{coil} \tag{A.6}$$

$$J_e = \sigma \frac{V_{coil}}{2\pi r} e_{coil} \tag{A.7}$$

where e_{coil} is the unit vector in direction of current flow.

APPENDIX B

ACTIVATING FUNCTION AND SPATIAL VARIANCE OF ELECTRIC FIELDS

The Activating Function as introduced and advocated by F. Rattay provides an efficient tool for determining stimulation efficacy without delving into neural modelling. The AF for an external electrical stimulation is given by:

$$A(x) = \frac{\partial^2 V_e}{\partial x^2} \tag{B.1}$$

Here V_e is the external stimulation potential. The derivation of this function can be found in several references [refs]. This function is based on several simplifications. One of them is cylindrical symmetry of the electrode, thereby simplifying the analysis by neglecting the transverse fields. As E = -V, A(x) may also be written in terms of E:

$$A(x) = -\frac{\partial E}{\partial x} \tag{B.2}$$

An important point to note is the right hand side of B.1 and B.2 are opposite in sign. Thus, while maxima in B.1 denotes peak depolarization, maxima in B.2 denotes peak hyperpolarization, unless the sign is accounted for while modeling [39]. In this thesis we have applied the Activating Function to more accurately examine the extent and effect of magnetic excitation and compare it with electrical stimulation. The AF relates to the membrane potential as follows [ref]:

$$r_i \frac{\partial v_m}{\partial t} = \frac{1}{c_m}\left(-i_{ion} r_i + \frac{\partial^2 v_m}{\partial x^2} + \frac{\partial^2 V_e}{\partial x^2}\right) \tag{B.3}$$

Here cm is the membrane capacitance per unit length ($\mu F/cm$), v_m is the transmembrane voltage (mV), i_{ion} is the ionic current flowing across the membrane ($\mu A/cm^2$), r_i is the internal membrane resistance times unit length (Ωcm) and x is the distance along the axon

(cm) [40]. While solving the above equation can be complicated, under sub threshold conditions v_m is equal to zero, so the second derivative of v_m and i_ion are also zero leaving behind the AF multiplied by $\frac{1}{cm}$. Therefore, plotting the solution for AF provides information about which regions are more likely to be excited than others. This is due to positive values of the AF corresponding to positive values of $\frac{\partial v_m}{\partial t}$, which represent the region that will depolarize. This is shown in preliminary work.

APPENDIX C

CARING FOR PLATED NEURONS ON A MULTIELECTRODE ARRAY

Instructions for media flushes and media change are as follows:

- Take Jimbos[1] media out of the fridge and leave it in the water bath for 10 minutes, so that it is at room temperature during media flushes.
- Put on gloves and sleeves, turn off UV light, open the fume-hood.
- Wipe down the area of the fume-hood that would be used for media changes with ethanol.
- Sterilize a waste beaker using ethanol and place it in the fume-hood for collecting used pipettes and flushed out media.
- Unscrew the lid of the centrifuge tube containing the media, but leave it on.
- Ensure sufficient number of 1 mL pipettes are present in the fume-hood before bringing the MEA with cells in there. Make sure everything is you need is within reach.
- Once the MEA is in the fume-hood, flush out the potentially contaminated media using a 1 mL pipette tip and carefully replace it with new media. The flow of media from the pipette should be drop-by-drop, not as a continuous stream. This ensures minimal damage to the plated cells.
- Dispose off the pipette tip.

[1]"Cortical tissue was taken from E17-18 Wistar rat embryos and dissociated by trituration after digestion with 0.02% papain (Boehringer). Cells were plated on laminin and poly-D-lysine-coated (Sigma) electrode array substrates. The culture medium consisted of Dulbeccos modified Eagles medium (DMEM) (Gibco) containing 5% FBS (Hy-clone), 5% heat-inactivated horse serum (Gibco), 2.5 μg/ml insulin (Sigma), and penicillin/ streptomycin (540 U/ml; Sigma), conditioned overnight in glial cell cultures (Baughman et al., 1991)." [92].

- After the first flush, wipe off the MEA surface outside the well, and even the outside and top of the well with ethanol, to minimize risk of infection.
- Repeat the media flushes three times then place an autoclaved Teflon cap on top of the MEA well.
- Place this covered MEA in a sterilized petri-dish and place it back in the incubator.
- Place the remaining Jimbos media back in the fridge, throw away the used petri-dish and pipette tips in the biohazard trash, and clean the waste beaker.
- Wipe down the fume-hood with ethanol, close the window and switch on the UV light.

APPENDIX D

DETAILED INSTRUCTIONS FOR PARYLENE COATING

The hot glue used in the first version of the stimulator had the disadvantage of being viscous and bulky. It was difficult to precisely control the thickness of the layer of glue and this was a problem because the induced fields vary with distance from a surface. So, as an alternative, NuSil med-2000 polymer was used in conjunction with a pneumatic pump and Madell digitally controlled pneumatic dispensing system to provide a more controlled layer of insulation. While the thickness of the polymer could roughly be controlled using a constant pressure of 30 psi, the coating was not uniform as it depended on the user's control on the apparatus to precisely apply the coat of polymer. So, an SCS parylene coater was used to add a conformal layer of the bio-compatible polymer, Parylene-C, on top the entire assembly of stimulator. As the final set of experiments may potentially compromise the sterility of the dissociated cultures by removing the Teflon cap from the MEA well and inserting the stimulator in the media, the aspect of bio-compatibility is important.

D.1 Introduction

The Labcoter PDS 2010 is a vacuum system used for vapor deposition of Parylene. The Parylene is initially in the form of a solid dimer. At temperatures above 80°C the dimer parylene becomes dimer parylene gas. This occurs inside the Vaporizer. In the Furnace, at 690°C, the dimer is decomposed to monomer gas. In this state it enters the chamber and is deposited on the substrate as a polymer. The deposition occurs at room temperature in vacuum. Parylene will stick to any surface at temperatures below 80°C and is difficult to remove. For this reason, we treat the interior of the chamber with 2% Microsolution and the pressure sensor is heated to 140°C. The cold trap is to prevent excess parylene and by-products from reaching the vacuum pump. The cold trap is held at temperatures below

-80°C, attracting most parylene particles that pass on its way from the chamber towards the vacuum pump. The parylene-C deposition rate is approximately 5um/hr at the default recipe pressure of 35.

The steps involved in coating the stimulator assembly are as follows:

1. Cover the parts of the assembly that need to electrically conducting after the coating process with tape.
2. Take off the cover of the coating chamber and place the parts to be coated inside it.
3. Spray the cover of the coating chamber and the cooling thimble with a thin layer of 2 % microsolution.
4. Start of the cooler and wait for the temperature to reach -90 ∘C before switching the system on.
5. Measure the amount of parylene-C required based on the desired thickness of the coat (8 grams for a 5 μm thick layer, figure D.1).
6. Put the Parylene-C in the heating chamber and close the chamber.
7. The default setting of the machine is set to work with Parylene-C (see table), so switch on the machine and wait till the green light at the Start/Stop button starts flickering.
8. Once finished, take the parts out and clean up after yourself.

The following sections provide the steps for using the spin-coater in details.

D.2 Precautions

The chamber base, inlet, and vaporizer reach high temperatures. Be careful.

Although parylene is considered non-toxic, parylene vapor does contain small amounts of corrosive and possibly harmful gases. Therefore, do not breathe it.

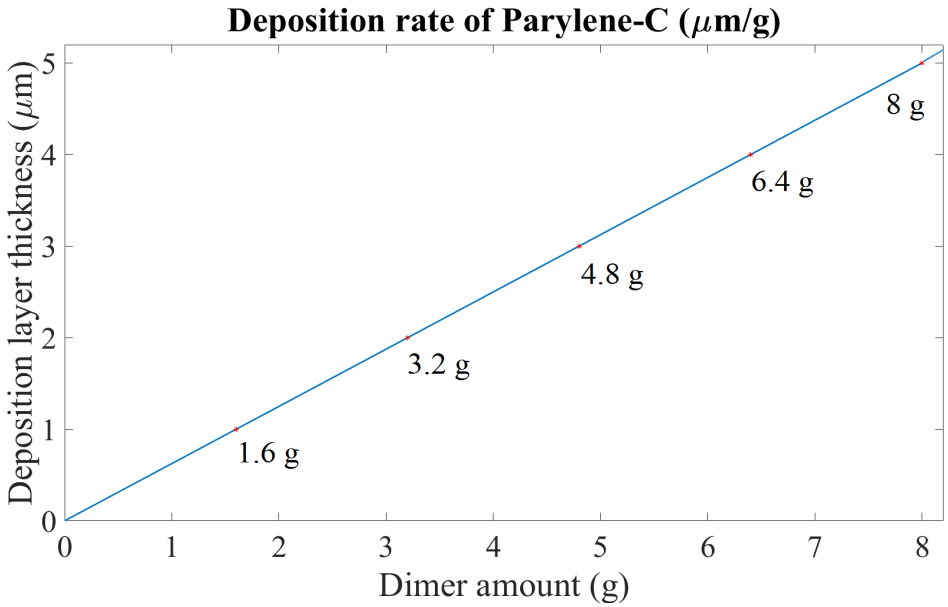

Figure D.1: Chart showing weight of parylene-C dimer in grams plotted against the thickness of the desired layer in micrometer.

D.3 Pre-Operation

Fill out log sheet.

D.3.1 Boat construction

Cut an aluminum sheet of approximately 10” by 4” Fold in the ends of the foil. (Reuse the foil until the dark residue becomes thick.)

D.3.2 System preparation

Place the parylene loaded boat inside the vaporizer (measure mass based off of thickness Disengage red Emergency Off button by turning. Press Main Power button on top left corner. Any surface that needs to be stripped of Parylene must be treated with supplied release solution (2% Micro-clean). The surfaces that can be cleaned and treated are:

Chamber lid Cold trap thimble and housing Note: DO NOT pull the parylene off of the chamber walls. Any loose parylene that can be removed near the chamber o-ring may be removed as long as you do not pull parylene off of the chamber wall.

Make sure o-rings, gasket, and the surfaces which they will contact are clean (use IPA). Chamber lid Cold trap inlet Vaporizer door Insert cold trap thimble into the PDS.

D.4 Operation

D.4.1 Start Up

Verify the set-point values (deposition pressure, furnace temp, and vaporizer temp). Turn vacuum knob to VACUUM while holding the cold trap in place. When the chamber pumps down to 100, start the Mechanical Chiller. When the pressure reaches 5 enable the Furnace and Vaporizer knob. Press Process Start/Stop button. First, the vacuum gauge will be heated up to 135°C to prevent any parylene deposition on the vacuum gauge that measures the pressure inside the chamber. Then, the furnace is heated up to 690°C.

D.4.2 Post-Operation

When Start/Stop button is blinking or pressure reading is below 10. Depress the Start/Stop button. Disable the Furnace and Vaporizer switches. Turn off cold-trap compressor. Turn the vacuum knob to VENT. Wait for cold-trap to warm up to above -40°C. Remove cold-trap and clean off all parylene deposition. Please wear gloves and use a razor blade, and vacuum cleaner. Be careful to not twist or bend the chiller hose at a tight radius as it will cause damage. Wait until cold-trap rises to above -40°C before handling.

Unload the chamber. Peel off the parylene from the chamber lid and wipe chamber lid with micro clean solution (use very little solution so it will not outgas for the next user). Replace the lid on the chamber. Note: You must clean up all of the parts stated in post operation as well as any parylene you may have spilled at the station. Failure to do so will result in suspension.

Turn off the Main Power by pressing the Emergency Off (EMO) button. If you would like to do another run you must wait until the cold-trap returns to room temperature (>20°C) to avoid condensation.

APPENDIX E

MATLAB CODES

E.1 Code for cleaning up data and calculating firing rate

```
%% Load raw and eliminate grounded channels
fn = '';
raw = loadraw(['G:\Sagarika_data\06142018\' fn '.raw']);
vrms = std(raw,[],2);
plot(vrms,'*')
th = 1e-5; % adjust this value based on the vrms values calculated
f_rep = 2; % repetition frequency in Hz
good_channels = (vrms > th);
I = (1:64)';
I1 = I.*good_channels;
I1 = I1(I1 ~=0);
raw = raw(I1,:);
fs = 25000;
[nc, ns] = size(raw);
t = (1:ns)/fs;
```

```
%% Removing stimulation artifacts
dur = (i2.Position(1) - i1.Position(1))*1000;
first_sample = (i1.Position(1)*fs)-13;
interstim_time = (1/f_rep)*1000;
rawCleaned = stim_art_removal(raw, dur, 4e-5, interstim_time);
% rawCleaned = stim_art_removal1(raw, dur, first_sample, interstim_time);
rw = raw;
raw = rawCleaned.raw;
```

```
%% Test how well stim art removal worked
plot(t,raw(22,:))
in = t>105&t<130;
raw_in = raw([17,24],:);
spkdat1 = raw2spikes(raw_in, 7);% if no spikes are seen in the region where
%no spikes are present, proceed further, else run line 17 again
%with modified parameters
```

```
%% Detect all spikes and bin them in 1-second bins
spkdat = raw2spikes(raw, 7);
[S, I] = sort(spkdat.time,'ascend');
N = hist(S/fs,0.5:(ceil((ns/fs))-0.5));
```

E.2 Code for stimulation artifact removal

```
function rawCleaned = stim_art_removal(raw, dur, threshold)
% raw is the raw file
% dur is the duration of the stimulus in ms; the function takes care of
%any other delays or viariation in stim artifact. Duration is 400 us for a
%200us per phase biphasic pulse or 11ms for a 9 khz 10 cycles of sine wave
% threshold is the minimum value that only the direct stim artifact can
% reach and the neural activity cannot achieve that value. 5e-4 is a good
% example of a threshold value irrespsctive of the stimulation type.
% interstim_time will determine the allowable window for observing neural
% activity. For example, if stimulation is provided at 10 Hz, then the
% maximum window for observing neural activity is 100 ms.

[nc,ns] = size(raw);
rw = raw;
if nargin~=4
    error('not enough input arguments');
end
dur = dur*25;
crossings = find((rw(:,1:(ns-1))<threshold)&(rw(:,2:ns)>=threshold));
[c,t] = ind2sub([nc,ns],crossings);
rawCleaned.time = t;
rawCleaned.channel = c;
ll = length(t);
cleanedSample = -13:dur+25;
all_samples = cleanedSample + t;
for ii = 1:ll
rw(c(ii),all_samples(ii,:)) = 0;
end
rawCleaned.raw = rw;
```

APPENDIX F

MEA ELECTRODE MAP

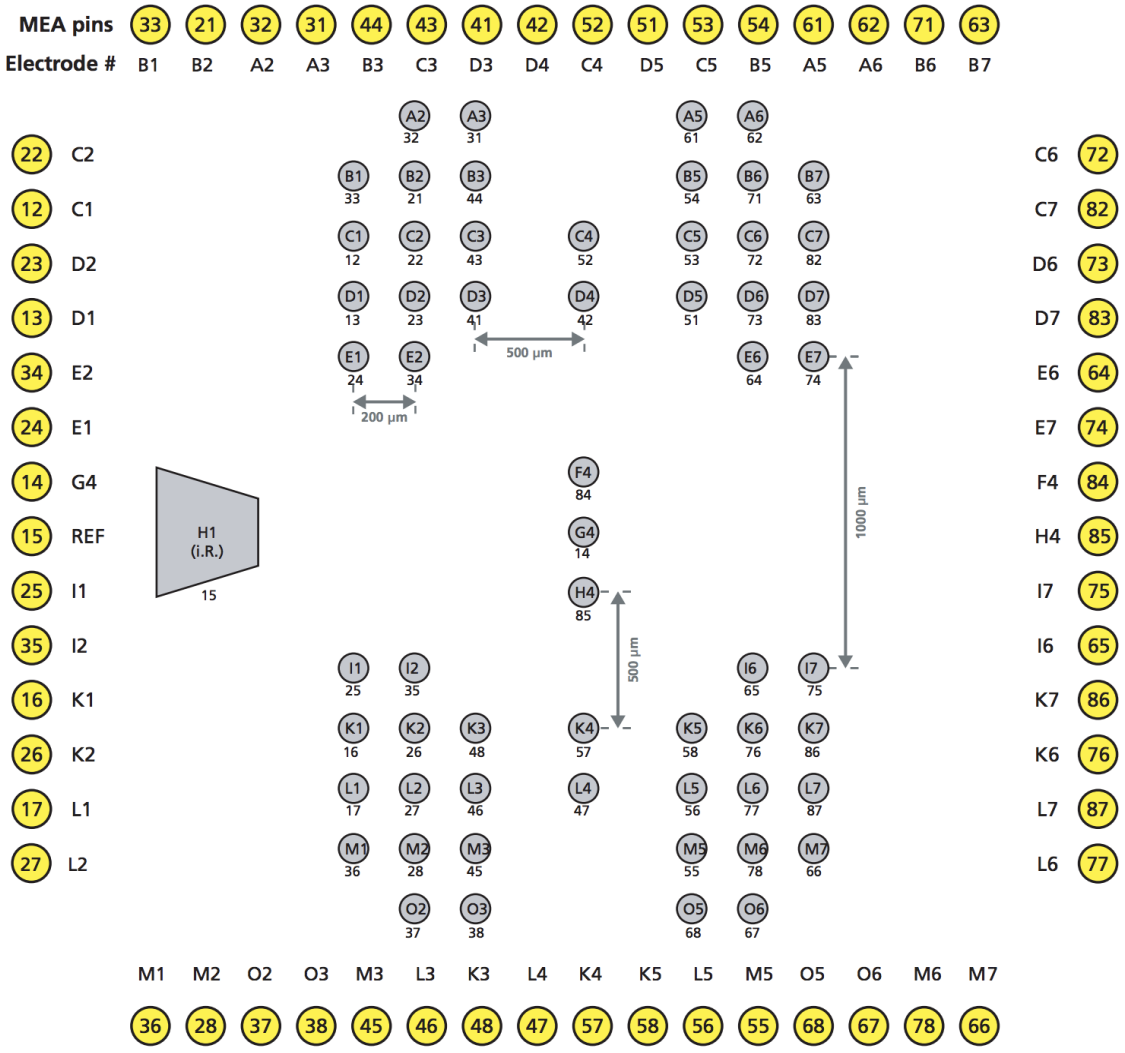

Figure F.1: MEA electrodes mapped on to the MCS amplifier channels (courtesy: Multi-channel Systems MCS GmbH)

REFERENCES

[1] B. S. Wilson, "Cochlear implants: Current designs and future possibilities," *The Journal of Rehabilitation Research and Development*, vol. 45, no. 5, pp. 695–730, 2008.

[2] F.-g. Zeng, Q. Tang, and T. Lu, "Abnormal Pitch Perception Produced by Cochlear Implant Stimulation," vol. 9, no. 2, 2014.

[3] *The national institute on deafness and other communication disorders statistics*, `https://www.nidcd.nih.gov/health/statistics/quick-statistics-hearing`.

[4] D. E. Brackmann, "The cochlear implant: Basic principles," *The Laryngoscope*, 1975.

[5] D. Wang, "Deep learning reinvents the hearing aid," *Phys. Rev.*, Dec. 2016.

[6] J. Swaminathan, R. L. Goldsworthy, P. M. Zurek, A. C. Lger, and L. D. Braida, "Preliminary evaluation of a physiologically inspired signal processing strategy for cochlear implants," *The Journal of the Acoustical Society of America*, vol. 135, no. 4, pp. 2410–2410, 2014.

[7] K. Chung and F.-G. Zeng, "Enhancing cochlear implants with hearing aid signal processing technologies.," pat. 8 942 815, Jan. 2015.

[8] N. Iglesias, J. M. Juarez, M. Campos, and F. Palacios, "Artificial computation in biology and medicine.," *Lecture Notes in Computer Science (including subseries Lecture Notes in Artificial Intelligence and Lecture Notes in Bioinformatics)*, vol. 9107, 2015.

[9] W. Ngamkham, M. N. van Dongen, J. J. Briaire, and J. H. M. Frijns, "A 0.042 mm∧2 programmable biphasic stimulator for cochlear implants suitable for a large number of channels," *Phys. Rev.*, vol. 13, 2015.

[10] K. Kolb, "Evaluation of multiple speech processing combinations in the Cochlear Nucleus 5 cochlear implant system using R-Space simulation," *Independent Studies and Capstones*, 2011.

[11] J. J. M. Monaghan, T. Goehring, X. Yang, F. Bolner, S. Wang, M. C. M. Wright, and S. Bleeck, "Auditory inspired machine learning techniques can improve speech

intelligibility and quality for hearing-impaired listenersa)," *The Journal of the Acoustical Society of America*, vol. 141, no. 3, pp. 1985–1998, 2017.

[12] G. M. Clark and R. J. Hallworth, "A multiple-electrode array for a cochlear implant," *The Journal of Laryngology and Otology*, vol. 90, pp. 623–627, 07 Jul. 1976.

[13] M. M. Merzenich, M. White, M. C. Vivion, P. A. Leake-jones, and S. Walsh, "Some considerations of multichannel electrical stimulation of the auditory nerve in the profoundly deaf; interfacing electrode arrays with the auditory nerve array," *Acta Oto-Laryngologica*, vol. 87, no. 3-6, pp. 196–203, 1979.

[14] L. Yong-xin, L. Shuang, and H. De-min, "Research Advances in Post-Operative Rehabilitation Following Cochlear Implant," *Journal of Otology*, vol. 2, no. 2, pp. 92–96, 2007.

[15] M. Seyyedi and J. B. Nadol, "Intracochlear inflammatory response to cochlear implant electrodes in humans.," *Otology & neurotology : official publication of the American Otological Society, American Neurotology Society [and] European Academy of Otology and Neurotology*, vol. 35, no. 9, pp. 1545–51, 2014.

[16] V. S. Polikov, P. A. Tresco, and W. M. Reichert, "Response of brain tissue to chronically implanted neural electrodes," *Journal of Neuroscience Methods*, vol. 148, no. 1, pp. 1–18, 2005.

[17] F.-G. Zeng, "Trends In Cochlear Implants," vol. 8, no. 1, pp. 1–34, 2004.

[18] N. R. Capretta and A. C. Moberly, "Does quality of life depend on speech recognition performance for adult cochlear implant users?" *Laryngoscope*, vol. 126, no. 3, pp. 699–706, 2016.

[19] L. Garcia, I. Zuriñe, M. Ane, U. Mercedes, and F. Xabier, "Cochlear implantation in the elderly : outcomes , long-term evolution , and predictive factors," *European Archives of Oto-Rhino-Laryngology*, vol. 0, no. 0, p. 0, 2018.

[20] B. H. Bonham and L. M. Litvak, "Current focusing and steering: Modeling, physiology, and psychophysics," *Hearing Research*, vol. 242, no. 1-2, pp. 141–153, Aug. 2008.

[21] J. D. Falcone and P. T. Bhatti, "Current steering and current focusing with a high-density intracochlear electrode array," *Proceedings of the Annual International Conference of the IEEE Engineering in Medicine and Biology Society, EMBS*, pp. 1049–1052, 2011.

[22] R. K. Kalkman, J. J. Briaire, and J. H. M. Frijns, "Current focussing in cochlear implants: An analysis of neural recruitment in a computational model," *Hearing Research*, vol. 322, pp. 89–98, 2014.

[23] P. T. Bhatti and K. D. Wise, "A 32-site 4-channel high-density electrode array for a cochlear prosthesis," *IEEE Journal of Solid-State Circuits*, vol. 41, no. 12, pp. 2965–2973, 2006.

[24] K. S. Min, S. B. Jun, Y. S. Lim, S. I. Park, and S. J. Kim, "Modiolus-hugging intracochlear electrode array with shape memory alloy," *Computational and Mathematical Methods in Medicine*, vol. 2013, 2013.

[25] M. F. Dorman and R. H. Gifford, "Combining acoustic and electric stimulation in the service of speech recognition.," *International journal of audiology*, vol. 49, no. 12, pp. 912–919, 2010.

[26] T. Rader, Y. Adel, H. Fastl, and U. Baumann, "Speech Perception with Combined Electric-Acoustic Stimulation: A Simulation and Model Comparison," *Ear and Hearing*, vol. 36, no. 6, e314–e325, 2015.

[27] R. T. Richardson, A. C. Thompson, A. K. Wise, and K. Needham, "Challenges for the application of optical stimulation in the cochlea for the study and treatment of hearing loss," *Expert Opinion on Biological Therapy*, vol. 17, no. 2, pp. 213–223, 2017, PMID: 27960585.

[28] C. Wrobel, A. Dieter, A. Huet, D. Keppeler, C. J. Duque-Afonso, C. Vogl, G. Hoch, M. Jeschke, and T. Moser, "Optogenetic stimulation of cochlear neurons activates the auditory pathway and restores auditory-driven behavior in deaf adult gerbils," *Science Translational Medicine*, vol. 10, no. 449, 2018.

[29] J. Wang, L. Tian, J. Lu, M. Xia, and Y. Wei, "Effect of shorter pulse duration in cochlear neural activation with an 810-nm near-infrared laser," pp. 389–396, 2017.

[30] M. P. Sato, T. Higuchi, F. Nin, G. Ogata, S. Sawamura, T. Yoshida, T. Ota, K. Hori, S. Komune, S. Uetsuka, S. Choi, M. Masuda, T. Watabe, S. Kanzaki, K. Ogawa, H. Inohara, S. Sakamoto, H. Takebayashi, K. Doi, K. F. Tanaka, and H. Hibino, "Hearing Loss Controlled by Optogenetic Stimulation of Nonexcitable Nonglial Cells in the Cochlea of the Inner Ear," *Frontiers in Molecular Neuroscience*, vol. 10, no. September, pp. 1–16, 2017.

[31] L. Tian, J. Wang, Y. Wei, J. Lu, A. Xu, and M. Xia, "Short-wavelength infrared laser activates the auditory neurons : comparing the effect of 980 vs . 810 nm wavelength," pp. 357–362, 2017.

[32] V. Lumbreras, E. Bas, C. Gupta, and S. M. Rajguru, "Pulsed infrared radiation excites cultured neonatal spiral and vestibular ganglion neurons by modulating mitochondrial calcium cycling Pulsed infrared radiation excites cultured neonatal spiral and vestibular ganglion neurons by modulating mitochondrial c," no. June, pp. 1246–1255, 2014.

[33] T. Moser, "Optogenetic stimulation of the auditory pathway for research and future prosthetics," *Current Opinion in Neurobiology*, vol. 34, pp. 29–36, 2015.

[34] V. Goyal, S. Rajguru, A. I. Matic, S. R. Stock, and C.-P. Richter, "Acute damage threshold for infrared neural stimulation of the cochlea: Functional and histological evaluation.," *Anatomical record (Hoboken, N.J. : 2007)*, vol. 295, no. 11, pp. 1987–99, Nov. 2012.

[35] V. H. Hernandez, A. Gehrt, K. Reuter, Z. Jing, M. Jeschke, A. M. Schulz, G. Hoch, M. Bartels, G. Vogt, C. W. Garnham, H. Yawo, Y. Fukazawa, G. J. Augustine, and E. Bamberg, "Technical advance Optogenetic stimulation of the auditory pathway," vol. 124, no. 3, 2014.

[36] R. D. U. Plonsey and R. C.D. U. Barr, *Bioelectricity A Quantitave Approach*. 2007, p. 531, ISBN: 9780387488646.

[37] *Action potential depiction*, `http://www.vce.bioninja.com.au`.

[38] J. Boulet, M. White, and I. C. Bruce, "Temporal Considerations for Stimulating Spiral Ganglion Neurons with Cochlear Implants," *JARO - Journal of the Association for Research in Otolaryngology*, vol. 17, no. 1, pp. 1–17, 2016.

[39] W. Wang and S. R. Eisenberg, "A three-dimensional finite element method for computing magnetically induced currents in tissues," *IEEE Transactions on Magnetics*, vol. 30, no. 6, 1994.

[40] S. S. Nagarajan, D. M. Durand, and E. N. Warman, "Effects of induced electric fields on finite neuronal structures: a stimulation study," *IEEE Trans. Biomed. Eng.*, vol. 40, no. 92, pp. 1175–1188, 1993.

[41] S. S. Nagarajan and D. M. Durand, "A generalized cable equation for magnetic stimulation of axons," *IEEE Transactions on Biomedical Engineering*, vol. 43, no. 3, pp. 304–312, 1996.

[42] F. Rattay, "Analysis of Models for External Stimulation of Axons," *IEEE Transactions on Biomedical Engineering*, vol. BME-33, no. 10, pp. 974–977, 1986.

[43] P. J. Basser and B. J. Roth, "Stimulation of a myelinated nerve axon by electromagnetic induction," *Medical & Biological Engineering & Computing*, vol. 29, no. 3, pp. 261–268, 1991.

[44] F. Rattay, "Analysis of Models for Extracellular Fiber Stimulation," *IEEE Transactions on Biomedical Engineering*, vol. 36, no. 7, pp. 676–682, 1989.

[45] C. T. Jr., P. A. Springer, G. E. Loeb, Y. Berwald-Netter, and L. M. Okun, "A miniature microelectrode array to monitor the bioelectric activity of cultured cells," *Experimental Cell Research*, vol. 74, pp. 61–66, 1 1972.

[46] B Eversmann, M Jenkner, F Hofmann, C Paulus, R Brederlow, B Holzapfl, P Fromherz, M Merz, M Brenner, M Schreiter, R Gabl, K Plehnert, M Steinhauser, G Eckstein, D Schmitt-Landsiedel, and R Thewes, "A 128 x 128 CMOS Biosensor Array for Extracellular\rRecording of Neural Activity," *Ieee Journal of Solid-State Circuits,*, vol. 38, no. 12, pp. 2306–2317, 2003.

[47] C. M. Hales, R. Zeller-Townson, J. P. Newman, J. T. Shoemaker, N. J. Killian, and S. M. Potter, "Stimulus-evoked high frequency oscillations are present in neuronal networks on microelectrode arrays," *Frontiers in Neural Circuits*, vol. 6, no. May, pp. 1–10, 2012.

[48] D. A. Wagenaar, "Controlling Bursting in Cortical Cultures with Closed-Loop Multi-Electrode Stimulation," *Journal of Neuroscience*, vol. 25, no. 3, pp. 680–688, 2005.

[49] D. A. Wagenaar, J. Pine, and S. M. Potter, "An extremely rich repertoire of bursting patterns during the development of cortical cultures," *BMC Neuroscience*, vol. 7, pp. 1–18, 2006.

[50] S. Hahnewald, A. Tscherter, E. Marconi, J. Streit, H. R. Widmer, C. Garnham, H. Benav, M. Mueller, H. Löwenheim, M. Roccio, and P. Senn, "Response profiles of murine spiral ganglion neurons on multi-electrode arrays," *Journal of Neural Engineering*, vol. 13, no. 1, p. 016 011, Feb. 2016.

[51] E. B. Montgomery and J. T. Gale, "Mechanisms of action of deep brain stimulation (DBS)," *Neuroscience and Biobehavioral Reviews*, vol. 32, no. 3, pp. 388–407, 2008.

[52] J. P. Lefaucheur, X Drouot, and J. P. Nguyen, "Interventional neurophysiology for pain control: duration of pain relief following repetitive transcranial magnetic stimulation of the motor cortex 124," *Neurophysiol.Clin.*, vol. 31, no. 0987-7053 (Print), pp. 247–252, 2001.

[53] A. Pascual-Leone, "Transcranial magnetic stimulation and the human brain.," *Nature*, vol. 406, no. 6792, pp. 147–150, 2000.

[54] G. L. Bagnato, G. Miceli, N. Marino, D. Sciortino, and G. F. Bagnato, "Pulsed electromagnetic fields in knee osteoarthritis: a double blind, placebo-controlled, randomized clinical trial.," *Rheumatology (Oxford, England)*, vol. 55, no. 4, pp. 755–62, 2016.

[55] T. Kammer, S. Beck, A. Thielscher, U. Laubis-herrmann, and H. Topka, "Motor thresholds in humans : a transcranial magnetic stimulation study comparing different pulse waveforms , current directions and stimulator types," vol. 112, pp. 250–258, 2001.

[56] FDA, "Guidance for Industry and Food and Drug Administration Staff Class II Special Controls Guidance Document: Electrocardiograph Electrodes," pp. 1–15, 2011.

[57] P. Rastogi, E. G. Lee, R. L. Hadimani, and D. C. Jiles, "Transcranial Magnetic Stimulation-coil design with improved focality," *AIP Advances*, vol. 7, no. 5, 2017.

[58] J. Ruohonen, J Virtanen, and R. J. Ilmoniemi, "Coil optimization for magnetic brain stimulation.," *Annals of biomedical engineering*, vol. 25, no. 5, pp. 840–849, 1997.

[59] Z. D. Deng, S. H. Lisanby, and A. V. Peterchev, "Coil design considerations for deep transcranial magnetic stimulation," *Clinical Neurophysiology*, vol. 125, no. 6, pp. 1202–1212, 2014.

[60] E. M. Wassermann and T. Zimmermann, "Transcranial magnetic brain stimulation: Therapeutic promises and scientific gaps," *Pharmacology and Therapeutics*, vol. 133, no. 1, pp. 98–107, 2012. eprint: NIHMS150003.

[61] H. Tischler, S. Wolfus, A. Friedman, E. Perel, T. Pashut, M. Lavidor, A. Korngreen, Y. Yeshurun, and I. Bar-Gad, "Mini-coil for magnetic stimulation in the behaving primate," *Journal of Neuroscience Methods*, vol. 194, no. 2, pp. 242–251, 2011.

[62] G. Bonmassar, S. W. Lee, D. K. Freeman, M. Polasek, S. I. Fried, and J. T. Gale, "Microscopic magnetic stimulation of neural tissue," *Nature Communications*, vol. 3, no. May, p. 921, 2012.

[63] H.-J. Park, G. Bonmassar, J. Kaltenbach, A. G. Machado, N. F. Manzoor, and J. T. Gale, "Activation of the central nervous system induced by micro-magnetic stimulation," *Nature communications*, vol. 4, p. 2463, 2013.

[64] S. Minusa, H. Osanai, and T. Tateno, "Micromagnetic Stimulation of the Mouse Auditory Cortex In Vivo Using an Implantable Solenoid System," *IEEE Transactions on Biomedical Engineering*, vol. 65, no. 6, pp. 1301–1310, 2017.

[65] S. W. Lee and S. I. Fried, "Suppression of Subthalamic Nucleus Activity by Micromagnetic Stimulation," *Neural Systems and Rehabilitation Engineering, IEEE Transactions on*, vol. 23, no. 1, pp. 116–127, 2015.

[66] S. W. Lee, F. Fallegger, B. D. F. Casse, and S. I. Fried, "Implantable microcoils for intracortical magnetic stimulation," no. December, 2016.

[67] S. W. Lee and S. I. Fried, "Enhanced Control of Cortical Pyramidal Neurons with Micromagnetic Stimulation," *IEEE Transactions on Neural Systems and Rehabilitation Engineering*, vol. 25, no. 9, pp. 1375–1386, 2017.

[68] D Blake, P. T. Bhatti, J. V. Beek-King, J. Crawford, and B. McKinnon, "Micro magnetic stimulation of the feline cochlea," *13th International Conference on Cochlear Implants and Other Implantable Auditory Technologies*, S4–8, 2014.

[69] F.-G. Zeng, S. Rebscher, W. V. Harrison, X. Sun, and H. Feng, "Cochlear Implants:System Design, Integration and Evaluation," *IEEE reviews in biomedical engineering*, vol. 1, 2008.

[70] B. Wang, W. M. Grill, and A. V. Peterchev, "Coupling magnetically induced electric fields to neurons: longitudinal and transverse activation," *bioRxiv*, vol. 115, no. 1, p. 275 073, 2018.

[71] M. F. Dempsey and B. Condon, "Thermal injuries associated with MRI," *Clinical Radiology*, vol. 56, no. 6, pp. 457–465, 2001.

[72] C. C. Della Santina, A. A. Migliaccio, and A. H. Patel, "A multichannel semicircular canal neural prosthesis using electrical stimulation to restore 3-D vestibular sensation," *IEEE Transactions on Biomedical Engineering*, vol. 54, no. 6, pp. 1016–1030, 2007.

[73] A. V. Peterchev, R. Jalinous, and S. H. Lisanby, "A Novel Transcranial Magnetic Stimulator Inducing Near Rectangular Pulses with Controllable Pulse Width (cTMS)," *IEEE transactions on bio-medical engineering*, vol. 55, 2008.

[74] D. Andreuccetti, R. Fossi, and C. Petrucci, "An internet resource for the calculation of the dielectric properties of body tissues in the frequency range 10 hz - 100 ghz," *IFAC-CNR, Florence (Italy)*, 1997.

[75] C. Gabriel, "Compilation of the dielectric properties of body tissues at rf and microwave frequencies," *Report N.AL/OE-TR- 1996-0037, Occupational and envi-*

ronmental health directorate, Radiofrequency Radiation Division, Brooks Air Force Base, Texas (USA), 1996.

[76] C. Gabriel, S. Gabriel, and E. Corthout, "The dielectric properties of biological tissues: I. literature survey," *Phys. Med. Biol.*, vol. 41, pp. 2231–2249, 1996.

[77] S. B. Baumann, D. R. Wozny, S. K. Kelly, and F. M. Meno, "The electrical conductivity of human cerebrospinal fluid at body temperature," *IEEE Transactions on Biomedical Engineering*, vol. 44, no. 3, pp. 220–225, 1997.

[78] P. H. Mason, W. Walters, T. D'Andrea, P. R. J. Gajsek, K.L.Nelson, D. Smith, K.I., and J. Ziriax, "Effects of frequency, permittivity, and voxel size on predicted specific absorption rate values in biological tissue during electromagnetic-field exposure," *IEEE Transactions on Microwave Theory and Techniques*, vol. 48, no. 11, pp. 2050–2058, 2000.

[79] T. Wu, T. S. Rappaport, and C. M. Collins, "The Human Body and Millimeter - Wave Wireless Communication Systems : Interactions and Implications," *2015 IEEE International Conference on Communications (ICC), Jun. 2015*, vol. 200, no. Icc, pp. 4026–4032, 2015.

[80] C. Y. Chan, J Hounsgaard, and C Nicholson, "Effects of electric fields on transmembrane potential and excitability of turtle cerebellar Purkinje cells in vitro.," *The Journal of physiology*, vol. 402, pp. 751–71, 1988.

[81] E. Erixon, H. Ho, K. Wadin, and H. Rask-andersen, "Variational Anatomy of the Human Cochlea : Implications for Cochlear Implantation," pp. 14–22, 2008.

[82] P Bhatti, A Sharpe, J Crawford, S Tridandapani, B Mckinnon, and D Blake, "Highly flexible silicone coated neural array for intracochlear electrical stimulation," *BioMed Research International*, vol. 2015, pp. 1–11, Jan. 2015.

[83] S. W. Lee and S. I. Fried, "The response of L5 pyramidal neurons of the PFC to magnetic stimulation from a micro-coil," *2014 36th Annual International Conference of the IEEE Engineering in Medicine and Biology Society, EMBC 2014*, no. 617, pp. 6125–6128, 2014. eprint: 15334406.

[84] G. Bonmassar and L. Golestanirad, "EM fields comparison between planar vs. solenoidal μmS coil designs for nerve stimulation," *Proceedings of the Annual International Conference of the IEEE Engineering in Medicine and Biology Society, EMBS*, pp. 3576–3579, 2017.

[85] R Guttman and R Barnhill, "Oscillation and repetitive firing in squid axons. Comparison of experiments with computations.," *The Journal of general physiology*, vol. 55, no. 1, pp. 104–118, 1970.

[86] H. Toreyin and P. Bhatti, "A field-programmable analog array development platform for vestibular prosthesis signal processing," *IEEE Transactions on Biomedical Circuits and Systems*, vol. 7, no. 3, pp. 319–325, 2013.

[87] N. J. Tachas and T. Samaras, "The effect of head and coil modeling for the calculation of induced electric field during transcranial magnetic stimulation," *International Journal of Psychophysiology*, vol. 93, no. 1, pp. 167–171, 2014.

[88] N. S. Davidovics, M. A. Rahman, C. Dai, J. Ahn, G. Y. Fridman, and C. C. Della Santina, "Research Article," vol. 248, pp. 233–248, 2013.

[89] N. Jonathan, Z.-T. Riley, F. Ming-fai, A. D. Sharanya, G. Robert, and P. Steve, "Closed-loop, multichannel experimentation using the open-source neurorighter electrophysiology platform," *Frontiers in Neural Circuits*, vol. 6, p. 98, Jan. 2013.

[90] D. Wagenaar and S. Potter, "A versatile all-channel stimulator for electrode arrays, with real-time control," *J. Neural Eng.*, vol. 1, no. 1, pp. 39–45, 2004.

[91] C. M. Hales, J. D. Rolston, and S. M. Potter, "How to culture, record and stimulate neuronal networks on micro-electrode arrays (meas)," *Journal of Visualized Experiments: JoVE*, vol. 39, 2056 2010.

[92] Y. Jimbo, T. Tateno, and H. Robinson, "Simultaneous induction of pathway-specific potentiation and depression in networks of cortical neurons," *Biophysical Journal*, vol. 76, 670678, 2 Feb. 1999.

[93] D. A. Wagenaar and S. M. Potter, "Real-time multi-channel stimulus artifact suppression by local curve fitting," *Journal of Neuroscience Methods*, vol. 120, no. 2, pp. 113–120, 2002. arXiv: `1204.3968`.

[94] *Squeakyspk for signal processing*, `http://code.google.com/p/squeakyspk/`.

[95] R. Feynman, R. Leighton, and M. Sands, *Feynman lectures on physics. Vol. 2, Mainly electromagnetism and matter*. AAPT, 1965, vol. 33, p. 536.

[96] C. D. Gerardo, E. Cretu, and R. Rohling, "Fabrication of circuits on flexible substrates using conductive SU-8 for sensing applications," *Sensors (Switzerland)*, vol. 17, no. 6, pp. 1–15, 2017.

[97] C. Weller, R. Kleer, and F. T. Piller, "Economic implications of 3D printing: Market structure models in light of additive manufacturing revisited," *International Journal of Production Economics*, vol. 164, pp. 43–56, 2015.

[98] M. Singh, H. M. Haverinen, P. Dhagat, and G. E. Jabbour, "Inkjet printing-process and its applications," *Advanced Materials*, vol. 22, no. 6, pp. 673–685, 2010.

[99] B. Bhushan and M. Caspers, "An overview of additive manufacturing (3D printing) for microfabrication," *Microsystem Technologies*, vol. 23, no. 4, pp. 1117–1124, 2017.

[100] S. A. Nauroze, J. G. Hester, B. K. Tehrani, W. Su, J. Bito, R. Bahr, J. Kimionis, and M. M. Tentzeris, "Additively Manufactured RF Components and Modules: Toward Empowering the Birth of Cost-Efficient Dense and Ubiquitous IoT Implementations," *Proceedings of the IEEE*, vol. 105, no. 4, pp. 702–722, 2017.

[101] `www.explainthatstuff.com/ink-jetprinters.html`.

[102] B. S. Cook, C Mariottit, R Cooper, D Revier, B. K. Tehrani, L Aluigit, L Roseuit, and M. M. Tentzeris, "Transformers on Flexible LCP Substrate," pp. 3–6, 2014.

[103] B. Tehrani, R. Bahr, M. Tentzeris, D. Revier, and B. Cook, "The Principles of Smart Encapsulation : Using Additive Printing Technology for the Realization of Intelligent Application-Specific Packages for IoT , 5G , and Automotive Radar Applications,"

[104] M. Smith, Y. S. Choi, C. Boughey, and S. Kar-narayan, "Controlling and assessing the quality of aerosol jet printed features for large area and flexible electronics Controlling and assessing the quality of aerosol jet printed features for large area and fl exible electronics," 2017.

[105] A. Mahajan, C. D. Frisbie, and L. F. Francis, "Optimization of Aerosol Jet Printing for High-Resolution , High- Aspect Ratio Silver Lines," 2013.

[106] *Schematic for aerosol-jet printer*, `www.powerelectronictips.com`.

[107] Y. Lee, C. Howe, S. Mishra, D. Sup, M. Mahmood, M. Piper, and Y. Kim, "Wireless , intraoral hybrid electronics for real-time quantification of sodium intake toward hypertension management," pp. 1–6, 2018.

[108] *Novacentrix website*, `https://www.novacentrix.com`.

[109] S. S. Mohan, M. Hershenson, S. P. Boyd, and T. H. Lee, "Simple Accurate Expressions for Planar Spiral Inductances," vol. 34, no. 10, pp. 1419–1424, 1999.

[110] *Inductance calculator*, `http://www.circuits.dk/calculator_planar_coil_inductor.htm`.

[111] *Shielded inductor vs. unshielded inductor*, `https://www.we-online.com/web/en/passive_components_custom_magnetics/blog_pbcm/blog_detail_electronics_in_action_107485.php`.

[112] B. J. Roth and P. J. Basser, "A model of the stimulation of a nerve fiber by electromagnetic induction," *IEEE Transactions on Biomedical Engineering*, vol. 37, no. 6, pp. 588–605, 1990.

[113] J. Larsson, "Electromagnetics from a quasistatic perspective," *American Association of Physics Teachers*, vol. 3, no. 75, pp. 230–239, 2007.

[114] COMSOL Multiphysics, "Comsol Multiphysics Reference Manual: Version 4.4," 2013.

VITA

Sagarika Mukesh received her B.E. degree in Instrumentation and Control engineering from Manipal Institute of Technology, Manipal, India in 2011 and her M.Sc. in Embedded Electronics from ESIGELEC, France in 2014. She received her Master's in Electrical and Computer Engineering in 2017, with a minor in Computer Science at the Georgia Institute of Technology. She also participated in the TI:GER program from 2016 to 2018, to explore the value proposition of an improved cochlear implant that promises better frequency resolution.

Sagarika has been working on theoretical and experimental evaluation of micro-scale magnetic stimulation during her PhD at the Georgia Institute of Technology. Her work involves the use of finite-element analysis to lay the basis of developing novel ways to experimentally test this stimulation technique.

She has also mentored several undergraduate students, volunteered for the green initiatives around campus, volunteered for STEM outreach by teaching at summer camps and participating in activities across schools in Atlanta, and served as the treasurer of the ECE Graduate Student Organization. She loves travelling, star gazing, and learning about different cultures.